

Study on Light-Ion Helicon Plasma Production with High-Density in Non-Uniform Magnetic Field

MORI Yoshitaka

June, 2004

Study on Light-Ion Helicon Plasma Production with High-Density in Non-Uniform Magnetic Field

by MORI Yoshitaka

ABSTRACT

A helicon plasma is categorized as a wave-sustained inductive coupling discharge in the presence of an applied magnetic field in which high density ($\sim 10^{19} \text{ m}^{-3}$) plasma generation can be obtained with very high ionization efficiency. Since the 1980s, continuous studies have been conducted for the purpose of developing an efficient plasma source for an industrial plasma processing and of investigating the mechanism of high-ionization efficiency. Helicon plasma sources have been spread out many field, not only for plasma processing, but also for fusion-intended experiments and space plasma simulator. However, since interests have been placed on the investigation of physics, most helicon research has been conducted in a relatively uniform static magnetic field and heavy ions such as Ar. Light ion, especially hydrogen, helicon operation is more sensitive to magnetic field strength and geometry than heavy ions. Above all, hydrogen helicon wave plasma had been considered very difficult until very recent. The axial non-uniform Mini-Radio Frequency Test Facility (Mini-RFTF) has the capability for controlling static magnetic fields and then is applicative for light ion source plasma operation. Actually, high density ($\sim 10^{19} \text{ m}^{-3}$) hydrogen helicon discharge has succeeded in Mini-RFTF. Non-uniform static magnetic field geometry also can produce a high velocity to plasma exhaust when combined with ICRF heating enabling the possibility of use in plasma propulsion.

The systematic understanding of helicon plasma source for non-uniform magnetic field contribution and the optimization to obtain light-ion high-density plasma will shed light on a robust plasma source for a specific plasma propulsion concept: Variable Specific Impulse Magnetoplasma Rocket (VASIMR) and for the testing of fusion-intended device components represented as antenna or divertor.

In this thesis, both numerical and experimental analyses are undertaken for non-

uniformity contributions to the light-ion helicon plasma discharges.

Chapter 1 gives a historical background of the helicon sources and their expected applications from the point of view of plasma propulsion.

The theory of helicon waves is described in Chapter 2 focusing on wave dispersion relations.

Non-uniform magnetic field helicon plasma facility (Mini-RFTF), used in experiments of this thesis, is described in Chapter 3 including diagnostics systems.

Chapter 4 shows comparisons between experiments and results from a coupled RF and transport model. Experimental observation of plasma sustainment can be quantitatively reproduced by a flux-tube-averaged transport model. Simulations of electromagnetic wave propagations and power absorptions including a plasma profile of the experiments indicate that damping of helicon wave mainly contributing to high-density helicon plasma sustainment.

Chapter 5 gives a discussion of high density hydrogen helicon plasma in a nonuniform magnetic field. Where, high-density ($\sim 10^{19} \text{ m}^{-3}$) hydrogen plasma has been successfully sustained in axially nonuniform static magnetic field configurations for frequencies both above and below the high-density limit of the lower hybrid resonance frequency (LH-HD). Wave field measurements suggest that several modes are coupling to generate these helicon plasmas. The dependence of the plasma density on the static magnetic field strength for fixed geometry can be explained by wavelengths that are close to the antenna length and that couple to the fundamental radial mode for frequencies below the LH-HD frequency and to the second radial mode for frequencies above the LH-HD frequency.

Chapter 6 gives contributions of non-uniform magnetic field to density enhancement of light ion helicon plasma sources. In this chapter, the ultimate achievable density, well above 10^{19} m^{-3} both hydrogen and helium, has been found to depend strongly on the shape of axial magnetic field strength profile as well as on the magnitude of B. As the magnetic field strength is swept from low to high values, two local maxima in plasma density are observed for cases in which the field strength increases monotonically in the downstream direction away from the helicon antenna. A comparison of the plasma density close to the antenna and further downstream suggests that the maximum at low field corresponds to efficient power absorption on source region. For the maximum at high field, plasma density drops sharply in

the case of hydrogen, but only slowly in the case of helium. The data suggests that this is due to a strong rise in the threshold power required to reach the high-density mode in hydrogen, which is not seen for helium operation.

Chapter 7 gives focusing magnetic field contribution for light-ion helicon plasma on Mini-RFTF. Here, field geometry dependence on source regions are conducted. As the results, the net power dependence for strong focusing field has gradual high-density transition compared with flat field configuration in which clear helicon mode transitions are observed. Strong focusing field geometry results in sustainment of high-density helicon plasma with smooth matching control. Measurements of both axial and radial density profiles reveals that flare geometry yields plasma generation region further downstream. It is found that magnetic fields configuration of source region is strongly related to the downstream plasma sustainment and a possible control method for further optimization.

Chapter 8 gives summaries and suggestions for future experiments.

Contents

1	Introduction	8
2	Helicon plasma dispersion relations	12
2.1	Background	12
2.2	Uniform plasma	12
2.3	Radial non-uniform plasma	14
3	The Mini-RFTF helicon plasma machine	20
3.1	Background	20
3.2	Mini-RFTF device	21
3.3	Diagnostics	24
3.3.1	Power monitor system	24
3.3.2	Single Langmuir probe	25
3.3.3	RF compensated Langmuir probe	27
3.3.4	RF magnetic probe	31
3.3.5	Interferometer	34
3.3.6	Data accumulation system	36
4	Comparison of high-density hydrogen helicon plasma experiments with modeling for non-uniform magnetic field geometry	39
4.1	Introduction	39
4.2	Review of RF modeling and power transport	40
4.2.1	RF modeling	40
4.2.2	Transport modeling	41
4.3	Experimental set-up	43
4.4	Comparison between the model and experiments	44

4.5	Conclusions	48
5	High-density hydrogen helicon plasma in a nonuniform magnetic field	50
5.1	Introduction	50
5.2	Experimental set-up	52
5.3	Effects of static magnetic geometry and field strength	54
5.3.1	Source magnetic field configuration	54
5.3.2	Isolating effects of the static magnetic field geometry	58
5.4	Isolating magnetic field strength dependencies	65
5.4.1	Radial and axial mapping of the RF magnetic field	66
5.4.2	Radial mode analysis	68
5.5	Discussion	74
6	Non-uniform magnetic field contribution to density enhancement of light ion helicon plasma sources	77
6.1	Introduction	77
6.2	Experimental apparatus and geometry of the external magnetic . . .	78
6.3	Dependence of density enhancement on magnetic field strength	79
6.4	Flux tube mapping dependence of density enhancement	84
6.5	Discussion	88
6.6	Conclusions	90
7	Focusing magnetic field contribution for helicon plasma	92
7.1	Introduction	92
7.2	Experimental Setup	93
7.3	Experimental Results and Discussion	93
7.4	Summaries and Conclusions	97
8	CONCLUSIONS	99
	References	101
	Acknowledgements	108

Chapter 1

Introduction

The motivation of this thesis originates from investigation of the robust plasma source for plasma propulsion. Most plasma propulsion concepts rely on electrostatic fields to accelerate plasma to produce thrust. These concepts require electrodes that are in contact with the plasma and are subject to erosion, which limits the thruster's life time. This problem will be crucial when a mission requires high power and high ion velocity represented as a deep-space mission or a human planetary exploration. A solution to this is to drive thrust with electrode-less system. For the purpose of electrode-less plasma propulsion system, several methods are developed. The utilization of Radio Frequency wave to accelerate ions has attracted great interests as a spin-off technology of heating plasma in the magnetic confinement fusion device. Those ion acceleration methods have been conducted for plumes of the plasma discharged by Electron Cyclotron Resonance (ECR) [1–8] and by Magneto-Plasma-Dynamic (MPD) thruster [9–11]. Above all, the most systematic electrode-less plasma propulsion experiments are conducted on the Advanced Space Propulsion Laboratory (ASPL) of NASA's Johnson Space Center [12], where NASA-led research team involving industry, academia and government facilities in the United States have been pursuing the development of a concept named Variable Specific Impulse Magnetoplasma Rocket: VASIMR [13–15].

Figure 1.1 shows a schematic of VASIMR rocket. The VASIMR is a high power radio frequency driven magnetoplasma rocket which utilizes a helicon wave discharge for plasma generation. Generated ions are accelerated by an Ion Cyclotron Resonant Frequency (ICRF) wave and then expand in a magnetic nozzle contributing to thrust generation [12, 16]. The development of ICRF heating have been conducted

VASIMR Laboratory Experiment

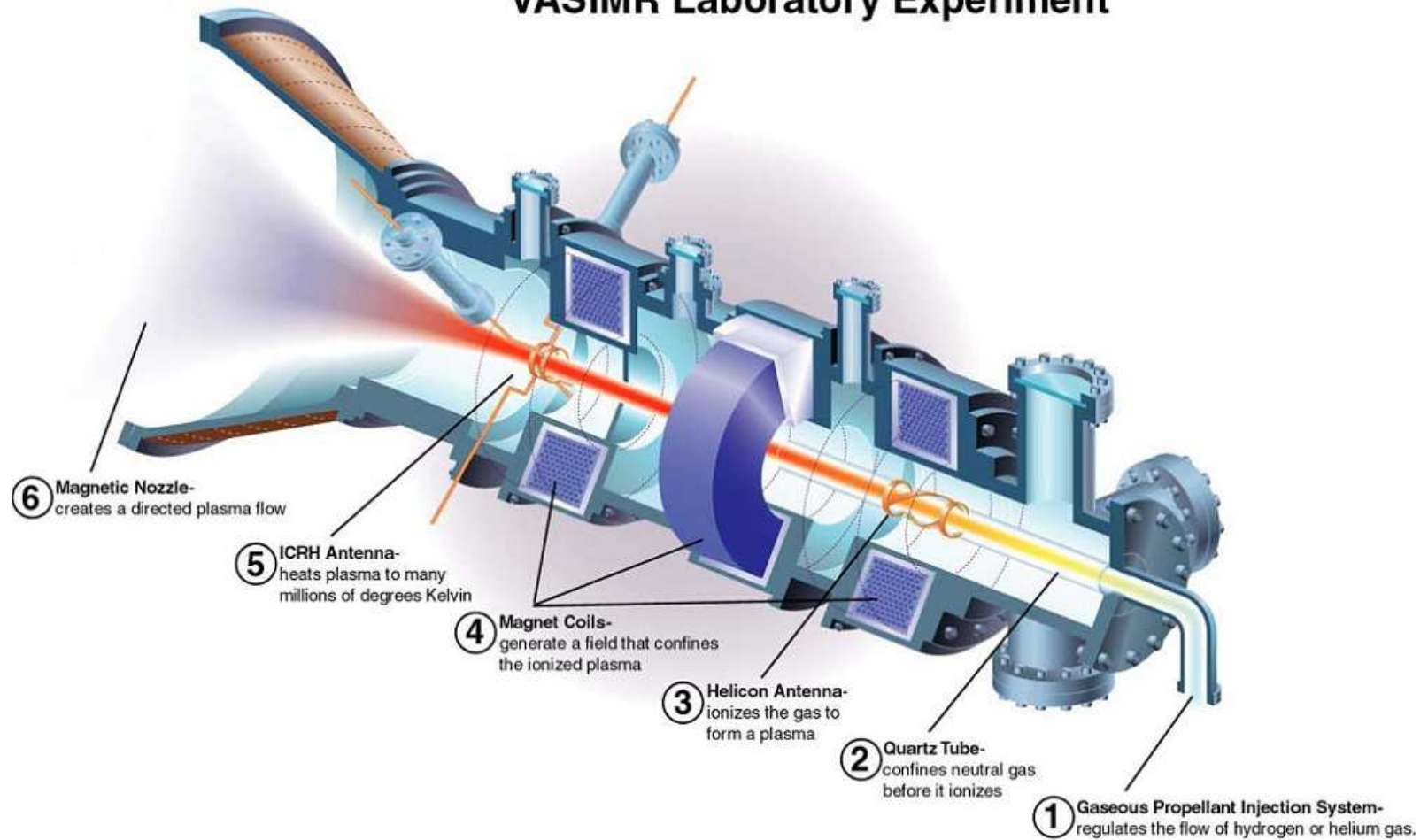


Figure 1.1: Schematic of VASIMR [12].

since the dawn of the magnetic confinement fusion research [17] and now considered as one of the indispensable techniques proposed for use on ITER: International Thermonuclear Experimental Reactor [18]. As for the helicon plasma discharge, although it was discovered in a gaseous plasma [19] and examined [20] in the 1960s, the investigation of its physics and optimization for applications are still attractive topics and many researchers have been devoting themselves to the investigation. The author of this thesis is no exception.

The helicon discharge is categorized as a wave-heated inductive coupling plasma in the presence of an applied magnetic field in which high density ($\sim 10^{19} \text{ m}^{-3}$) plasma generation can be obtained with a very high ionization efficiency [21]. After a reconsideration and a systematic study of helicon source by Boswell [21] in the 1980s, continuous studies have been conducted to develop an efficient plasma source for an industrial plasma processing and to investigate the mechanism of high ionization efficiency [22, 23]. Helicon plasma sources have been spread out many fields, not only for the plasma processing [24, 25], but also for fusion-intended experiments [26–28] and a space plasma simulator [29, 30]. However, since interests have been placed on physics rather than applications, most of helicon researches have focused on a relatively uniform static magnetic field and heavy ions such as Ar. For light ion, especially hydrogen, helicon operation is more sensitive to magnetic field strength and geometry than heavy ions. Above all, hydrogen helicon wave discharge had been considered very difficult until very recent [28, 31, 32].

The axial non-uniform Mini-Radio Frequency Test Facility; Mini-RFTF, has a capability for controlling static magnetic fields, and then it is applicable to light ion source plasma operation. Actually, high density ($\sim 10^{19} \text{ m}^{-3}$) hydrogen helicon discharge has succeeded in Mini-RFTF [32, 33]. Non-uniform static magnetic field geometry also can produce a high velocity to plasma exhaust when combined with ICRF heating enabling the possibility of use in plasma propulsion. Systematic understanding of helicon plasma source for non-uniform magnetic field and optimization to obtain light-ion high density plasma will shed light on a robust plasma source for a specific plasma propulsion concept represented as VASIMR and for the testing of components mounted on fusion-intended plasma devices represented as antenna or divertor [31, 34].

The thesis consists of eight chapters.

Following this chapter, Chapter 2 gives a theoretical background of the helicon plasma discharge, especially focusing on wave dispersion relations.

Chapter 3 introduces an experimental setup of Mini-RFTF; the device for light ion helicon plasma production in non-uniform magnetic field.

Chapter 4 gives comparisons of high-density hydrogen helicon plasma experiments with modeling for non-uniform magnetic field geometry. In this chapter, a computational study to simulate helicon plasma is reviewed, and then comparisons of the results between computations and experiments are conducted.

Chapter 5 describes investigation of high density hydrogen helicon plasmas in a non-uniform magnetic field. In this chapter, high-density ($\sim 10^{19} \text{ m}^{-3}$) hydrogen plasma has been successfully sustained in axially nonuniform static magnetic field configurations. Helicon plasma sustainment is discussed in terms of multi-radial eigenmode coupling.

Chapter 6 contains a contribution of non-uniform magnetic field to density enhancement of light ion helicon plasma sources. Here, plasma densities well above 10^{19} m^{-3} have been observed in helicon sources operating with hydrogen and helium. The dependences of the axial magnetic field strength profile and the magnitude of itself on high-density plasma sustainment are described.

Chapter 7 describes a contribution of focusing magnetic field to light-ion helicon plasma. Here, dependences of field geometry in source regions on plasma characteristics are examined in terms of RF power. Plasma production characteristics in terms of species, hydrogen and helium, are also shown here.

Finally, Chapter 8 gives summaries and future suggestions.

Chapter 2

Helicon plasma dispersion relations

2.1 Background

The name "helicon" was introduced by Aigrain [35] to describe an electromagnetic wave propagating in the presence of an applied magnetic field at low temperatures with frequencies between the electron and ion cyclotron frequencies. Theoretical treatment of helicon waves in a cylindrical magnetoplasma has been reported by Legéndy et al. [36] and Klosenberg et al. [37] in the 1960s. After these pioneer works, further modeling of the helicon discharge theories have been conducted including an electron inertia [38–40] and radial non-uniform plasma shape [20, 38, 40–42]. Here, a contribution of radial nonuniformity to a helicon eigenmode of dispersion relation is mainly described, since this is important for the following chapters. Other important theoretical investigations such as energy absorptions related with Trivelpiece-Gould mode appearing when the electron inertia is included [43, 44] are left out here.

Following this section, a wave dispersion relation in a uniform magnetic field is described in Section 2.2. Section 2.3 gives a contribution of radial nonuniformity to the dispersion relations in terms of an azimuthal mode.

2.2 Uniform plasma

The electromagnetic dispersion relation for a uniform cold plasma can be written as [45]

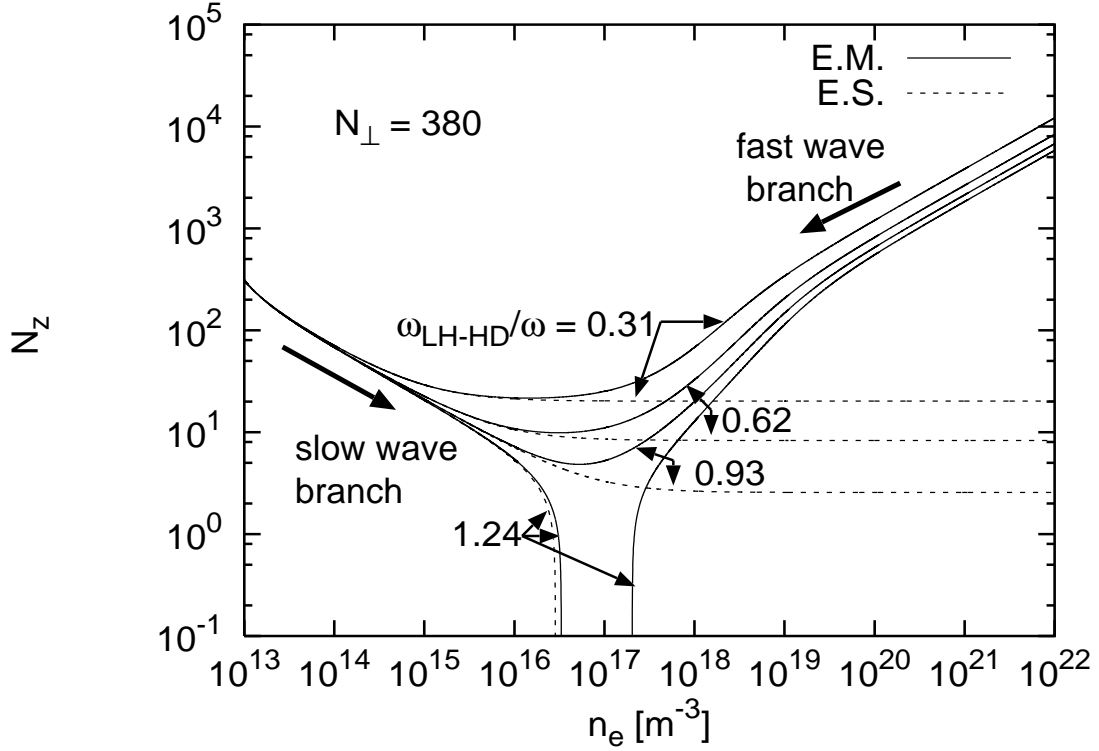


Figure 2.1: The dependence of N_z on electron density n_e for the cold uniform plasma. Solid lines show electromagnetic waves and dashed lines show electrostatic waves. N_\perp is determined for our interesting value. Slow and fast wave merging point is disappeared for $\omega_{LH-HD}/\omega > 1$.

$$SN_\perp^4 + [(N_z^2(S + P) - (S^2 - D^2 + PS))N_\perp^2 + P[N_z^2 - (S + D)][N_z^2 - (S - D)] = 0, \quad (2.1)$$

where N_\perp and N_z are the indices of refraction perpendicular and parallel, respectively, to the static magnetic field B_0 , $S = 1 - \sum_j \omega_{pj}^2 / (\omega^2 - \omega_{cj}^2)$, $P = 1 - \sum_j (\omega_{pj}^2 / \omega^2)$, and $D = \sum_j (\omega_{cj} / \omega) \omega_{pj}^2 / (\omega^2 - \omega_{cj}^2)$. Here ω is the operating RF frequency, $\omega_{cj} = q_j B_0 / m_j$ is the cyclotron frequency of the j^{th} species, $\omega_{pj} = \sqrt{q_j^2 n_j / (\epsilon_0 m_j)}$ is the plasma frequency for the j^{th} species, ϵ_0 is the permittivity of free space, and q_j , m_j , and n_j denote the species charge (with sign), mass, and density of the j^{th} species, respectively.

Figure 2.1 shows the dispersion relation for a cold uniform plasma. The dependence of N_z in the electromagnetic wave on the electron density n_e is shown

in Figure 2.1 as solid line, while N_z in the electrostatic limit ($PN_z^2 + SN_\perp^2 = 0$) is shown as dashed line. Here, $\omega_{LH-HD} = \sqrt{|\omega_{ce}\omega_{ci}|}$ is the High-Density limit of the Lower Hybrid frequency: $[\omega_{LH-HD}^{-2} + (\omega_{pi}^2 + \omega_{ci}^2)^{-1}]^{-1/2}$. The value of ω_{LH-HD} is also useful to normalize the field strength B_0 represented as ω_{LH-HD}/ω . Single species H^+ ion plasma is assumed to calculate ω_{LH-HD}/ω in the following discussions. For typical parameters, Equation (2.1) has two propagating modes with the slow wave propagating for lower densities and the fast wave propagating at higher densities. For a helicon plasma with a single ion species and $\omega < \omega_{ce}$, the fast and slow waves merge for $\omega_{LH-HD}/\omega < 1$. For $\omega_{LH-HD} > \omega$, these waves are separated and only the fast (helicon) wave ($N_z \propto n_e/B_0$ [46]) can propagate for high density plasma.

2.3 Radial non-uniform plasma

Discussion in the previous section has based on the uniform plasma. Generally, density-jumped helicon plasma has a strong non-uniformity of radial plasma density profile. Here we will include the radial non-uniformity, and then find out that dispersion relation yields a dependence of azimuthal mode.

Helicon plasma dispersion relations within cylinders have been developed for a radial uniform plasma as well as non-uniform shape [20, 36, 38, 41, 42]. Here we refer to recent work by Chen et al. [47, 48] for their modeling flexibility. The radially oscillating magnetic field component, B_r , calculated from Maxwell's equations including a radial nonuniformity plasma density profile can be written as follows [48]

$$B_r'' + \left(1 + \frac{2m^2}{m^2 + \gamma k_z^2 r^2}\right) \frac{B_r'}{r} - \left[m^2 + \frac{mr\alpha}{k_z\gamma}\right. \\ \left. \frac{\alpha'}{\alpha} - \frac{r^2}{\gamma}(\alpha^2 - k_z^2\gamma^2) - \frac{m^2 + k_z r^2(2m\alpha - k_z\gamma)}{m^2 + \gamma k_z^2 r^2}\right] \frac{B_r}{r^2} = 0, \quad (2.2)$$

$$\alpha = \frac{\alpha_0}{a} n^*(r) = \frac{\omega}{k_z} \frac{e\mu_0}{B_0} n_0 n^*(r), \quad (2.3)$$

where $k_0 = \omega/c$, $\gamma \equiv 1 - (k_0/k_z)^2$, k_z is the axial wave number, m is the azimuthal mode, μ_0 is the permeability of vacuum, $(') = \partial/\partial r$, $n^*(r) = [1 - (r/a)^s]^q$ gives the analytically radial density profile represented as parabolic-like shape using variables s and q with a plasma radius of a , and n_0 is the maximum density on axis.

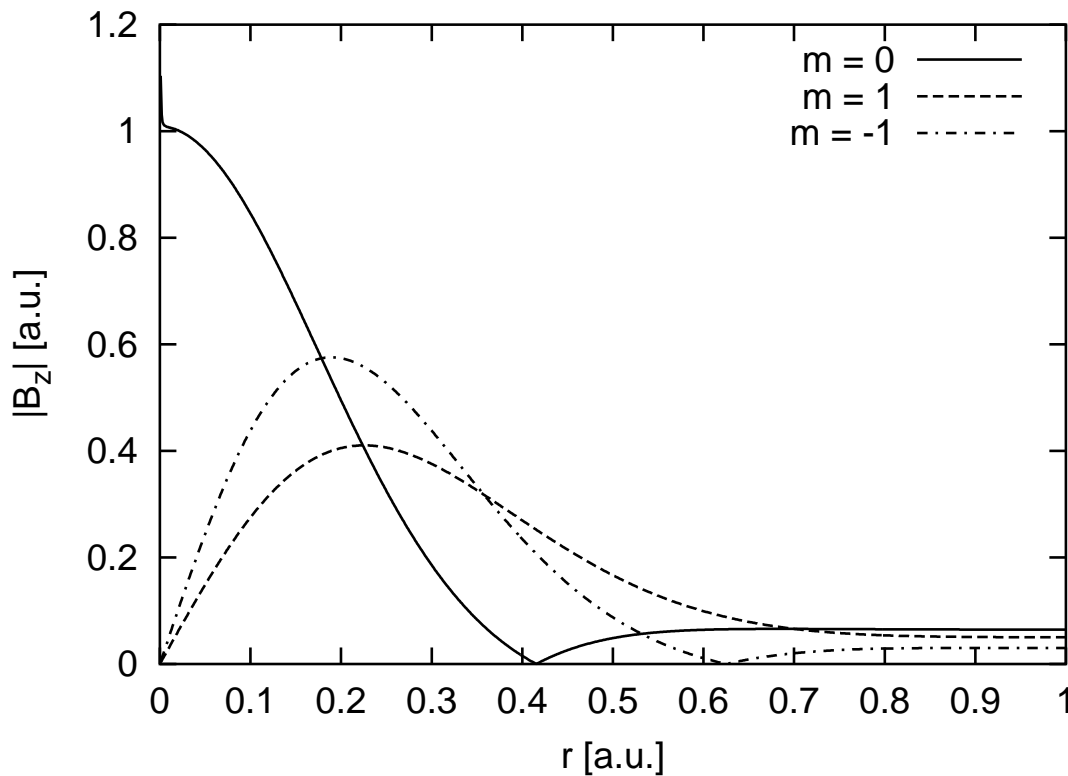


Figure 2.2: Radial profiles of $|B_z|$ for three azimuthal modes ($m = 0, 1$ and -1) in a parabolic-like density profile.

Equation (2.3) can be integrated numerically to satisfy the boundary condition, $B_r(r = a) = 0$, for the normalized radial eigenvalues of α_0 . Components of the other directions such as B_θ and B_z can be computed from the value of B_r .

Figure 2.2 shows $|B_z|$ curves for azimuthal modes represented as $m = 0, 1$ and -1 for a parabolic-like density profile ($s = 2, q = 4$). Eigenvalues of first radial modes were computed for each azimuthal mode from Equation (2.3), respectively. As shown in Figure 2.2, for $m = 1$, there is no node of B_z along the radius, although it was observed for both $m = 0$ and -1 . Therefore, the radial wave field profile contributes to identify the azimuthal mode and the measurements of radial profile of B_z on Min-RFTF will be shown in Chapter 5.

Figure 2.3 shows a dependence of the first (open circles) and second (closed circles) normalized radial eigenvalues on the radial density profile shape for parameters

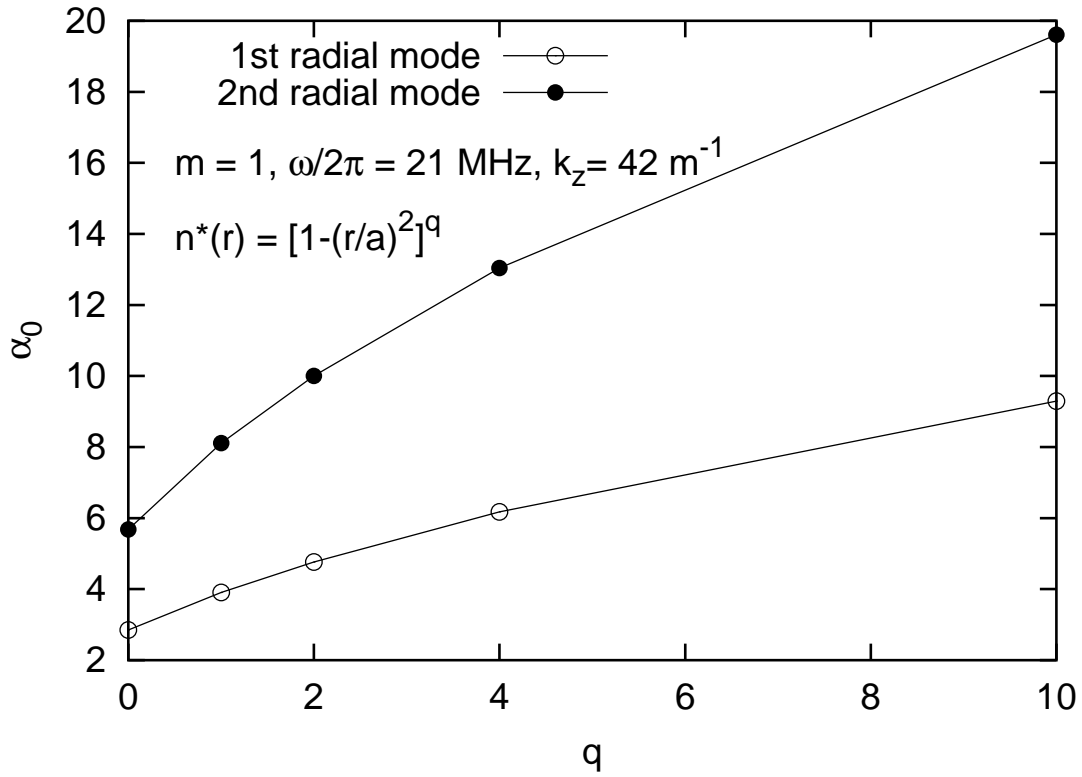


Figure 2.3: Normalized radial eigenvalue α_0 dependence on density profile for $m = 1$ for the first radial mode (open circles) and second radial mode (closed circles).

typical of our experimental conditions: $m = 1$, $\omega/2\pi = 21$ MHz, $s = 2$, and $k_z = 42$ m⁻¹. The value of k_z was chosen from the dominant axial wave length observed in our experiments which was close to the antenna length rather than twice the antenna length. The eigenvalues increase as the density profile peaks on axis (q increases).

If we assume that both the first and second radial eigenmodes are mixed in the system, then the helicon wave dispersion relation satisfies the following condition [47, 48]

$$\alpha_1 k_{z1} = \alpha_2 k_{z2}, \quad (2.4)$$

where $\alpha_{1(2)}$ and $k_{z1(2)}$ are the first (second) radial eigenvalues and the axial wave numbers, respectively.

The superposition of the first and second eigenmodes for the RF magnetic field can be written as [49]:

$$\begin{aligned} \tilde{B}_{rf} = \tilde{B}_1 + \tilde{B}_2 = & (1 - a_2)e^{-k_{z1}^i z} e^{i(k_{z1}^r z - \omega t)} \\ & + a_2 e^{-k_{z2}^i z} e^{i(k_{z2}^r z - \omega t)}, \end{aligned} \quad (2.5)$$

where a_2 is the ratio of the second wave field amplitude to a normalized wave amplitude defined as 1 at a wave launching point ($z = 0$), k_{z1}^r and k_{z1}^i are the real and imaginary part of the first (second) axial wave number, respectively. Experimental results can be fit using those factors described above and Figure 2.3.

Figure 2.4 shows an oscillating longitudinal magnetic component $|B_z|$ of $m = 1$. Both radial and axial profiles of B_z are measured in the experiments on Mini-RFTF, and then comparisons between measurements and the theory described here will be shown in Chapter 5. In Figure 2.4, at first, a B_r profile was calculated from Equation (2.3) then B_z field was obtained. The dashed line shows the first radial mode and dash-dotted line for the second radial mode. The solid line indicates the mixture of the first and second radial modes for $a_2 = 0.5$. As shown in Figure 2.4, mixture of the first and second radial modes is associated with the wave focusing effect.

One of the important characteristics of including non-uniform radial plasma density profile is that the dispersion relation has an azimuthal mode dependence [50, 51]. Figure 2.5 shows k_z versus n_e curves for several azimuthal modes including radial modes for the parabolic-like density profiles ($s = 2$, $q = 4$). Both external magnetic

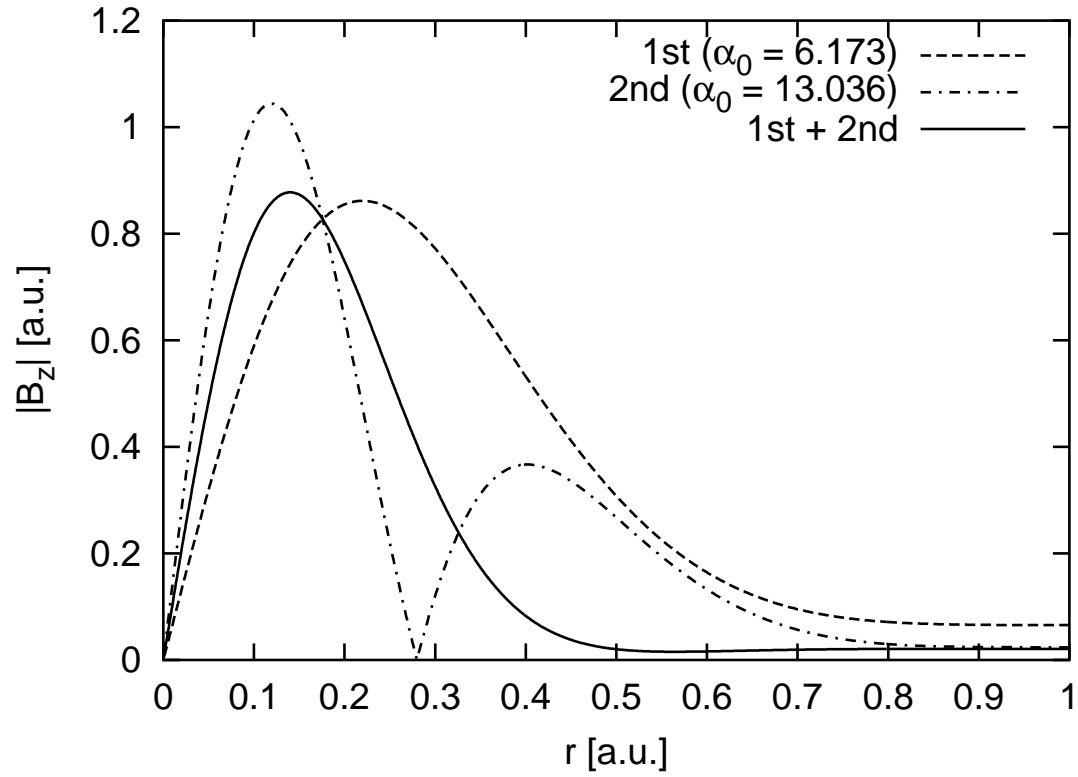


Figure 2.4: Radial profiles of the longitudinal magnetic field $|B_z|$ for the first (dashed line), second (dash-dotted line) radial mode and the mixture of them with the same amplitude (solid line).

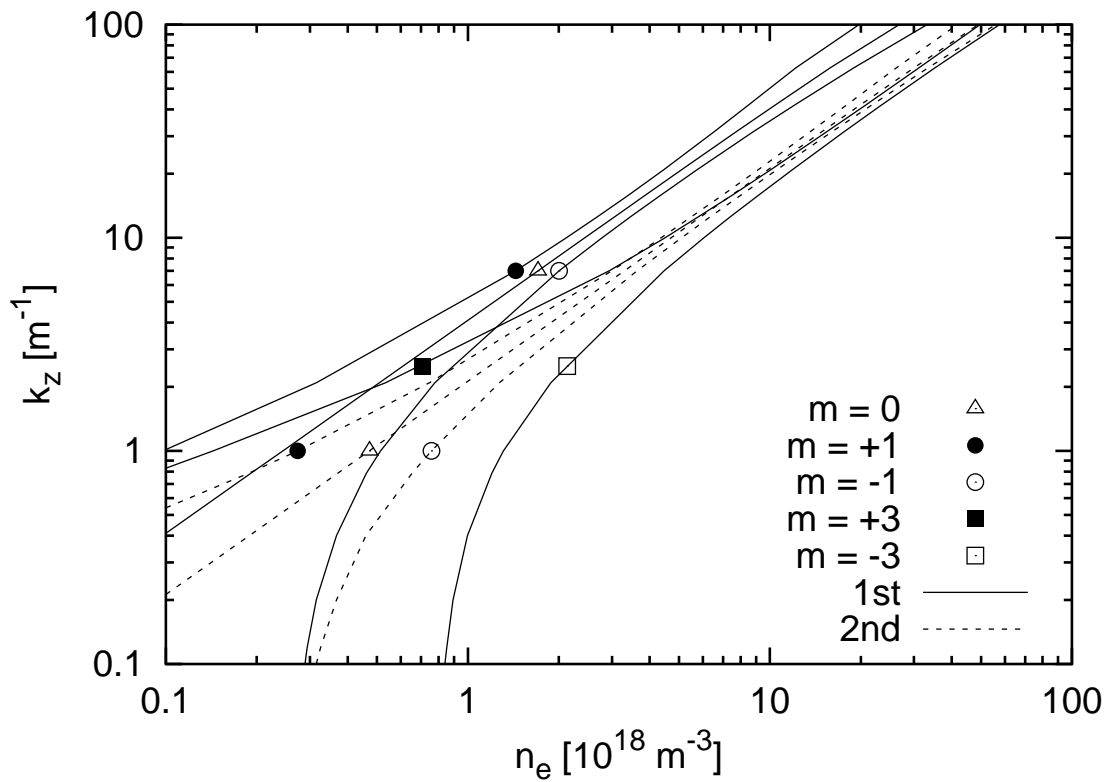


Figure 2.5: Azimuthal mode dependence of the dispersion relation.

field strength and plasma density profiles were fixed in these computations. From Figure 2.5, it is expected that k_z values become smaller when higher radial or azimuthal mode is excited at the same plasma density and magnetic field strength. It is also shown that azimuthal modes with minus sign ($m < 0$) have a strong dependence of n_e rather than $m \geq 0$, which yields cut off ($k_z = 0$) for a critical density. Figure 2.5 is useful to identify which mode can be excited in the experimental conditions.

Chapter 3

The Mini-RFTF helicon plasma machine

3.1 Background

The Mini-Radio Frequency Test Facility: Mini-RFTF, at Oak Ridge National Laboratory (ORNL) has been designed for the understanding of light-ion such as hydrogen, deuterium and helium, helicon discharge source intended for testing the new hardwares mounted on fusion plasma devices. Since the 1980s, Radio Frequency Test Facility: RFTF, a mirror device with super-conducting magnets at ORNL [52], has contributed to validate new hardwares represented as antennas for ICRF heating or current-drive mounting on fusion facilities [53, 54]. In the RFTF, a steady-state bulk plasma has been generated by ECR breakdown in a mirror magnetic field using a dedicated 28-GHz gyrotron. However, it has been claimed that large X-ray fluxes can be generated by electron rings formed under certain conditions of fields, gas density, and ECR heating power [52]. Dedicated attention should be paid for shielding of X-rays to prevent the experimental instruments from troubles. Moreover, achieved density was limited by a cut-off plasma density around $\sim 10^{18} \text{ m}^{-3}$ fixed by the gyrotron frequency, and the density is not sufficient to satisfy the requirement of latest fusion devices [34]. On the other hand, helicon discharge has the capability of higher density ($\sim 10^{19} \text{ m}^{-3}$) plasma sustainment without resonance processes. Development of helicon source on the Mini-RFTF will solve the technical problems of RFTF device such as cut-off density or X-ray radiations.

3.2 Mini-RFTF device

Figure 3.1 shows a schematic of the Mini-RFTF facility. The device consists of a quartz tube with radius $r_p = 2.3$ cm and length $L_p = 76$ cm that is placed into a stainless steel vacuum chamber. The chamber is pumped by a PfeifferTM TPH-510, turbomolecular pump (500 l/s) to a base pressure of 2×10^{-7} Torr measured by a Varian[®] B-A ionization gauge mounted on the end of the chamber close to the turbomolecular pump. Gas is fed into the system upstream (from the antenna side) through the quartz tube in which gas flow is controlled by a MKS[®] Mass-Flo[®] 179A-type, mass flow controller calibrated at He. H₂ or He gas was used for pressure ranging from 3 to 20 mTorr. Pressures described in this thesis were measured by a Granville-Phillips[®] 275 series, Convectron[®] gauge or a MKS[®] Baratron[®], capacitance manometer mounted around the port of ionization gauge.

Three magnet coils are aligned coaxially with the vacuum chamber. A solenoid coil (48 cm-long), represented as SOL in Figure 3.1, surrounds the quartz tube, providing an axial field up to 0.05 T in the source region. In the downstream region, a maximum axial field of 0.25 T was obtained using the first downstream mirror coil shown at $z = 0.9$ m as MR1 in Figure 3.1. The other mirror coil at $z = 1.55$ m was not used for the work presented here.

The antenna used for the experiments presented in this thesis is a 15-cm long, right-helical antenna mounted in air around the quartz tube as shown in Figure 3.2. The quartz tube is surrounded by a conducting cylinder with an inner diameter of 13 cm to provide a reliable RF ground. The matching circuit (see Figure 3.1) consists of two variable vacuum condensers in which a JenningsTM CSVF-500-0315, provides C_{SHT} 12 to 500 pF placed in parallel to the antenna for a resistance matching and the other, CometTM CV1-C-100E/15, gives C_{SER} 5 to 100 pF connected in series to the antenna for a reactance elimination.

Two power supply modules are available to energize the antenna. One consists of a Alpha/PowerTM 91B, 2 kW RF (1.8 to 28 MHz) amplifier driven by a Kenwood[®] TS-450S, transceiver 1.8 to 30 MHz. The other module requires two amplifiers to generate up to 20 kW power. In the module, a Hewlett-Packard/Agilent[®] 8657B, signal generator drives a Mini-Circuits[®] ZHL-1A, RF amplifier up to a power level which is large enough to drive a Continental ElectronicsTM AN/FRT-85, air-cooled

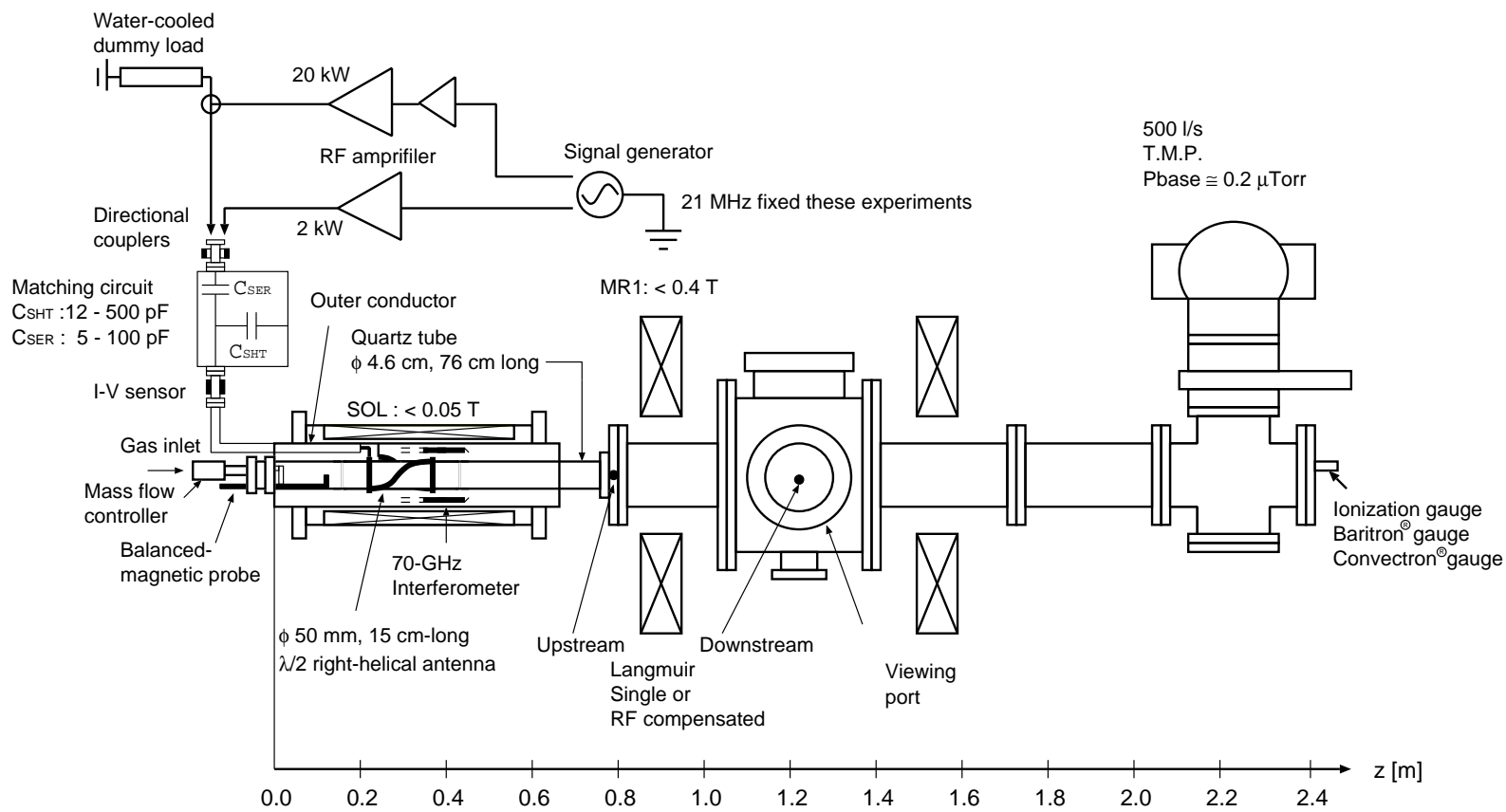


Figure 3.1: Schematic of the Mini-RFTF device at ORNL.



Figure 3.2: Photo of a right-helical antenna mounted on the Mini-RFTF.

RF (2 to 30 MHz) amplifier build for the U. S. Navy electronics systems command. We used the 2 kW power supply for low power operation and the 20 kW power supply for high power operation. The frequency was fixed at 21 MHz in the experiments presented here. During the very high power (> 3 kW) operations with AN/FRT-85, a Bird[®] water-cooled 50 Ω dummy load is placed in parallel with the antenna in order to prevent parasitic oscillations in the RF power supply, which can cause damage to the antenna, transmission line, and the power supply itself. This also allows the power supply to operate stably during the impedance transient that occurs when the plasma discharge ignites, and to drive over a wide range of input impedances that can be encountered during operation with the manually adjusted matching network.

3.3 Diagnostics

Diagnostics of the Mini-RFTF include a 70-GHz interferometer that can be scanned axially ($z = 0.1$ to 0.7 m), and two radially movable single or RF-compensated Langmuir probes; one is identified as upstream probe installed at the end of the quartz tube ($z = 0.78$ m), and the other, downstream probe, is installed at the middle of the viewing port ($z = 1.22$ m). A balanced-RF magnetic probe is used to scan the axial component of the oscillating magnetic field both axially and radially. A current-voltage (I-V) sensor mounted on the output of the matching network is used to measure both net power into the load including plasma and loading impedance. The net power also can be monitored by directional couplers mounted on the input of the matching circuit. Details of each diagnostics are given in the following sections.

3.3.1 Power monitor system

Net power into circuit can be measured by two type of Bird[®] directional couplers. Both of them are mounted between the power supply and the matching circuit. One consists of rectified elements (5000H and 1000H for forward and reflection powers, respectively) which are monitored during matching procedures to sustain power reflection. The other consists of RF sampling elements (couplers with 60 dB coupling factor for frequencies from 25 to 75 MHz) plugged into the network analyzer

for the precious net power measurements. Both current and voltage induced on the antenna can be monitored with the current–voltage (I-V) sensor fabricated at ORNL. All couplers and the I-V sensor were carefully calibrated respectively with a Hewlett-Packard[®] 8753D network analyzer at low power level (10 dBm) to obtain coupling factors. These values were also confirmed by high power (up to 5 kW) injection calibrations using the 50 Ω water-cooled dummy load.

During the experiments, signals from the directional couplers and the I-V sensor were monitored with the network analyzers. Using the network analyzer, very accurate measurements of antenna impedance including plasma loading are possible. A tuned receiver mode analysis of the network analyzer provides the values of each amplitude and phase shift of two synchronized RF signals. From the values of amplitude and phase shift of RF currents and voltages, both resistive and reactive impedances including net power can be obtained.

3.3.2 Single Langmuir probe

Insertion of a metal probe biasing to draw electron or ion current in plasma is one of the earlier and still the most useful tools for diagnosing a plasma [55]. The probe, called Langmuir probe has been studied and several improvements are conducted since the dawn of plasma physics. Here we review a brief theory of the single Langmuir probe assuming a large surface probe area with collisionless sheath [55, 56]. Such assumptions are reasonable for high-density helicon plasma conducted on the Mini-RFTF. A single Langmuir probe installed on Mini-RFTF consists of 0.010 inch diameter tungsten wire mechanically cramped to a semi-rigid cable. A tip of wire (a few mm-long) is exposed to the plasma and the rest is surrounded by a coaxial-insulator tube made of aluminum with ground-shielding to provide reduction of RF pick-up and to eliminate electrostatic disturbance into plasma. The coaxial-insulator tube is held with a stainless probe holder giving a robust RF shielding.

Consider that the probe is biased sufficiently negative to collect only ion current, I_i . The current by the probe, I , is

$$I = -I_i = -en_s A_s (eT_e/m_i)^{1/2} \quad (3.1)$$

where, e , n_s , T_e and m_i denote the charge of electron, the electron density at the sheath edge, the electron temperature and the ion mass, respectively. A_s is the

area of the sheath surface which is generally close to that of the probe tip surface represented as A_p . According to the Bohm sheath criterion, the density at the sheath is given by $n_s \sim 0.61n_e$, where n_e is the electron density in the bulk plasma.

If we know T_e and A_s , then the electron density is determined from the measurement of I_i . Typical electron temperature of helicon discharge is 2 to 10 eV, and then in most cases the ion saturation current $I_{is} \sim I_i$ represents roughly the order of electron density without knowing T_e . If we consider a probe near the floating potential, the normalized sheath thickness by the Debye length λ_D : x_s/λ_D can be obtained 3.8, 4.2 and 5.0 for H^+ , He^+ and Ar^+ species, respectively [56]. The sheath area is also approximately obtained for a cylindrical probe with radius a as $A_s \approx A_p(1 + x_s/a)$. Therefor the ion current near the floating potential is useful to determine the electron density if T_e is available.

For the determination of T_e , sweeping of the probe voltage is required to obtain a current–voltage characteristics. Considering that the probe potential V_p is retarding with respect to the plasma potential V_{sp} , then using Boltzmann’s relation, the electron component of the probe current is

$$I + I_i = I_e = \frac{1}{4}en_s\bar{v}_eA_s\exp\left(\frac{V_p - V_{sp}}{T_e}\right), \quad (3.2)$$

where $\bar{v}_e = (8eT_e/\pi m_e)^{1/2}$ and $V_p - V_{sp} < 0$ is the potential between the probe and the plasma. Taking the logarithm of Equation (3.2), we have

$$\ln(I_e) = \frac{V_p - V_{sp}}{T_e} + Const. \quad (3.3)$$

From Equation (3.3), the inverse slope of the logarithmic electron probe current with respect to V_p gives T_e directly in volts.

Figure 3.3 shows a schematic of a Langmuir probe measurement circuit. Here a Hewlett-Packard[®] 6209B, power supply is used to bias the voltage, V_b , negatively enough to draw the ion saturation current. A voltage across the load resistance R_m of 25 Ω or 100 Ω is measured with an Analog Devices[™] 3B40-00, isolated wideband amplifier, to reduce a noise came from the power supply itself. For the measurements of a current–voltage characteristics, a Wavetek[®] model-23, 12 MHz synthesized function generator is used to drive a Kepco[™] B0P100M, bipolar operational power supply/amplifier. The output voltage, V_{out} , is measured by oscilloscopes.

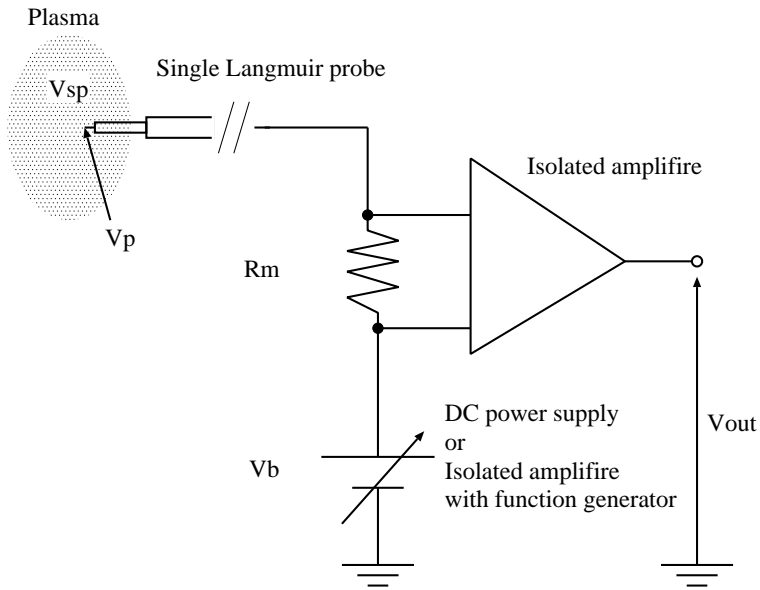


Figure 3.3: Schematic of the Langmuir probe measurement system.

3.3.3 RF compensated Langmuir probe

For RF-induced plasma sources represented as capacitive or inductive coupling plasma, RF pickup can distort current–voltage characteristics and then it gives higher estimation of electron temperature, T_e . Helicon plasma is no exception. Such distortion occurred because probe tip can not follow plasma potential, V_{sp} . Several methods for reducing RF effects have been tried [57–59]. Here, we review a RF compensated method by Sudit et al. [60], which was also refereed for a probe design and fabrication used in our experiments.

The principle is to isolate the probe tip from the circuit with a RF choke; an inductor which has a self-resonance around the RF with a stray capacitance. Including a RF choke provides enough impedance between probe tip and the rest circuit for operating RF as well as second harmonics. Additional external electrode with a capacitor is usually required for decrement of sheath impedance to draw enough charge from the V_{sp} oscillations. A schematic probe design is shown in Figure 3.4.

The probe tip was made of 0.3 mm-diameter, 1 mm-long tungsten wire. The wire was fed into a ceramic tube and mechanically cramped with a coupler tube which was soldered with a coupling capacitor. Tungsten wire of 0.3-mm diameter was closely wound 10 times around the ceramic tube, starting at the probe tip end,

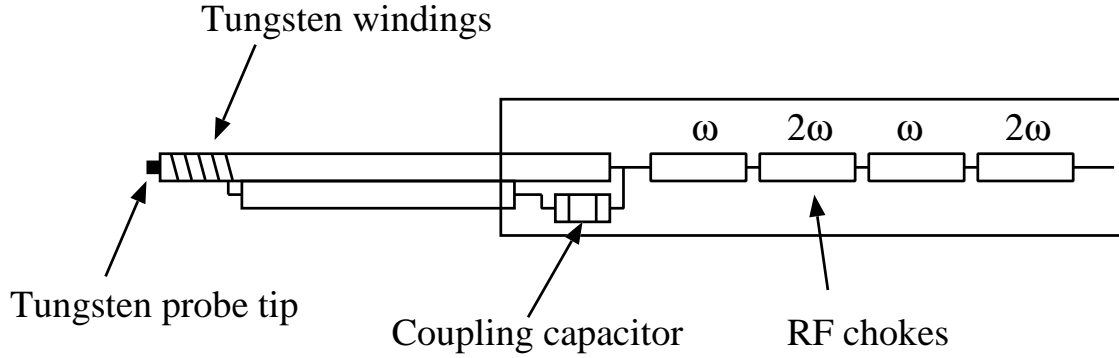


Figure 3.4: Schematic of a RF compensated Langmuir probe.

providing an apprehensive electrode to decrease sheath impedance. The wire was fed through a separate ceramic tube and soldered with the capacitor. The RF chokes in series with the probe tip wire, as well as the capacitor, were covered with a 1/4 inch stainless tube. A leader of the choke was plugged into a coaxial cable which follows a measurement circuit.

An equivalent circuit for the RF compensated probe is shown in Figure 3.5. Both equilibrium capacitances of sheath and electrode, C_{sh} and C_x , respectively shown in Figure 3.5 can be calculated by solving the Poisson's equation and the Child-Langmuir formula as

$$C_{sh,x} \approx \frac{\epsilon_0 A_{sh,x}}{2^{7/4} \lambda_D} \left[\frac{(V_{sp} - V_p)}{T_e} \right]^{-3/4}, \quad (3.4)$$

where λ_D is the Debye length, A_{sh} and A_x denote the surface areas of sheath and electrode, respectively. To resolve the current-voltage characteristics for electron temperature computation,

$$\frac{Z_{sh,x}}{Z_{sh,x} + Z_{ck}} |V_{RF}| \ll T_e \quad (3.5)$$

is required. Therefore, the apprehensive electrode with surface area $A_x \gg A_{sh}$, shown in Figure 3.4 as wounded wire, was added in order to decrease the sheath impedance. The electrode is connected to the RF short capacitor C_{cp} which is large enough to short out RF signal and small enough to isolate both D.C. signals and low frequency fluctuations excited in plasma. The design of RF-compensated probe was based on parameters of experiments conducted in this thesis.

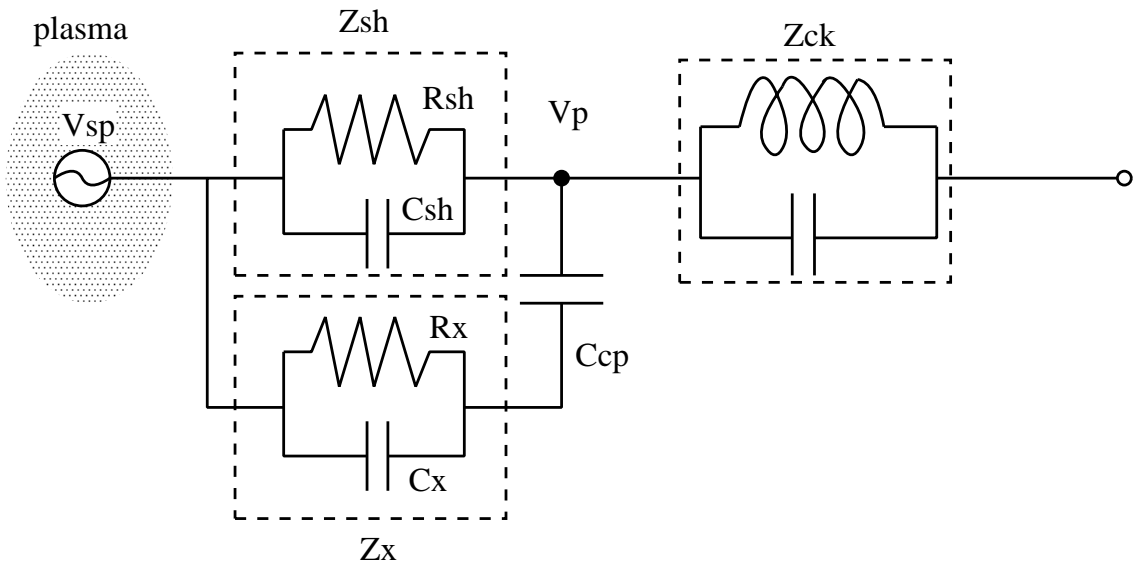


Figure 3.5: Equivalent circuit design of a RF compensated probe.

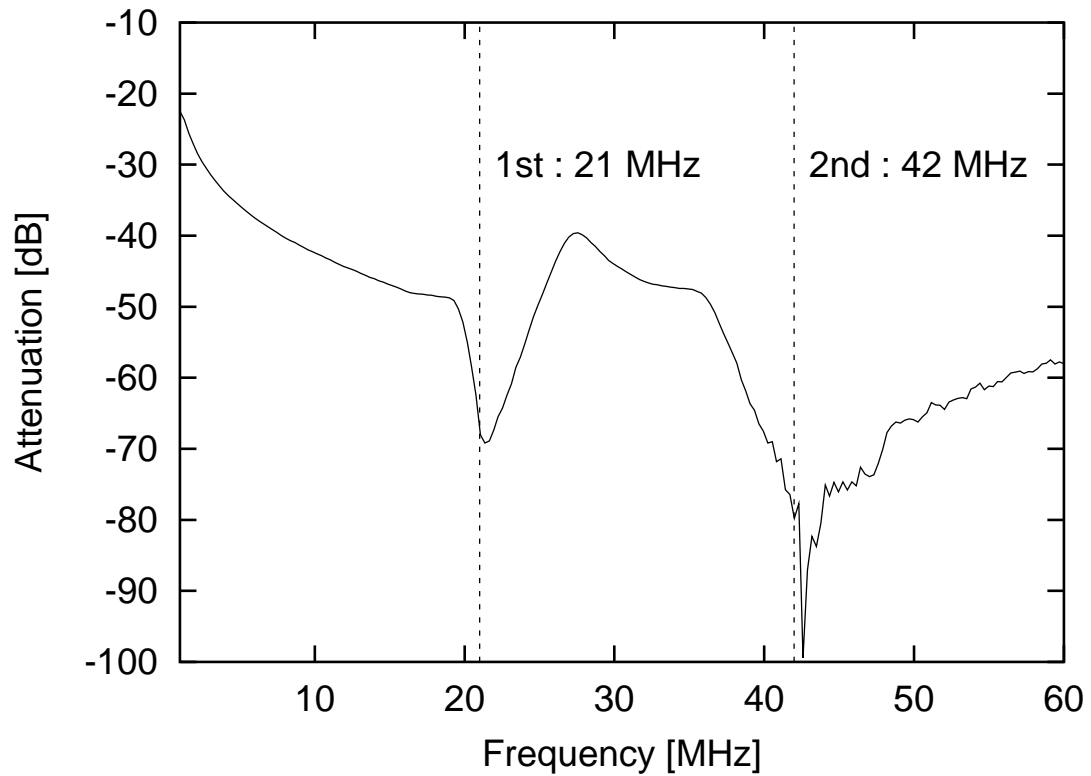


Figure 3.6: Attenuation measurements of the RF chokes mounted in a RF-compensated probe on the Mini-RFTF.

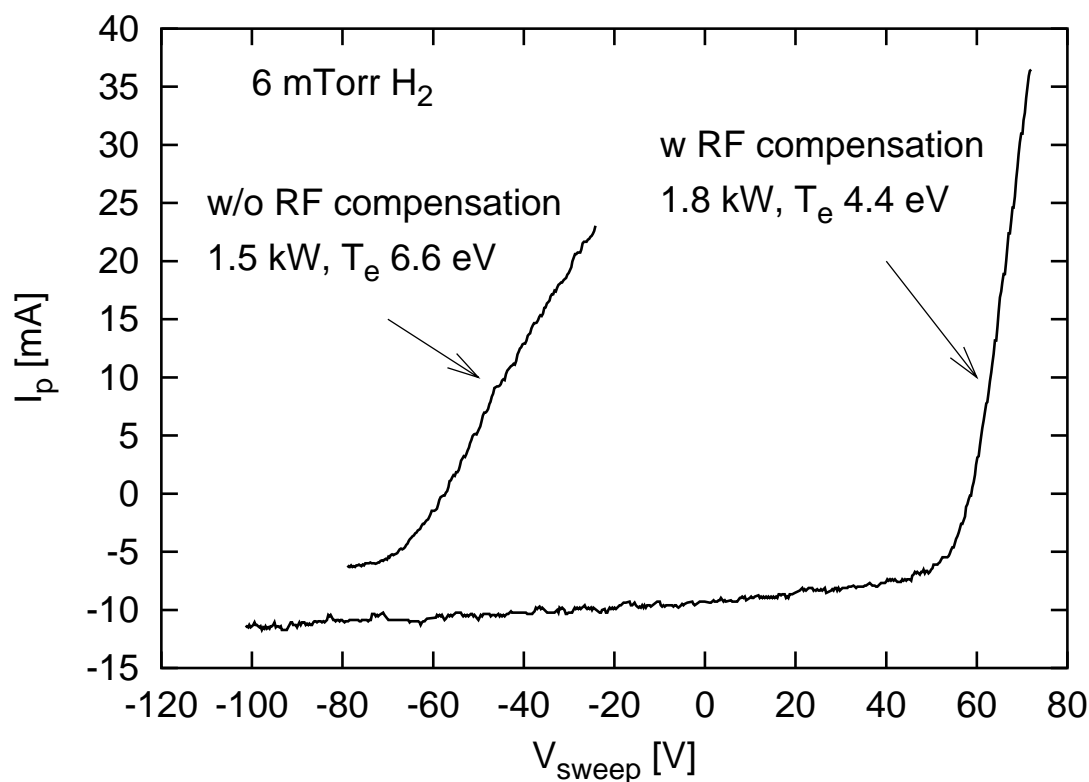


Figure 3.7: Current–voltage characteristic curves taken with and without RF compensation.

Figure 3.6 shows a network analyzer measurement of attenuation versus RF of RF chokes used in a RF-compensated probe. It is found that high impedance (high attenuation) is obtained around frequencies both fundamental and second harmonics. This value is high enough for RF compensations when the apprehensive electrode is used.

Figure 3.7 shows current–voltage curves measured in the experiments on Mini-RFTF for both with and without RF-compensations. From Figure 3.7, with compensations, the floating potential is found to be shifted higher voltage than without it. Also, the current–voltage characteristics curve with RF-compensation has a gradient for electron current steeper than without it. From these measurements, it was found that the RF compensation contributed to the resolution of electron temperature determination.

3.3.4 RF magnetic probe

An inductive RF magnetic probe is often used to measure electromagnetic fields both in plasma and vacuum. However, especially for higher RF operations, the probe becomes also sensitive to an electrostatic potential which distorts the electromagnetic field measurements. A calibration of the RF magnetic probe is required to confirm that the electrostatic pickup is suppressed enough and a probe sensitivity against the oscillating magnetic field, B_{rf} , at a given RF is reliable. Such calibrations often utilize a Helmholtz coil which generates a uniform magnetic field. However, because of a stray capacitance, the Helmholtz coil has a self resonant frequency around 100 MHz, hence for higher frequency (> 20 MHz) an amplitude of a current usually measured on a coil leader is not the same as that contributing to the oscillating magnetic fields [61]. Fortunately, utilization of the network analyzer has solved the problem described above; a sensitivity of the probe can be obtained from a s-parameter measurement by using two-port method [62]. In this section, a simple calibration method of a RF magnetic probe using the network analyzer is described.

The basic principle of the RF probe is to measure the magnetic field, B_{rf} , from the induced voltage to the pickup coil. The induced voltage $V_{RFprobe}$ to the RF probe can be obtained from Faraday's law:

$$V_{RFprobe} = \omega NS B_{rf}, \quad (3.6)$$

where ω is an angular frequency of the oscillating magnetic field and NS is the effective area of the RF probe. We define probe sensitivity as $S_0 = |V_{RFprobe}/B_{rf}|$. The theoretical value of S_0 is obtained from Equation (3.6) as follows,

$$S_0 = \omega NS. \quad (3.7)$$

Generally, calibration of S_0 is required to estimate an absolute value of B_{rf} at the operating RF.

Figure 3.8 shows a schematic diagram of the RF probe calibration system. The Hewlett-Packard® 8753D, network analyzer includes the output port RF out which provides a RF signal. The signal is divided by a Hewlett-Packard® 11549A, power divider into the input port R to refer a current to the loop and into the simple loop coil of diameter 50 mm (a resonant frequency of over 100 MHz) following after

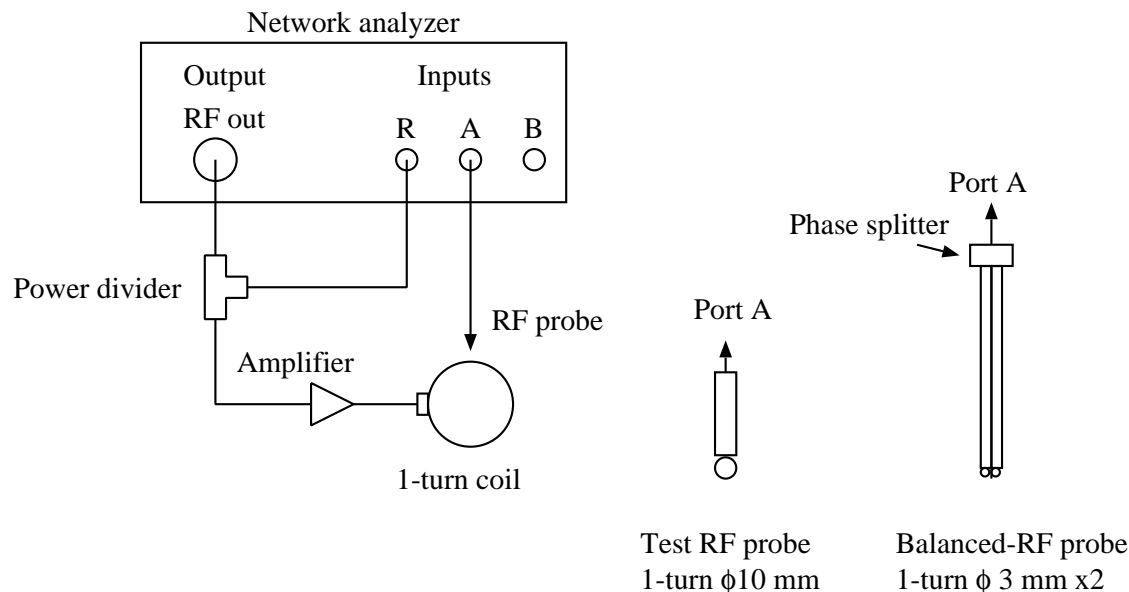


Figure 3.8: Schematic of a magnetic probe calibration system.

a Mini-Circuits[®] ZHL-2, power amplifier to excite detectable levels of magnetic fields. A RF probe is located on-axis of the simple coil to pick up the oscillating magnetic field and then the signal is into the input port A.

The ratio of the signals at port A to that of port B, A/R , in the network analyzer gives a relative value of a probe sensitivity. That is, the signal of the input port R represents a current into the coil: magnetic field B_{rf} , and that of the input port A represents pickup voltage by the probe. The absolute values of the sensitivity can be obtained by using a test probe. The test RF probe used had a 10 mm diameter of 1 turn loop mounted on the tip of 20 cm coaxial cable. A resonant frequency of the probe was around 600 MHz. So both resonance and leader length effects can be negligible at the region of our interesting frequency < 50 MHz in which the probe sensitivity can be calculated accurately from Equation (3.7). The calculated value agreed well with that measured from s-parameters by the network analyzer [62]. Therefore, the relative value of A/R between the balanced RF probe and the test probe gives a reliable probe sensitivity of the balanced probe.

Figure 3.9 shows calibration results of a balanced RF probe. The balanced RF probe consists of two pick up coils [63], each 3 mm in diameter with opposite orientation, and plugged into a Mini-Circuits[®] ZSCJ-2-1, phase splitter to eliminate

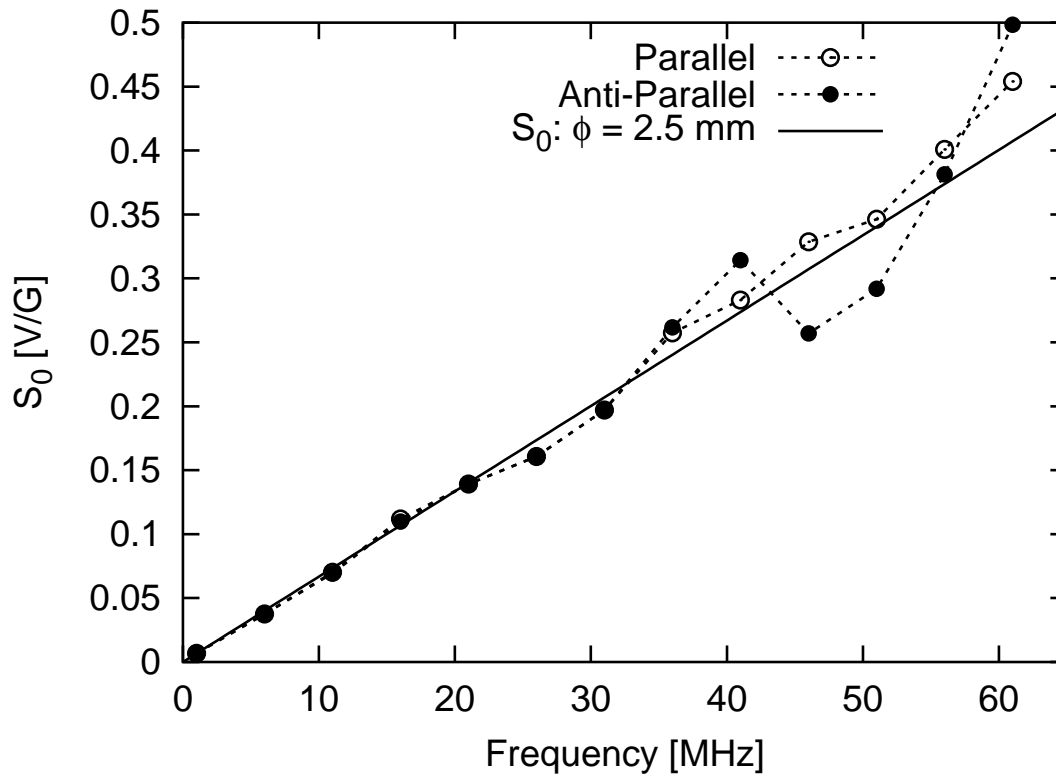


Figure 3.9: The balanced RF probe calibration results.

electrostatic signals. The probe was located on-axis of the single loop oriented parallel to the excited lines of magnetic force (open circles represented as parallel in the figure), and anti-parallel (closed circles). Solid curve indicates an estimated probe sensitivity from the fitting of data. From Figure 3.9, curves of both directions show linear increment against the frequency and adequate consistency up to 40 MHz. It was confirmed that the fabricated probe had reliable frequency characteristics and electrostatic signals were adequately eliminated up to 40 MHz.

For the propagating wave measurements, the network analyzer is utilized with the tuned receiver mode. Here, RF current signal from the I-V sensor is used as reference and then relative values of both phase and amplitude of the oscillating magnetic field to the antenna current are obtained. Amplitude of the magnetic field is also available.

3.3.5 Interferometer

One of the common methods to estimate absolute density is a measurement of the refractive index in plasma conducted by the form of interferometry [55, 56]. Although Langmuir probes are able to measure density profiles, they are unreliable for determining absolute density especially in the presence of strong magnetic field. For the density range from 10^{11} to 10^{19} m^{-3} for helicon plasma, and plasma diameter of cm or tens of cm, millimeter-wave can be handled very well. In the Mini-RFTF, a 70-GHz quadrature interferometer system has been used.

A schematic of interferometer circuit is shown in Figure 3.10. Millimeter-wave beam driven from the 70-GHz klystron is divided by the T conjunction into two ways, main and reference arms, respectively. The main arm is directly connected to the launch horn phase into plasma region, in which the launched beam is going through the plasma and then it is received by the receive horn which is connected to one of the quadrature mixer inputs, RFO. The referenced arm is plugged into the mixer input, LO, via a phase shifter device. Outputs of the mixer IF1 and IF2 are going to a tuning device, in which calibration of offset or gain of signals are conducted, and then plugged into an oscilloscope.

Outputs of the mixer are

$$V_{IF1} = A_1 \cos(\theta(t)) + V_{OFF1}, V_{IF2} = A_2 \sin(\theta(t)) + V_{OFF2}, \quad (3.8)$$

where subscript number, 1 or 2, of A_1 , A_2 , V_{OFF1} and V_{OFF2} represents the port number of the mixer, A_j and V_{OFFj} are the amplitude and the DC offsets, respectively. Phase error between IF1 and IF2 driven from the quadrature mixer is negligible in our system. Ideally, $A_1 = A_2$ and $V_{OFF1} = V_{OFF2} = 0$, so that outputs are exactly balanced with zero offset. In practice, calibration are possible by tuning the values of A_1 , A_2 , V_{OFF1} and V_{OFF2} . After that, phase shift as a function of time, $\theta(t)$, can be computed from

$$\theta(t) = \arctan \left[\left(\frac{A_1}{A_2} \right) \frac{V_{IF2}(t) - V_{OFF2}}{V_{IF1}(t) - V_{OFF1}} \right]. \quad (3.9)$$

Calibration to determine A_1 , A_2 , V_{OFF1} and V_{OFF2} is available with the variable phase shifter installed in the reference leg by sweeping through 2π phase shift under absence of plasma. During the calibration, signals shown on the X-Y mode

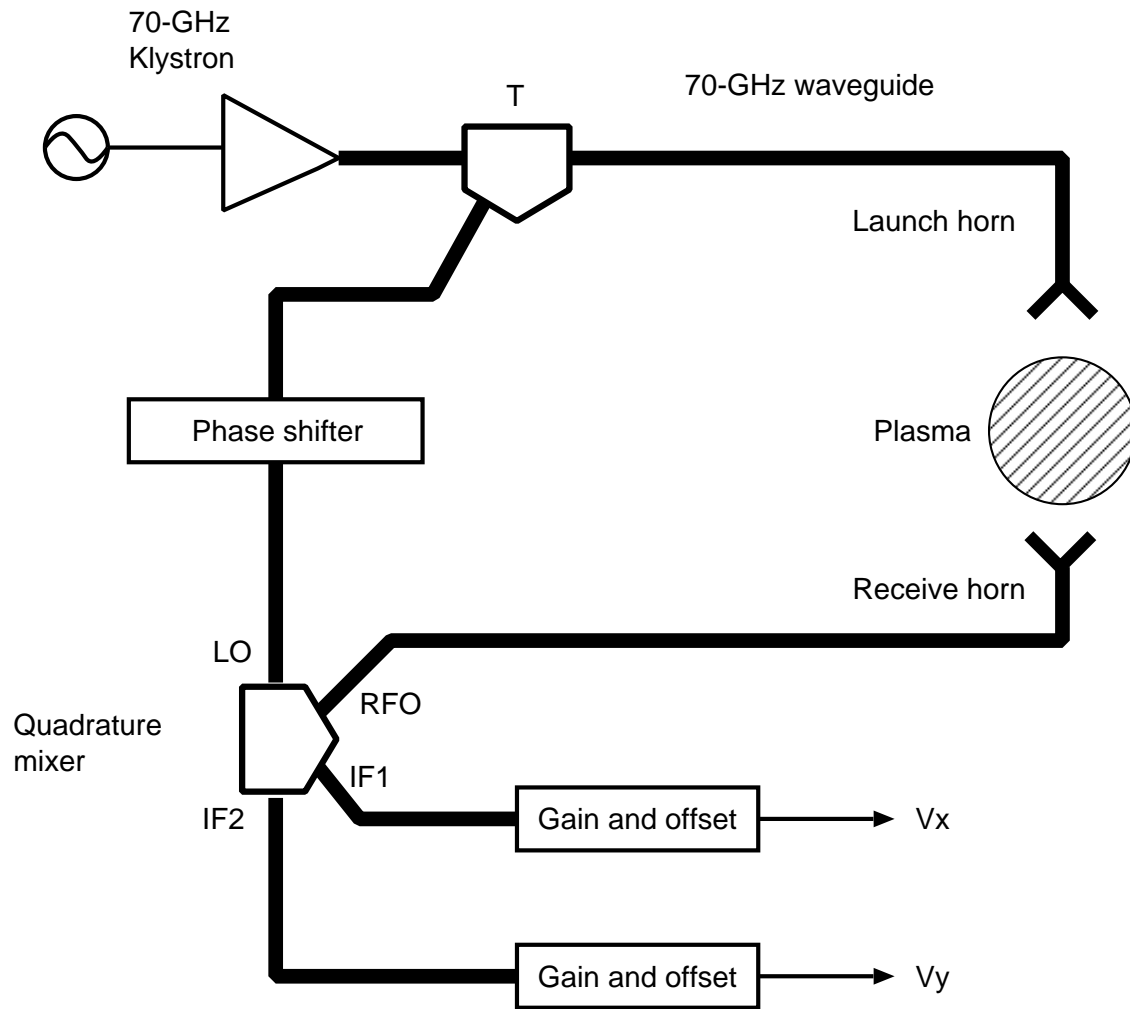


Figure 3.10: Schematic of an interferometer circuit mounted on the Mini-RFTF.

of the oscilloscope are tuned to be circular by adjusting the offset and gain of the outputs.

The phase shift is related to the electron density n_e by

$$\theta(t) = \int_0^L [k_0 - k_{plasma}] dx = \frac{\omega}{c} \int_0^L \left[1 - \sqrt{1 - \frac{\omega_{pe}^2(x, t)}{\omega^2}} \right] dx, \quad (3.10)$$

$$\omega_{pe}^2(x, t) = \frac{n_e(x, t)e^2}{\epsilon_0 m_e}, \quad (3.11)$$

where k_0 and k_{plasma} are the wave numbers in free space and in a slab plasma with width L , respectively, ω is the angular frequency of the beam, ω_{pe} is the electron plasma frequency, e , m_e , c and ϵ_0 denote the electron charge, the electron mass, the speed of light and the permittivity of free space, respectively. Here, the argument of root in Equation (3.10) should satisfy > 0 , that is, measured electron density should be lower than cut-off density: $\omega^2 m_e \epsilon_0 / e^2$. The normalized density profile can be measured by a Langmuir probe so that Equation (3.10) may be integrated numerically. Equation (3.10) is derived from the cold plasma dispersion relation of ordinary wave [56].

Figure 3.11 shows voltage signals from the quadrature mixer, $V_{x,y}$, and analyzed line-averaged density, $n_e l$ profile. Measurements were conducted in the Mini-RFTF with hydrogen gas. The sinuous signals appeared in V_x and V_y around 0.3 msec in the figure indicate the increment of density during the discharge breakdown. The interferometer measurement is also useful to detect low-frequency fluctuations excited in the plasma without disturbance as shown in the figure.

3.3.6 Data accumulation system

Experimental data obtained from the diagnostics of the interferometer, Langmuir probe, or rectified directional couplers are acquired using oscilloscopes: LeCroy[®] 9314A, or Tektronix[®] TDS2024. For RF signals from such as I-V sensor, balanced RF magnetic probe or directional couplers are analyzed by the Hewlett-Packard[®] 8753D network analyzer. Figure 3.12 shows data accumulation system on Mini-RFTF. Data accumulation or storage is conducted with GPIB interfaces and the data is analyzed with National Instruments[®] LabVIEW[®] programs in which data

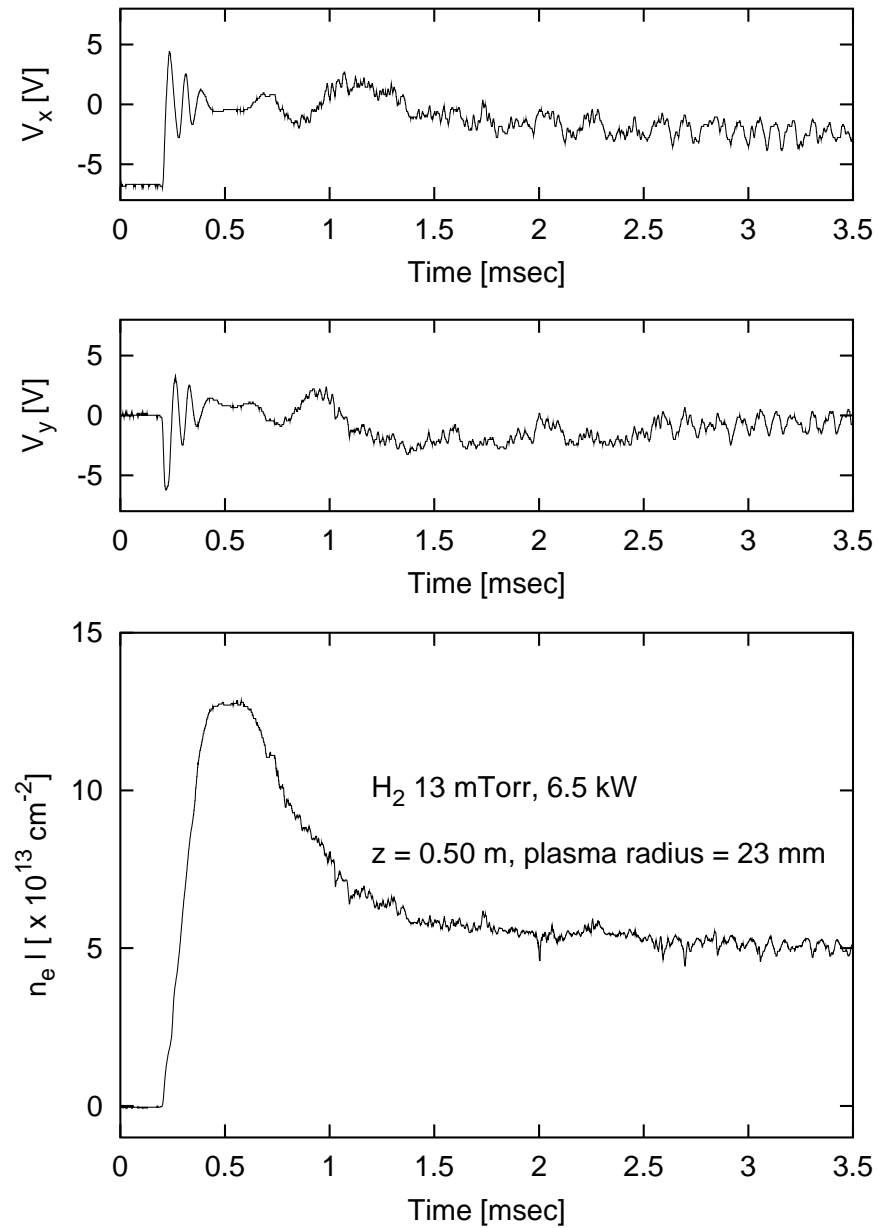


Figure 3.11: Voltage signals from the quadrature mixer and a computed line-averaged density profile measured in the Mini-RFTF.

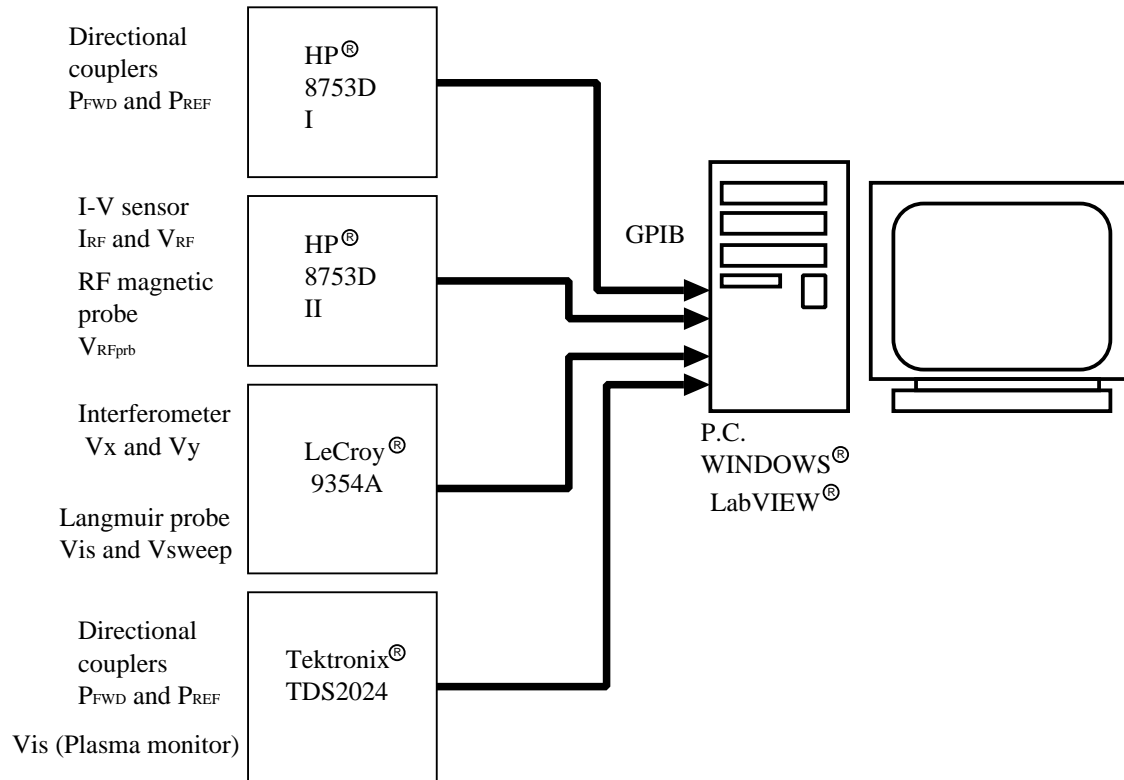


Figure 3.12: Schematic of data accumulation system on Mini-RFTF.

analyses are possible *in-situ*. Manual data store are also available for each measurements diagnostics.

Chapter 4

Comparison of high-density hydrogen helicon plasma experiments with modeling for non-uniform magnetic field geometry

4.1 Introduction

Helicon plasma sources have been applied in many fields [12, 26, 64] for a capability of sustaining high density ($\leq 10^{19} \text{ m}^{-3}$) plasma with high ionization efficiency. Related with numerous experimental studies, several numerical simulations with modeling have been conducted [65–68]. However, these studies have not adequately revealed the contribution of the magnetic field non-uniformity which has been observed in several experiments. For example, in non-uniform magnetic field geometries, compared with uniform geometries, density enhancement operations have been reported [69, 70]. Recent experiments on Mini-RFTF, which will be described in Chapter 6, also found a clear evidence of density enhancement which is strongly related with magnetic field geometries. For the density enhancement measurements for hydrogen on Mini-RFTF, radial density profiles around source region (electron density $\sim 10^{19} \text{ m}^{-3}$) were different from that of expanding region ($\sim 10^{18} \text{ m}^{-3}$). The modeling of RF plasma generation have been conducted by Carter et. al [68] on non-uniform field geometries including a flux-tube-averaged transport model. To

reveal the mechanism of density enhancement, further improvements of transport models including axial diffusion are required. In this chapter, on-going development of transport model; comparisons of the RF modeling by Carter et. al [68] and measured density profiles on source region by the interferometer system are discussed. Oscillating magnetic field profile detected by the balanced-RF magnetic probe, described in Chapter 3, is compared with a simulated electromagnetic field. Developments of robust RF plasma generation modeling will lead to optimizations for RF generating plasma applications represented as plasma processing and plasma propulsion. Following this section, the RF modeling and power transport are reviewed in Section 4.2. After a description of the Mini-RFTF experiments conducted for the modeling in Section 4.3, comparisons between the simulation and experiments are discussed in Section 4.4. Conclusions are given in Section 4.5

4.2 Review of RF modeling and power transport

The modeling of the experiments is performed with EMIR3 RF code [68] by iterating between a high-resolution RF calculation and a transport model based on the power deposition given by the RF calculation. A brief description of EMIR3 is given here.

4.2.1 RF modeling

Maxwell's equations for the linearized cold plasma response can be written as [45]

$$\begin{aligned} \nabla \times \vec{E} &= i\omega\vec{B}, \\ \nabla \times \vec{B} &= \mu_0\vec{J}_{ext} - i\omega\epsilon_0\mu_0\tilde{K}\cdot\vec{E}, \\ \tilde{K} &= \begin{pmatrix} S & -iD & 0 \\ iD & S & 0 \\ 0 & 0 & P \end{pmatrix}, \vec{E} = (E_{\perp 1}, E_{\perp 2}, E_{\parallel}), \end{aligned} \quad (4.1)$$

where $P = 1 - \Sigma_j(\omega_{pj}^2/\omega^2)$, $S = 1 - \Sigma_j\omega_{pj}^2/(\omega^2 - \omega_{cj}^2)$, and $D = \Sigma_j(\omega_{cj}/\omega)\omega_{pj}^2/(\omega^2 - \omega_{cj}^2)$ describes the Hall contribution to the plasma current. Here ω is the operating RF frequency, $\omega_{cj} = q_j B_0/m_j$ is the cyclotron frequency of the j^{th} species, $\omega_{pj} = \sqrt{q_j^2 n_j/(\epsilon_0 m_j)}$ is the plasma frequency for the j^{th} species, ϵ_0 is the permittivity of free space, and q_j, m_j , and n_j denote the species charge (with sign), mass, and density of the j^{th}

species, respectively. In these equations, \vec{E} and \vec{B} are the complex RF electric and magnetic field vectors, respectively, with implicit $\exp(-i\omega t)$ time dependence, and J_{ext} represents RF current sources from the antenna; all units are MKS. The $\perp 1$ and $\perp 2$ directions are orthogonal and are perpendicular to the direction for the static magnetic field. The \parallel direction is that of the static magnetic field. Cases retaining finite \vec{E}_{\parallel} are computationally demanding because very-short-wavelength electrostatic modes at the lower hybrid resonance must be resolved accurately to obtain good numerical solutions.

The RF fields are expanded in a periodic Fourier sum in the azimuthal coordinate, $\theta(=\perp 2)$, to reduce the three dimensional field problem to a sum over two-dimensional solutions weighed by the Fourier spectrum of the antenna. Absorption is introduced in the cold plasma model by adding an imaginary collision frequency to the RF frequency. For the calculations presented here, the current along the strip is assumed to be constant ($\nabla \cdot \vec{J}_{ext} = 0$), ignoring any direct capacitive coupling. (Not that electrostatic modes in the plasma can still be excited because of inhomogeneities in the antenna and the plasma.) The RF calculations presented here used 130 radial and 1200 axial grid locations to resolve short wavelength surface modes near the lower hybrid resonance.

4.2.2 Transport modeling

To obtain a self-consistent plasma density profile, we use a flux tube averaged power balance with a particle balance in which the plasma source rate is determined from the deposited RF power, similar to work by Yasaka et al. [71].

The transport model assumes that power deposited axially upstream of the maximum magnetic field is rapidly carried by parallel thermal conduction along field lines upstream on the flux tube. The plasma flowing downstream of the magnetic field maximum is assumed to expand rapidly without contributing significantly to the source.

The plasma source is a complicated function of electron temperature and density as well as the densities of any neutral species in the device. These quantities are not well known spatially and are very difficult to model. However, a robust model can be obtained by averaging the source over a magnetic flux tube, $\psi \approx \pi r^2 B_z(z)$, along a distance of field line, s , such as $S(\psi, s) \rightarrow S(\psi)$, and assuming the source rate on

a flux tube is proportional to the total RF power deposited on that tube, where $B_z(z)$ is the external magnetic field strength at distance z . Such a model provides the average value for the electron density on a flux tube and allows parameterization of the density along a field line that is consistent with the flux tube average. For a uniform geometry, separation of variables indicates a parabolic shape for the density distribution $n(\psi, s)$ along a field line. Assuming a weakly variation in the parallel diffusion along a line, one can consider a flux tube average by using

$$n(\psi, s) \approx a(\psi)s^2 + b(\psi)s + N_u(\psi), \quad (4.2)$$

where N_u is the density at the upstream boundary of a field line. The axial fitting parameters for the density dependence along the field line, a and b in Equation (4.2), are determined by the boundary conditions at each end of a field line. In a "long-thin" approximation, the density evolution follows;

$$S(\psi) \approx C_z(\psi) \langle n \rangle / L_{eff} - 4\pi \frac{\partial}{\partial \psi} \langle B_z(z) D_{rr} \rangle \psi \frac{\partial \langle n \rangle}{\partial \psi} \quad (4.3)$$

where $\langle n \rangle$ is the average plasma density on the flux tube, S is the ionization source rate, D_{rr} is the radial diffusion coefficient, C_s is the sound speed, and L_{eff} is the effective confinement length of the flux tube, including any mirror or collisionally enhanced confinement effects.

L_{eff} can be determined by the loss rates at each end of a flux tube. For mirror-constricted sonic flow at the end,

$$\left[D_{\parallel} \frac{\partial n}{\partial z} \right]_{z_d} = -\frac{C_s N_d}{\sqrt{R_d}}, \quad \left[D_{\parallel} \frac{\partial n}{\partial z} \right]_0 = -\frac{C_s N_u}{\sqrt{R_u}} \quad (4.4)$$

gives

$$L_{eff} = \frac{z_d}{2} \left[\frac{2\sqrt{R_u R_d} + 2\alpha(\sqrt{R_u} + \sqrt{R_d})/3 + \alpha^2/6}{\sqrt{R_u} + \sqrt{R_d} + \alpha} \right] \quad (4.5)$$

where the upstream mirror has a mirror ratio of R_u , and the downstream mirror has a mirror ratio of R_d . Mirror ratios are determined from the midpoint between the boundary condition locations on a field line. The densities, N_d and N_u , in Equations (4.4) and (4.5) are located, respectively, at the upstream ($z = 0$) and downstream ($z = z_d$) locations for each field line. The parameter $\alpha = z_d/2\lambda_e$ is the ratio of half the distance along a field line to the electron collisional mean free path: λ_e .

A power balance is required to complete the particle conservation equation. Rather than attempting to solve for the electron temperature or distribution function, we choose a simple power balance on a flux tube to complete the system:

$$P_{rf}(\psi) \approx C_s(\phi) \langle n \rangle (\psi)(E_i + \phi)/L_{eff} - 4\pi \frac{\partial}{\partial \psi} \langle B_z(z) D_{rr} \rangle (E_i + \phi) \psi \frac{\partial \langle n \rangle}{\partial \psi}, \quad (4.6)$$

where P_{rf} is the RF power delivered to the plasma and E_i is the energy cost per electron/ion pair. Terms proportional to E_i in Equation (4.6) represent the power required to ionize the neutral gas. Terms proportional to the electric potential of the flux tube, ϕ , represent power lost because of the kinetic energy carried by ions as they fall through the electrostatic potential. Typically for Mini-RFTF, $\phi \sim T_e$ is much less than $E_i \geq 36$ eV, and one observes that the power balance is dominated by the ionization process rather than the kinetic energy of the escaping plasma.

The insight offered by the parabolic model helps to shed light on the effects of the axial inhomogeneity of the magnetic field on density, and in any case, the density drops over a short radial scale length where the outer flux tubes have very short magnetic field connection lengths.

Numerical evaluation of the flux-tube-averaged quantities are obtained by discretizing ψ and by numerically mapping the cylindrical computational grid onto the ψ grid. Equation (4.6) is then solved numerically for an initial density profile and is iterated to convergence by using the RF results from the previous EMIR3 calculation to calculate a new density profile based on Equation (4.6). The axial dependence that maintains the flux tube average is then applied. Transport parameters in Equation (4.6) are estimated with the formulas found in NRL book [72].

4.3 Experimental set-up

The details of experimental setup are described in Chapter 3. External magnetic fields were applied using the SOL coil and MR1 coil giving $R_u = 0.11$ and $R_d = 6.9$ as shown in Figure 4.1 where a dotted line is the high-density limit of the lower hybrid resonant magnetic field strength $B_{lh} = 0.0322$ T for hydrogen. p Hydrogen gas was fed into the discharge tube from the gas-inlet port with 12 mTorr ($\alpha \approx 14$) and RF net power of 2.8 kW with frequency 21 MHz was supplied to the heli-

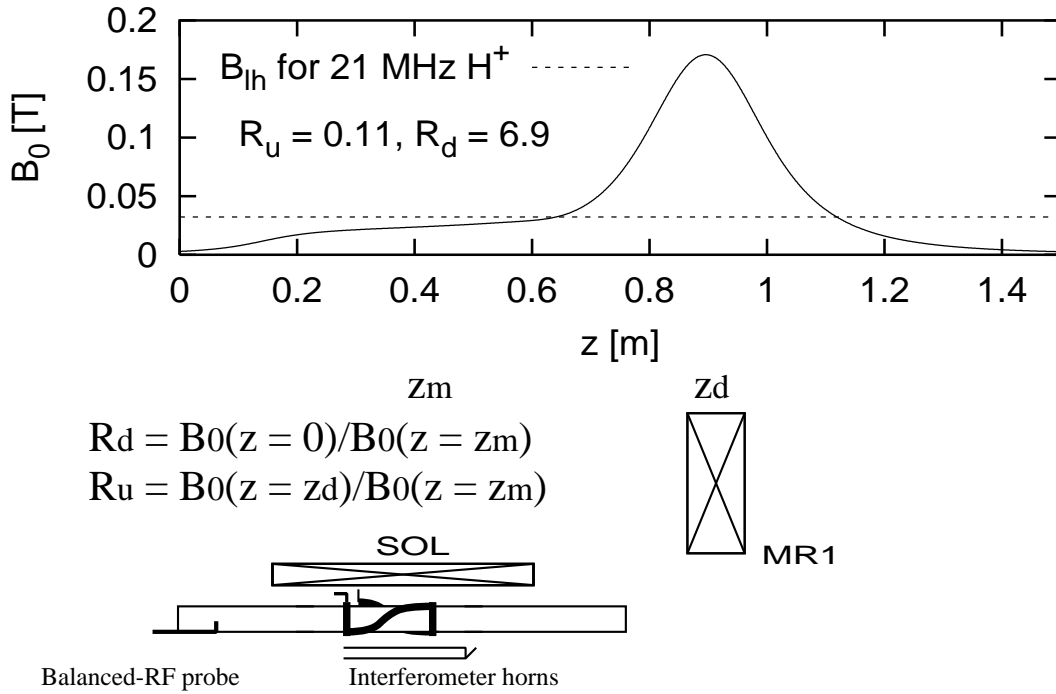


Figure 4.1: External magnetic field configuration with flux tube.

cal antenna. These experimental conditions were considered as collisional region, $\alpha \geq 2\sqrt{R_u}, 2\sqrt{R_d}$.

Both the axial movable interferometer horns and balanced-RF magnetic probe were used to measure axial line-averaged density and oscillating axial component of magnetic field, respectively in order to compare with simulation results.

4.4 Comparison between the model and experiments

Transport comparison

Plasma profile comparisons between experiments and the results of EMIR3 calculation are shown in Figure 4.2. Figure 4.2 (a) shows a radial electron density profile from EMIR3 code (solid line) including the transport model which described in the

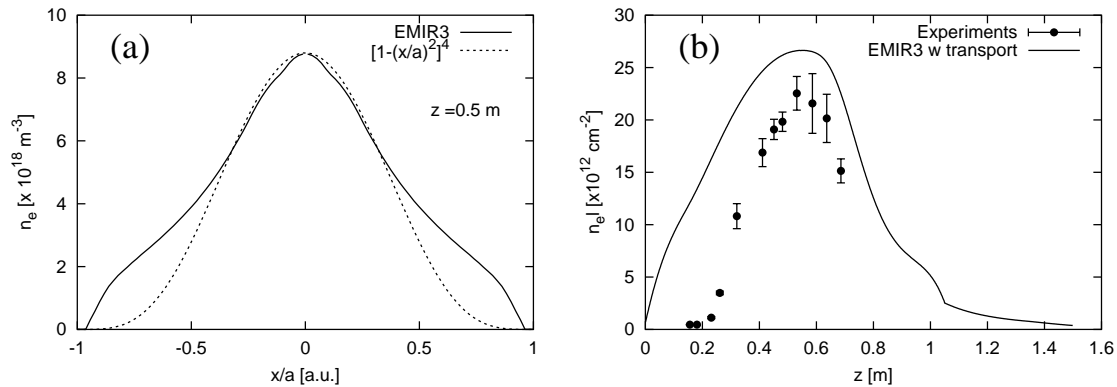


Figure 4.2: Plasma density profiles from experiments and the results of EMIR3 code including transport model.

previous section and a parabolic-like profile (dashed line). Figure 4.2 (b) shows axial line-averaged electron density profiles from the experiment (closed circles with error bars) and EMIR3 code (solid line).

The calculated radial plasma density profile shown in Figure 4.2 qualitatively agrees with a density-jumped helicon plasma behavior represented here as parabolic-like profile which is generally detected on the Mini-RFTF experiments. The experimental results from the interferometer, shown in Figure 4.2 (b), indicate that the flux tube average using a parabolic fit along field lines, as assumed in Equation (4.2) is relatively simple to describe all of the observed behavior. While overall plasma volume estimated from the measured line-averaged electron density profile is reasonably obtained with the parabolic fit in the model including collisional damping power depositions, the measurements clearly show that the dependence of the density along field lines is more complicated than a simple parabolic fit can describe.

Flux-tube-averaged density profile gives a good insight for helicon plasma design, however, experiments in a strong non-uniform magnetic field geometry, which will be described in another chapter, shows an importance of the estimation of the axial power deposition. Another cause of the reduction in density observed upstream in the experiments is introduction of gas and recycling in the upstream section. Thus, the axial variation in the neutral species parameters results in a non-uniform pressure imbalance that is not accounted for in the original model of reference [68]. Proper modeling of these behaviors would require a two-dimensional transport model

coupled with a gas model.

Electromagnetic field comparison

It is important to have the plasma parameters in the experiment and model as consistent as possible before comparing the RF fields because the dispersion of the waves of interest depends on density and magnetic field. Because the density profile can significantly affect the wave propagation, it is important that the density profiles match the experimental measurements as closely as possible. Thus, we modify the densities obtained from the simple flux-tube-averaged transport model until they match the interferometer measurements. This modification is made by simply multiplying the model density by a hyperbolic tangent weighting in the axial direction

$$n(r, z) = n_{fta}(r, z)[f_d + f_u + (f_d - f_u)\tanh[(z - z_i)/z_s]/2] \quad (4.7)$$

where n_{fta} is the density profile provided by the flux-tube-averaged model shown in Figure 4.2 (b) as solid line, f_d is the asymptotic factor applied to the downstream of the density profile, and f_u is the asymptotic factor applied to the upstream.

Figure 4.3 shows a modified axial line-averaged electron density profiles (solid line) by Equation (4.7) with factors; $f_d = 0.01$, $f_u = 0.80$, $z_i = 0.32$ and $z_s = 0.10$, and experimental profile (closed-circles). From Figure 4.3, the resulting axial density dependence then provides good agreement with the experimental measurements.

RF modeling code is used to run without transport model for comparison between experimentally detected electromagnetic field and calculated field profiles from the EMIR3 RF modeling.

Figure 4.4 shows an oscillating magnetic field profile of (a) amplitude and (b) phase shift. In Figure 4.4, experimental results are shown as closed circles and simulation results are as solid curve. There are qualitative agreement between model and experiments for both amplitude and phase shift. Especially, phase shift shows both qualitative and quantitative agreements with model. The amplitude mismatch detected around antenna locations from $z = 0.28$ to 0.45 in Figure 4.4 were probably strong near field contributions from the antenna in which a local-resolution of probe was not sufficient to resolve. As for helicon wave propagation, simulation results and experiments has an appropriate agreement.

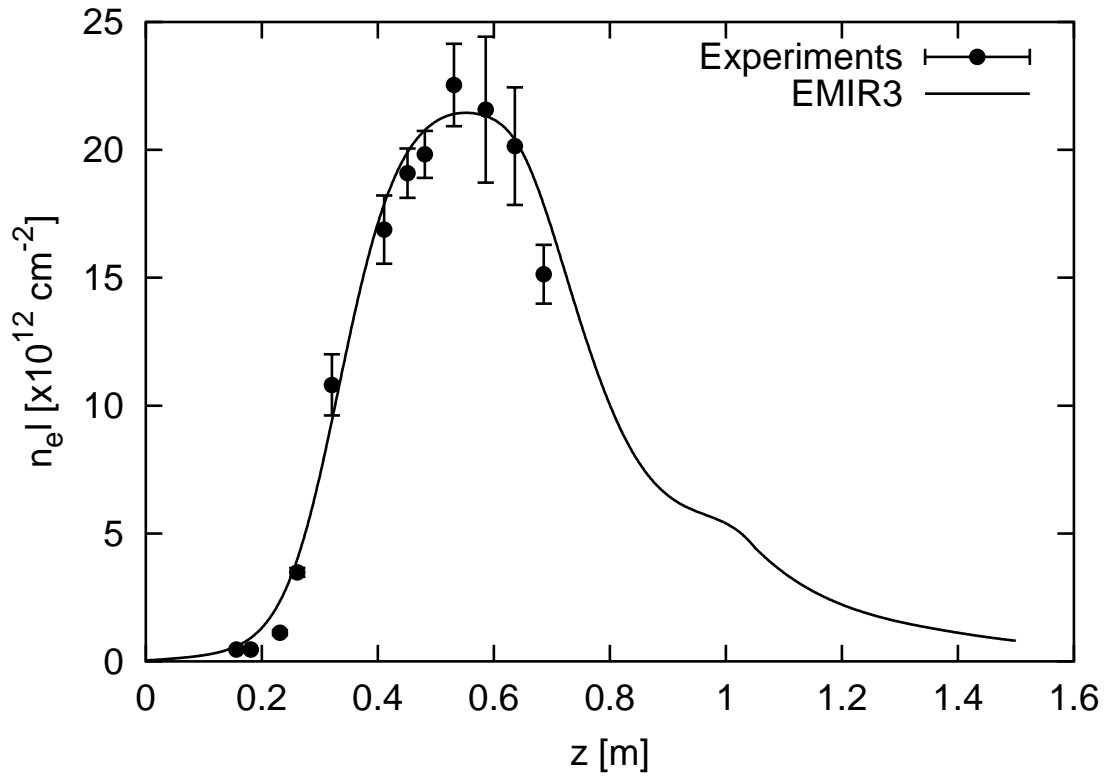


Figure 4.3: Modified plasma profile on EMIR3 to fit the experiment.

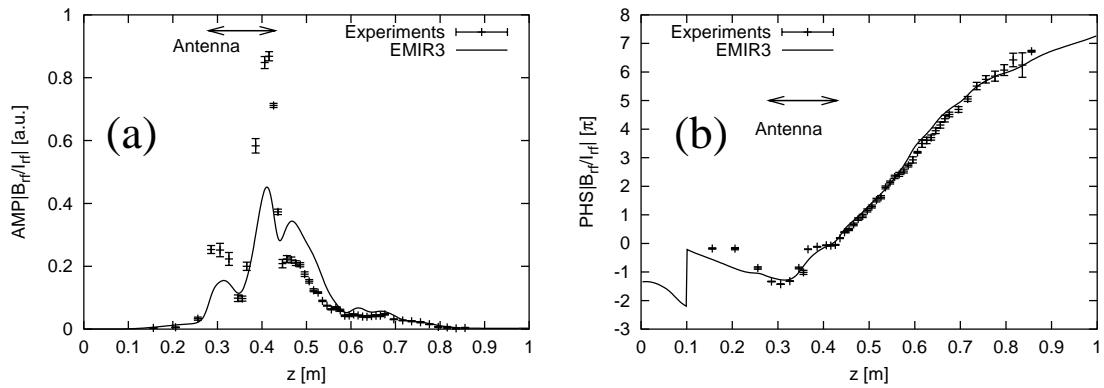


Figure 4.4: Axial oscillating magnetic field (a) amplitude and (b) phase shift of experiments (closed-circles) and RF modeling by EMIR3 (solid line).

From the results shown in Figure 4.4, it is found that as far as correct density profiles were obtained, electromagnetic fields can reasonably be calculated from EMIR3 code since both amplitude and phase shift of oscillating magnetic fields obtained from EMIR3 show qualitative agreements with experiments.

Figure 4.5 shows oscillating electric fields and power density profiles from EMIR3 code as well as a plasma density profile and flux tube mapping. From Figure 4.5, it is found that $E-$, right-hand circular polarized helicon wave, is excited and then it can propagate into downstream rather than $E+$ mode. From the profiles of electric fields amplitudes and power density, $E-$ mode deposits its power on axis around the source regions, which results in helicon plasma sustainment. A power deposition from inductive field, represented as $E_{parallel}$, is also significant at the edge of plasma around the antenna location. Plasma generated in this region is rapidly lost in the edge and demotes the efficiency of a plasma source. It is suggested to reduce this coupling to the edge plasma by modifications to the antenna such as adding a Faraday shield to reduce the parallel electric field in the plasma edge [73].

4.5 Conclusions

Transport model with flux tube averaging was found too simple to demonstrate experiments results. However, as far as correct density profile is applied, RF modeling on EMIR3 has revealed a qualitative agreement with measured RF profiles and then excited right-hand circular polarized helicon wave was found responsible for plasma sustainment. Further improvement of an axial transport model including local power deposition and neutral gas profiles will give more robust modeling of helicon plasma in a nonuniform magnetic field.

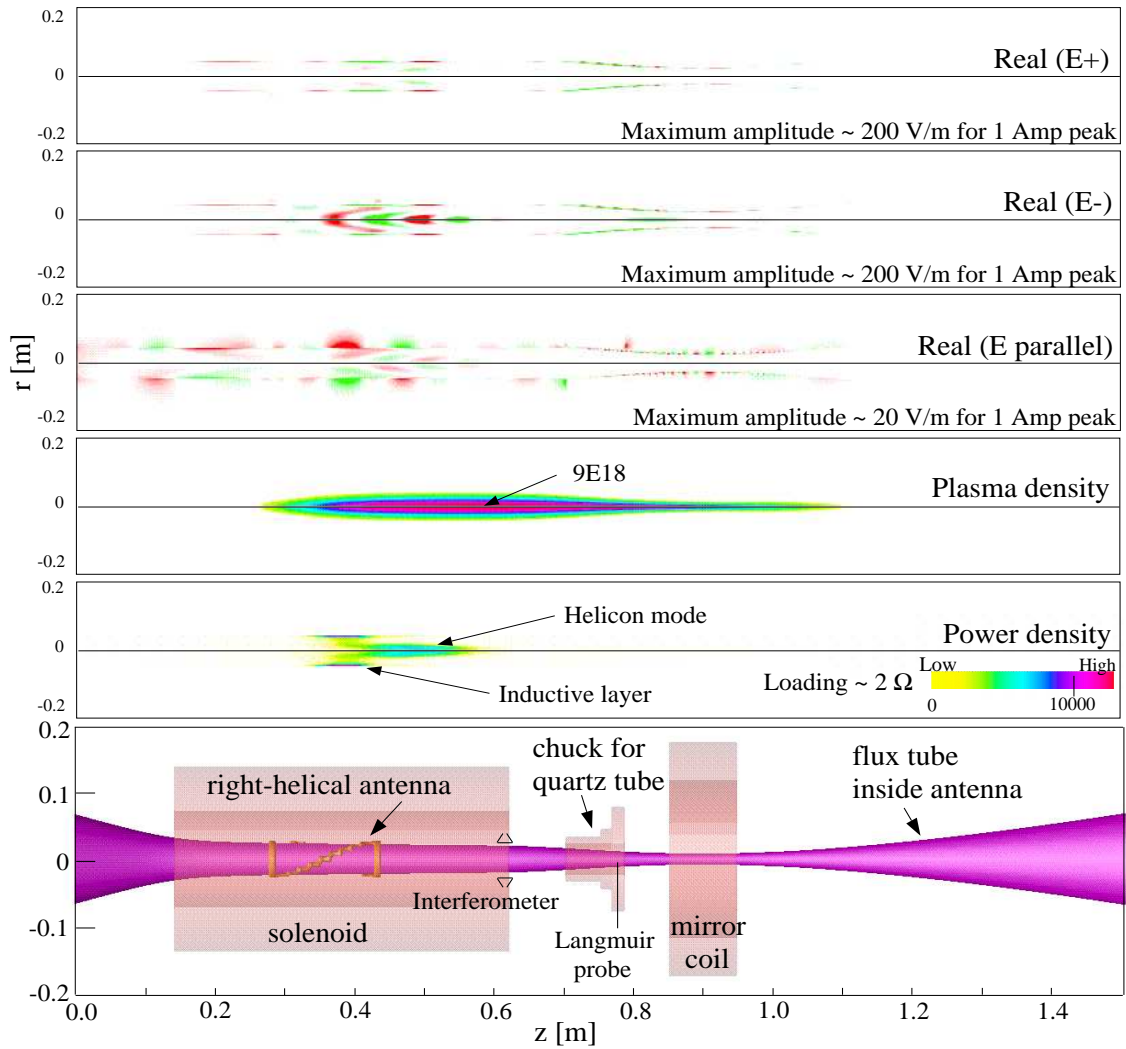


Figure 4.5: EMIR3 results.

Chapter 5

High-density hydrogen helicon plasma in a nonuniform magnetic field

5.1 Introduction

Helicon plasma sources are used for many applications requiring high-density plasma, including plasma processing and fusion component testing [22, 23, 27, 74]. Most helicon research to date has been focused on devices having a uniform static magnetic field and relatively heavy ions, such as Ar or N₂. Helicons having nonuniform magnetic fields and heavy ions have been examined by Guo et al., showing that a strong axial density gradient associated with nonuniform magnetic fields can contribute to absorption of the wave fields and high source efficiency [75]. However, many applications require operation with both an axial magnetic field variation and light ions, such as H₂ or He. These light-ion species have not been studied in the same detail as heavier ions, partly because of the increased difficulty in obtaining good discharges. In general, we find that helicon operation using light ions is much more sensitive to the magnetic field strength and geometry than operation using heavy ions.

Effects caused by the lower hybrid resonance have been studied extensively for space plasma [76, 77] and fusion research [78], and the lower hybrid resonance also plays a role in helicon operation. For helicon plasmas with heavy ions, the lower hybrid resonance has been investigated for optimal operation [79–81] and for ion heating [82, 83]. For experiments with uniform magnetic fields, especially for the

case of hydrogen, it has been reported that the plasma density did not increase with magnetic field strength, as expected for the helicon mode, and that the best operation was obtained with a lower hybrid resonance present [84, 85]. We found that optimal operation can be obtained away from the lower hybrid resonance for light ions in a nonuniform magnetic field, so long as sufficient RF power is available.

Many other features of helicon behavior have been reported for devices having both uniform and nonuniform magnetic fields. Low-frequency instabilities in helicon discharges with uniform axial magnetic fields have been investigated [86]. The effects of cross-field and axial transport with and without the lower hybrid resonance have been used to explain some aspects of light-ion plasma generation in axially varying systems [68]. Surface processes in hydrogen helicon plasma have been studied in uniform [87] and torus plasmas [28, 88]. However, many mechanisms for light-ion helicon plasma production have not been fully investigated.

In this chapter, we utilize the capabilities of the Mini-Radio Frequency Test Facility (Mini-RFTF) [33, 68] to control and vary the axial static magnetic fields so that helicon operation with light ions can be systematically studied. A better understanding of light-ion operation in geometries with inhomogeneous static magnetic fields demonstrates that efficient light-ion sources are possible for many applications, including the testing of fusion components and high specific-impulse propulsion systems [12]. We also find that plasma operation for hydrogen in the axially varying magnetic fields of Mini-RFTF is significantly different from results reported in the literature for uniform magnetic field devices.

This paper presents experimental measurements of the RF magnetic fields in high-density ($n_e \simeq 10^{19} \text{ m}^{-3}$) hydrogen helicon plasma over a range of power and gas pressure for several magnetic field strengths and axially inhomogeneous geometries. After this section, the experimental set-up is given in Section 5.2. Sections 5.3.1 and 5.3.2 contain plasma measurements obtained by changing the static magnetic field configuration, including both the static field strength and shape. Also in Section 5.3.2, we demonstrate that high-density plasma operation with light gases is not limited to RF frequencies above the high-density limit of the lower hybrid resonance if enough power is supplied. In Section 5.4, analyses of density measurement and oscillating magnetic field are given to demonstrate the contributions of the first and second radial helicon modes. In Section 5.5, we discuss our conclusions that the

axial focusing of the magnetic field gives a wide density range by allowing the second radial mode to contribute to high-density plasma production. We also discuss our finding that high-density operation is not necessarily limited to magnetic fields near the lower hybrid resonance.

5.2 Experimental set-up

Details of experimental device and diagnostics are described in Chapter 3. Here, we address experimental conditions related to the following experiments described in this chapter. H_2 gas was used over a range of pressure from 3 to 13 mTorr. Two power supplies are available to energize the antenna. One provides up to 2 kW and the other up to 20 kW. In these experiments, we used up to 5 kW at 21 MHz. We used the 2-kW power supply for low-power operation and the 20-kW power supply for high-power operation. Forward and reflected power are monitored by directional couplers mounted between the power supply and a matching network. The match was tuned to keep the reflected power less than 20% of the forward power. Diagnostics include the 70-GHz interferometer that can be scanned axially ($z = 0.1$ to 0.7 m) and the radially movable single Langmuir probe installed at the end of quartz tube ($z = 0.78$ m). The balanced RF magnetic probe is used to scan the axial component of the oscillating magnetic field both axially and radially. Axial scans are performed by sliding the probe through a feed-through motor drive on the upstream end of the system and radial scans are performed by rotating the probe. The magnetic probe and a current-voltage sensor mounted on the output of the matching network were connected to a network analyzer. The amplitude and phase difference between the current signal and magnetic probe were obtained by a tuned receiver mode of the network analyzer to synchronize measurements in the plasma with the driven antenna current.

Figure 5.1 presents pulsed operation signals typical of those on Mini-RFTF in the experiments described in this chapter. The 21-MHz RF was typically pulsed with a 35 ms pulse width and 1.8% duty rate. Measurement signals of ion saturation current, I_{is} , taken by the Langmuir probe and line-averaged density, $n_e l$, taken by the interferometer horns were averaged over 5 ms during the middle of the pulse (0.008 – 0.013 sec) as indicated in Figure 5.1. Forward and reflected power, P_{FWD}

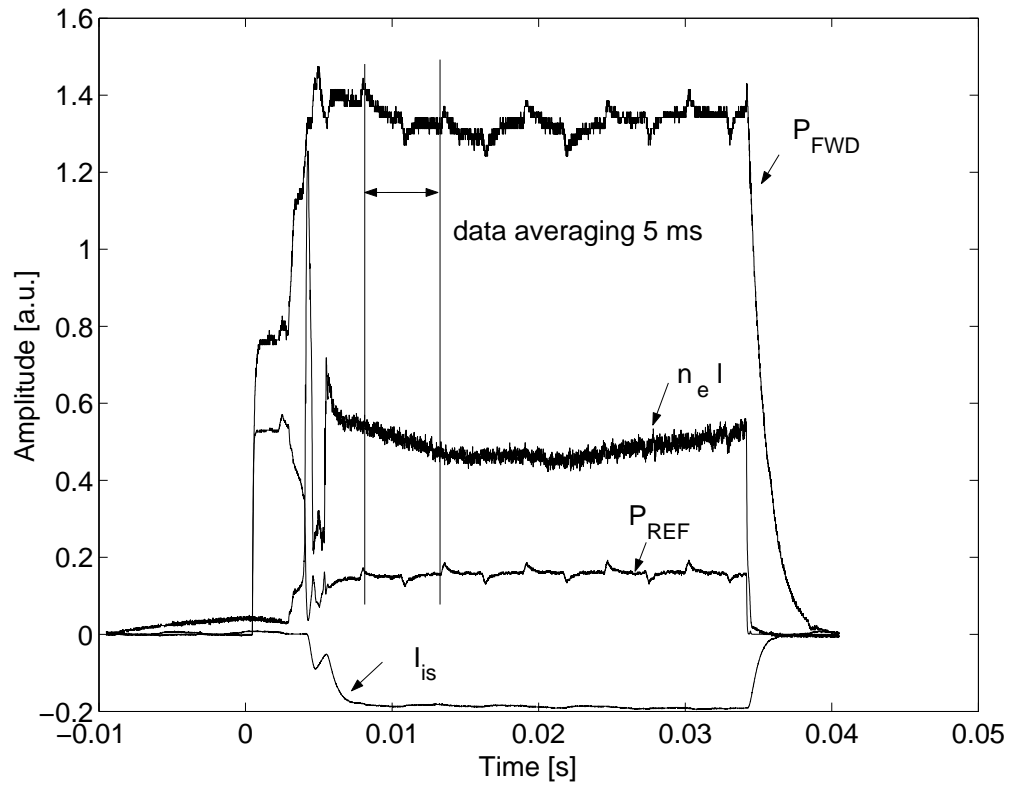


Figure 5.1: Pulse operation signals on Mini-RFTF for experiments described in this chapter. The 21-MHz RF was typically pulsed with a 35 ms pulse width and 1.8% duty rate. Measurement signals were averaged over 5 ms during the middle of the pulse (0.008 – 0.013 sec).

and P_{REF} , obtained from directional couplers are also shown in Figure 5.1. Glitches shown on P_{FWD} and P_{REF} were AC noise came from DC power supply to energize a static magnetic coil. However, the influence to plasma was negligible.

5.3 Effects of static magnetic geometry and field strength

The maximum stable plasma density was found to depend on the available power as well as the magnetic field geometry. In Section 5.3.1, we describe experiments to explore the effect of the magnetic field configuration on helicon operation for up to 2 kW of power. At this power level, characteristics of the helicon wave in high-density operation could be found at two values of the magnetic field near the antenna. One value was nearly zero and the other was near the lower hybrid resonance. In Section 5.3.2, operation with over 3 kW of power is described, showing that this range for high-density helicon operation is dramatically altered with sufficient power and becomes roughly independent of the lower hybrid resonance location. In Section 5.4.1, results from mapping the RF magnetic field with a loop probe are described, indicating that several radial and axial wavenumbers play a role in high-density helicon operation.

5.3.1 Source magnetic field configuration

In the first set of experiments, the dependence of hydrogen helicon plasma operation on the static magnetic flux shape was examined as shown in Figure 5.2. Both Langmuir probe and magnetic probe measurements were made for these experiments. The magnetic probe was rotated 1 cm off the axis and located at a fixed position 8.5 cm from the downstream end of the antenna ring ($z \approx 0.5$ m in Figure 5.2). The plasma was unstable for the full range of fields using pressure < 13 mTorr, so a fixed gas pressure of 13 mTorr was used for stable operation in this set of experiments.

The magnetic flux configuration was varied by scanning the solenoid coil current, I_{SOL} (surrounding the antenna) from 0 to 100 A in 20 A increments. Axial magnetic field strengths for these configurations are shown in Figure 5.2. B_{LH-HD} designates the magnetic field for which $\omega = \omega_{LH-HD}$ in the bulk plasma for 21-MHz RF operation, where ω_{LH-HD} denotes the high-density limit of the lower hybrid frequency

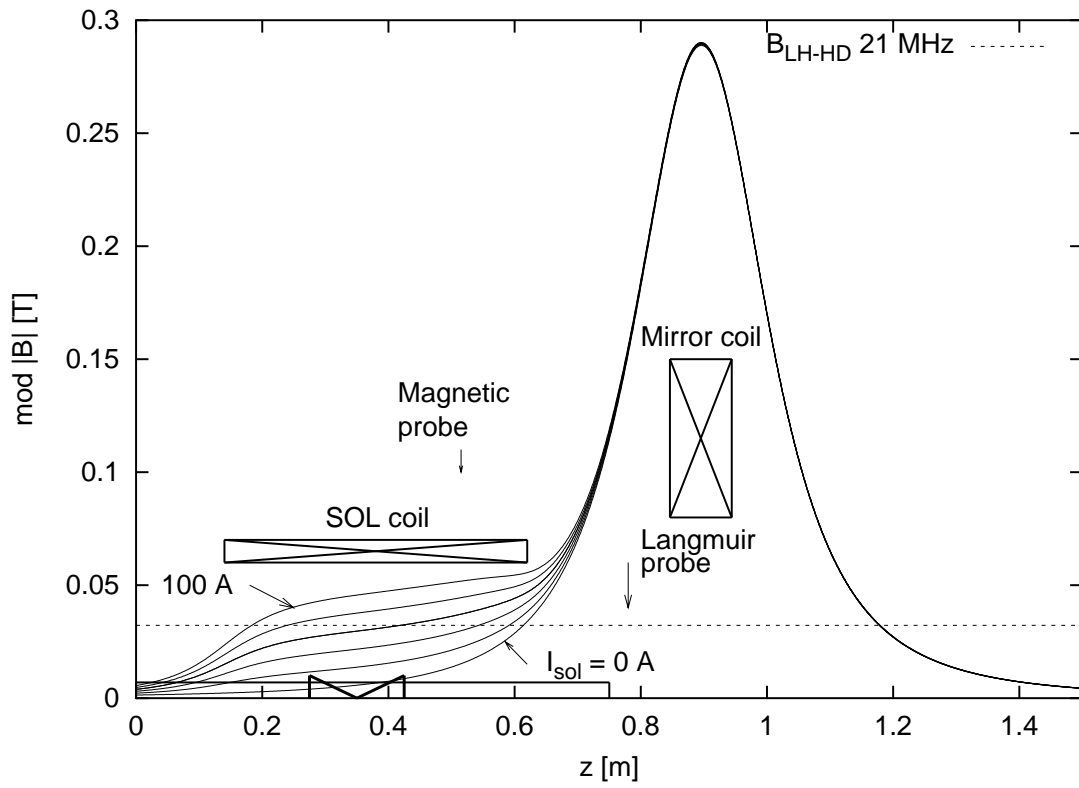


Figure 5.2: Static magnetic field configuration for keeping the downstream mirror coil current constant. Solid lines show the magnetic field configuration for every 20 A of the antenna region coil (SOL coil) current, I_{SOL} . The dashed line is the high-density limit of the lower hybrid resonant magnetic field strength B_{LH-HD} (0.0322 T for 21 MHz).

described in Chapter 2. The solenoid coil is capable of carrying up to 200 A, so it is possible to increase the magnetic field in the antenna region to over $2 B_{LH-HD}$.

Figure 5.3 shows experimental results when I_{SOL} is changed using up to 2 kW of power. Part (a) shows the ion saturation current obtained by the Langmuir probe and (b) shows the wave number computed from a magnetic probe at a fixed position. In Figure 5.3(b), wave numbers were computed from the measured phase shift of B_z/I_{rf} with the assumption that the wave was launched from the end of the antenna ring because the probe location was fixed in these experiments. The validity of the assumption was supported by the axial scans of magnetic fields described later for low-power operation (2 kW).

For power levels up to 2 kW, Figure 5.3(a) shows that the maximum ion saturation currents were obtained with I_{SOL} between 50 and 60 A, where the lower hybrid resonance occurs near the antenna region as shown in Figure 5.2. Assuming a typical value of 4 eV for the electron temperature detected on Mini-RFTF, the electron density is supposed to be $> 10^{18} \text{ m}^{-3}$ for this range of I_{SOL} . High-density helicon plasma was also sustained for $I_{SOL} \approx 0$ A. Increasing the solenoid coil current from 0 A to 5 A resulted in a drop in density by a factor of 2. The density continued to decrease monotonically with increasing I_{SOL} until the high plasma density mode reappeared with the lower hybrid resonance near the antenna. The high-density regions, where $I_{SOL} \approx 0$ and $50 \text{ A} < I_{SOL} < 60 \text{ A}$, were confirmed to be jumps into a helicon plasma mode as measured by the magnetic field probe.

While the precise identification of the waves sustaining the discharge requires accurate measurements discussed later, phase shift measurements provide clues about the parallel wave numbers for the dominant modes in the discharge. The parallel wave number determined from these measurements are shown in Figure 5.3(b) for comparison with the behavior from the simple helicon dispersion relation, $k_z \propto n_e/B_0$, where k_z is an axial wave number parallel to the background magnetic field, B_0 , as described in Chapter 2. For the low-density region where $10 \text{ A} < I_{SOL} < 50 \text{ A}$, the wavelength remains short compared with the device scale. For coil currents between 10 A and 40 A, the wave number decreases with increasing coil current while the density remains somewhat constant, in reasonable agreement with the helicon plasma dispersion relation. However, for I_{SOL} between 40 A and 50 A, the k_z remains almost constant or even increases with increasing magnetic field. As I_{SOL} increases

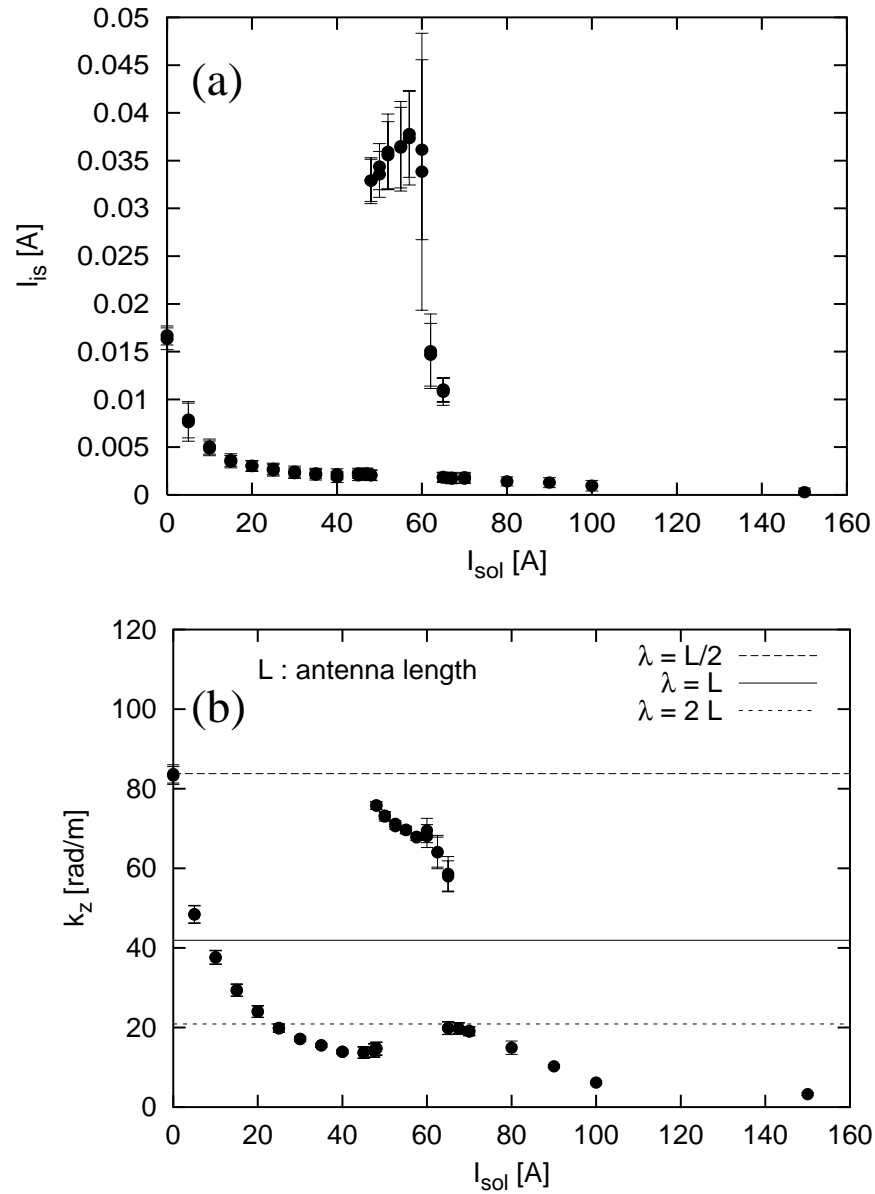


Figure 5.3: Changing the magnetic field profile in the antenna region strongly affects the helicon performance at low-power. (a) The ion saturation current measured by the Langmuir probe. (b) The wave number computed from measured phase shift of B_z/I_{rf} by the magnetic probe assuming that the waves are launched from the antenna ring.

to between 50 A and 65 A, the density jumps to a much higher, but nearly constant level, and the scaling of k_z is again in reasonable agreement with the helicon plasma dispersion relation. From I_{SOL} values of 65 to 70 A, k_z becomes nearly constant. For $I_{SOL} > 70$ A, k_z again decreases with a magnetic field near the antenna until it becomes comparable to the device length for $I_{SOL} > 100$ A.

It is important to determine how the plasma is sustained in light-ion helicon sources, especially for the high magnetic field region, $B_0 > B_{LH-HD}$. In particular for the hydrogen discharges shown here with high magnetic field, the density drastically decreases for $B_0 > B_{LH-HD}$, while helicon experiments using heavy ions typically show a much more gradual decrease in density with an increase in magnetic field [85, 86] near the lower hybrid resonance. For the 2-kW power supply used in this set of experiments, the density for helicon plasma operation seems to be limited by the presence of the lower hybrid resonance frequency. However, as discussed in Section 5.3.2, this limitation appears to be much more related to the available power than to the presence of a lower hybrid resonance.

These experiments with high axial nonuniformity also show that hydrogen helicon plasmas can be well sustained with very low magnetic fields in the antenna region. Similar behavior for hydrogen helicon plasmas having two peaks for varying magnetic field strengths were also observed under the uniform magnetic fields [84, 86].

5.3.2 Isolating effects of the static magnetic field geometry

Changing the magnetic field geometry in Mini-RFTF can result in simultaneous changes in boundary conditions, transport, and RF propagation. To identify the effects of changing the geometry, three different magnetic configurations were considered, as shown in Figure 5.4. For these studies, up to 5 kW of RF power was available, and significant changes from the behavior shown in Figure 5.3 were observed. The electron line-averaged density and ion saturation current were measured with the interferometer and the Langmuir probe, respectively, for these three magnetic field flux configurations. The interferometer horns were located 8.5 cm downstream from the antenna ring.

In Figure 5.4 we identify the three magnetic field flux configurations as “bottle” (long dash), “flat” (short dash), and “focus” (dash-dot), respectively. The mirror coil

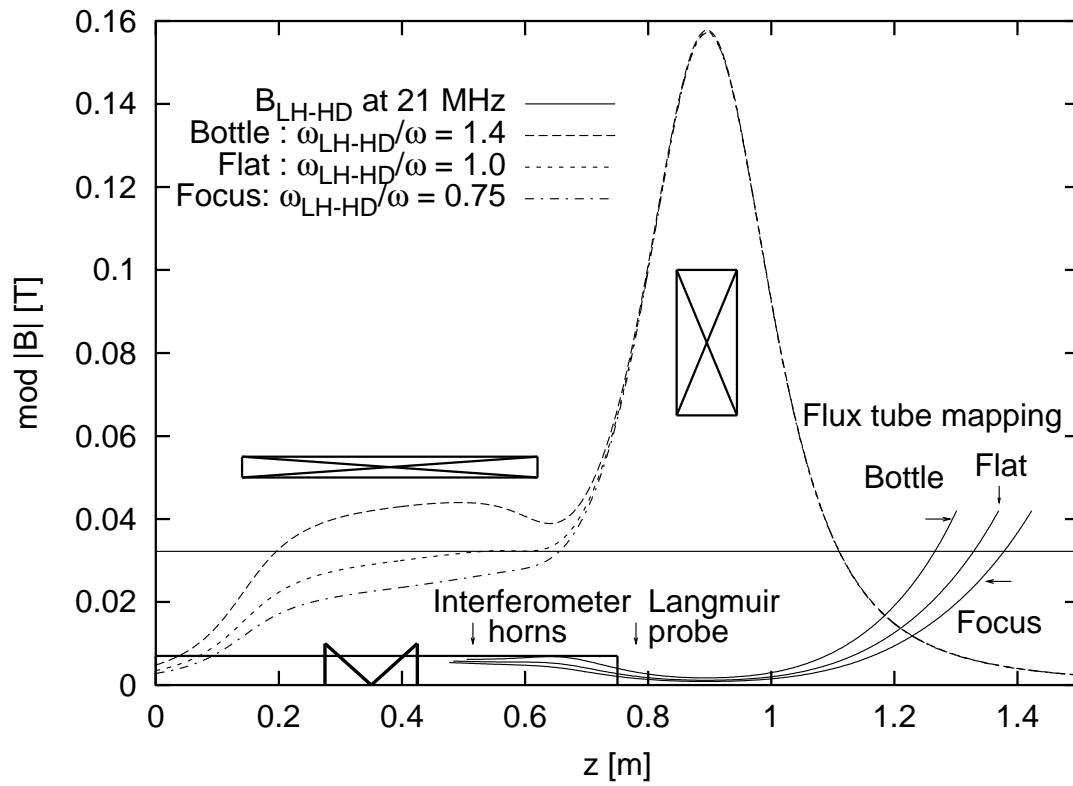


Figure 5.4: Magnetic field configuration for “bottle” (long dash), “flat” (short dash), and “focus” (dash-dot). The identification of them is defined as its shape behavior around $z = 0.6$ m. The mirror coil current is the same value in the figure. Flux tube mappings are also shown in the quartz tube.

current is the same for each of the three configurations. Each of the configurations is also labeled in Figure 5.4 with the ratio of ω_{LH-HD}/ω at $z = 0.6$ m (near the axial peak in the density profile): 1.4 for the “bottle,” 1.0 for the “flat,” and 0.75 for the “focus.” Also shown is the flux tube mapping inside the quartz tube for each configuration. The names for these configurations are obtained from their shape around $z = 0.6$ m. The bottle geometry has a neck such that field lines intersect the quartz tube in the downstream end. For the flat geometry, the field strength is nearly uniform, and the field lines are well aligned with the quartz tube in the primary region where plasma is generated between $z = 0.4$ and $z = 0.6$ m. The focus geometry has good curvature throughout the system, and field lines flare to provide no intersection with the quartz tube downstream.

To isolate the magnetic field strength effects without changing the geometry, the ratio of coil currents was fixed for each of the geometries while the magnetic field strength was varied with constant flux shape. The gas pressure for these experiments was tuned from 3 to 6 mTorr to obtain the maximum density with $\omega_{LH-HD}/\omega \geq 1$, the region generally yields a capability of high-density plasma sustainment rather than other field strength, and input powers of over 3 kW with 21-MHz operation.

Figures 5.5(a), (b), and (c) show the magnetic field dependence on the line-averaged electron density in the left column, and the net power applied in the right column. In the left column, open circles were obtained from the interferometer measurements, and closed circles were obtained from the ion saturation current of the Langmuir probe. The power data is the net power obtained from directional couplers. Horizontally, the results are for the different flux tube mappings, (a) bottle, (b) flat and, (c) focus, respectively. Interferometer measurements were not available during the experiments using the focus geometry. For comparison with the earlier low-power results, one result shown in Figure 5.3 that had the same magnetic field profile (focus) is plotted at $\omega_{LH-HD}/\omega \approx 1.55$ as a solid triangle in Figure 5.5(c). During each scan, the power setting of the signal generator that drives the transmission amplifier was kept constant to give the net power values shown in the right column of Figure 5.5.

Low-frequency oscillations were detected on the interferometer signals during the experiments described above. Fluctuations were observed in the bottle configuration over a narrow range of magnetic fields near ratios with $\omega_{LH-HD}/\omega \approx 0.45$. Fluctua-

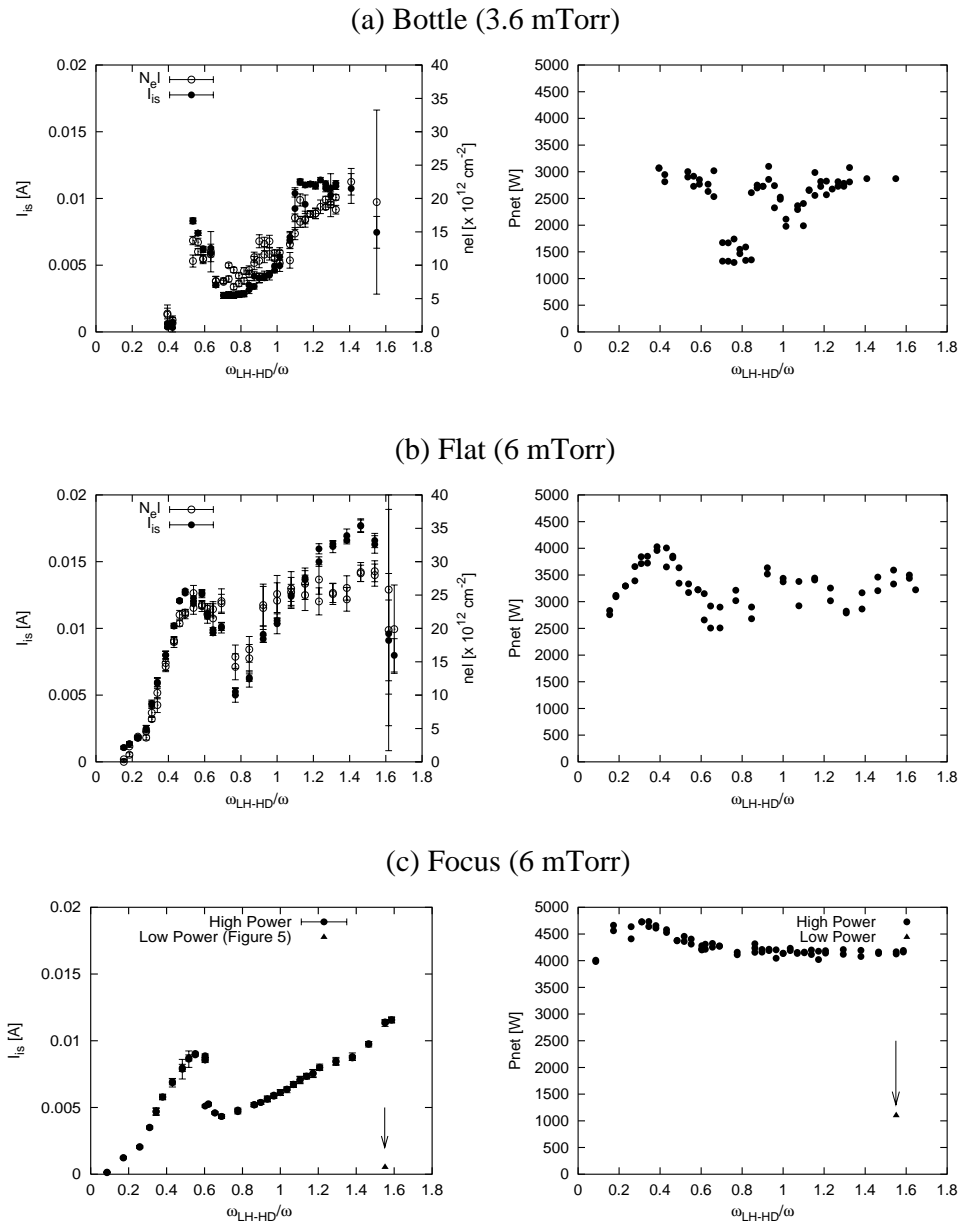


Figure 5.5: Interferometer (open circles on left column figures), Langmuir probe (closed circles on left), and net power (right) measurements scanning the static magnetic field for (a) “bottle,” (b) “flat,” and (c) “focus.” The closed triangle on (c) indicates the result of Figure 5.3 for the same magnetic field profile.

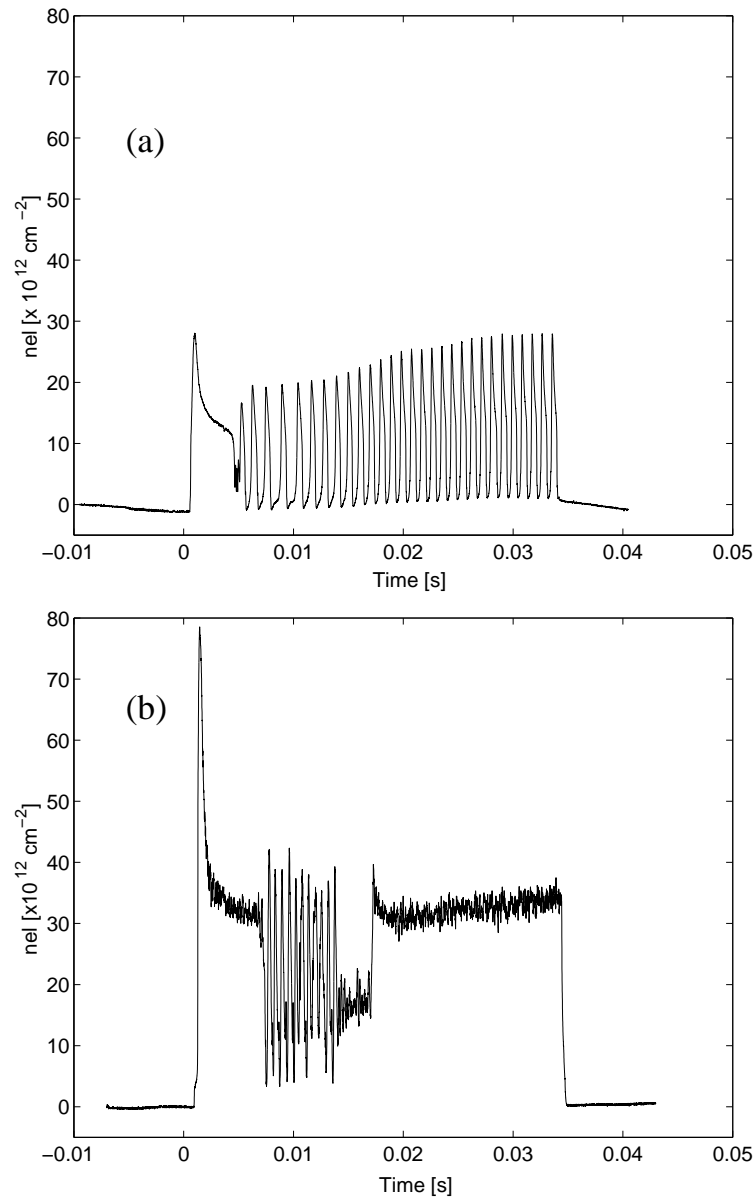


Figure 5.6: Plasma density fluctuations observed on the interferometer signals for scanning B_0 measurements: (a) low - high-density transition (0.8 kHz) from 0.005 to 0.034 sec for $\omega_{LH-HD}/\omega \approx 0.45$ region for bottle configuration, (b) Low-frequency fluctuation (1.6 kHz) from 0.007 to 0.014 sec for $\omega_{LH-HD}/\omega \approx 1.6$ region for flat configuration.

tions also occurred for $\omega_{LH-HD}/\omega \approx 1.6$ in both the bottle and flat geometries. An example of the fluctuations for the bottle configuration with $\omega_{LH-HD}/\omega \approx 0.45$ is shown in Figure 5.6(a). Figure 5.6(b) shows an example of the fluctuations in the flat geometry for $\omega_{LH-HD}/\omega \approx 1.6$.

The observed interferometer line-integrated density fluctuations could be the result of either density or plasma radius variations. While the plasma radius could, in principle, vary with applied magnetic field strength, the plasma radius at the interferometer location was estimated by extrapolation from the density profile measured at $z = 0.78$ m along the magnetic flux tubes. The estimated plasma radius for all conditions was found to be comparable to the radius of the quartz tube. Therefore, the interferometer fluctuations are assumed to represent variation in density.

For the bottle case, operation was sensitive to the RF tuning conditions; however, this sensitivity may have been caused by the lower neutral gas pressure used for this geometry to obtain the best density results. The net power also depended strongly on the magnetic field strength. Oscillations with frequency 0.8 kHz, shown in Figure 5.6(a), were observed near the jump in density for $\omega_{LH-HD}/\omega \approx 0.45$ on the interferometer horn signals. A fluctuation of ~ 9 kHz was also observed on the interferometer signals at $\omega_{LH-HD}/\omega = 0.4$ where only low-density plasma was obtained. Fluctuations were also responsible for the lack of signals in Figure 5.5(a) between $\omega_{LH-HD}/\omega \approx 0.45$ and 0.5 because of instability in the discharge during the transition from low to high density. The density decreased until $\omega_{LH-HD}/\omega = 0.7$ where high-power reflection, approaching half the transmitter power setting, occurred. (Such high reflection was not observed for either flat or focus operation.) For $\omega_{LH-HD}/\omega > 0.7$ in the bottle geometry, the density began increasing roughly proportional to the magnetic field, although a small jump in density was observed by the interferometer when $\omega_{LH-HD}/\omega = 1.1$. Low-frequency fluctuations around 3.1 kHz began to occur for $\omega_{LH-HD}/\omega > 1.4$, and high-density plasmas could not be consistently sustained for every shot for $\omega_{LH-HD}/\omega > 1.4$.

For the flat configuration, operation was not very sensitive to the RF tuning conditions. The density increased monotonically from $\omega_{LH-HD}/\omega = 0.2$ to 0.5, however, for $0.5 < \omega_{LH-HD}/\omega < 0.8$, the density decreased. For $0.8 < \omega_{LH-HD}/\omega \approx 1.5$, the density again increased with increasing magnetic field, reaching the highest values for any of the geometries considered. The maximum net power was cou-

pled for $\omega_{LH-HD}/\omega = 0.4$; however, the density was not maximal at those conditions. Assuming a parabolic-like radial density shape, a peak density of $1.1 \times 10^{19} \text{ m}^{-3}$ was obtained for $\omega_{LH-HD}/\omega \approx 1.0$ from the interferometer signal. At around $\omega_{LH-HD}/\omega = 1.6$, low-frequency fluctuations 1.6 kHz, as shown in Figure 5.6(b), were observed. This fluctuation was probably related to a helicon-mode transition because a small density jump allowed stable high-density discharges for some shots.

The oscillation shown in Figure 5.6(a) is explained as neutral gas depletion by Degeling et al. [89]. The reason it was detected on the bottle case as shown in Figure 5.6(a) is because of the lower fill pressure used compared to the flat case. Although the magnetic field strength is different, case (b) can be explained by a similar mechanism.

As shown in Figure 5.5(c), Langmuir probe signals for the focus geometry were similar to those in the flat geometry case except that the density obtained was consistently lower even though the coupled power was consistently higher. This indicates that the power balance is sensitive to the magnetic field geometry. Net power measurements showed relatively stable operation compared with the other geometries over the full range of the magnetic field scan. For the focus case, the helicon plasma could not be sustained for $\omega_{LH-HD}/\omega > 1.4$, but operation with over 4 kW of RF power provided stable plasmas for ω_{LH-HD}/ω well above 1. This result shows that nonuniform geometries with sufficient power can provide stable high-density helicon plasmas for magnetic fields well above the maximum obtained near $\omega_{LH-HD}/\omega = 1$ as shown in other experiments [86]. This fact is made clear by overlaying one density result from the earlier experiments using lower power (up to 2 kW), shown in Figure 5.3, as a black triangle on Figure 5.5(c). This lower-power result, with a ratio of $\omega_{LH-HD}/\omega \approx 1.4$, had exactly the same focus geometry as the higher-power (over 4 kW) case, but the higher power produced more than ten times the plasma density obtained at lower power. Also, note that for power levels less than 2 kW, the high-density helicon regime could only be obtained over a very narrow range of fields near $\omega_{LH-HD}/\omega \approx 1$; but, with over 4 kW of net power, a high-density plasma could be obtained over the entire range of the static magnetic field scan. The observation that high-density helicon plasmas can be obtained throughout the region with sufficient power is consistent with the power threshold model suggested by Carter et al. [68] when no fluctuations are present. However, significantly more

work is required concerning the radial and axial transport in the power balance [68] to provide an accurate modeling of these discharges over the range of parameters studied.

Another comparison can be made between the different geometries by considering the difference between the interferometer located at $z = 0.5$ m and Langmuir probe signals obtained at $z = 0.78$ m. As shown in Figures 5.5(a) and (b), differences between the two signals are probably caused by changes in the axial density profile with changing magnetic field strength. Strong axial variation has also been reported for systems with a uniform axial magnetic field [90]. Radial profiles were not taken for this data, but we expect that the radial profiles vary considerably with different magnetic field strengths and geometries.

Overall, these geometry experiments show that a nonuniformity in the magnetic field combined with high power levels allow high-density helicon plasmas to be produced over a broad range of magnetic field strengths. Over much of this range, especially $\omega_{LH-HD}/\omega > 1$, the density still increases with increased field strength. Similar results are reported [26, 79, 85, 86] for heavier ions. However, these results are markedly different from the hydrogen operation in uniform fields reported by Sakawa et al. [85] and Light et al. [86]. Also, from the net power measurements, the flat geometry was the optimum magnetic flux tube mapping, producing the highest plasma densities, even though it typically required less power than the focus geometry. However, the focus geometry provided the most stable operation over the range of magnetic fields that were scanned.

5.4 Isolating magnetic field strength dependencies

In this section, we consider the role of the static magnetic field strength in the axial region of plasma production for these discharges. To understand the importance of this parameter in high-density helicon plasmas, we isolated three cases to make detailed studies of the RF mode structure. All cases have good curvature in similar "focus-like" magnetic geometries. The parameters for the cases are summarized as follows:

Case I is referred to as a "choke" because field lines in this geometry are somewhat

more focused than in the other two cases. Its configuration is very similar to the case illustrated in Figure 5.2 for $I_{SOL} = 0$ A. This case has the lowest magnetic field in the antenna region of the three, with $\omega_{LH-HD}/\omega = 0.43$. Stable plasmas could be obtained for these conditions for power > 3 kW, but RF field measurements are presented here at the 1.8-kW power level to offer contrast with the other cases as explained in Section 5.4.2. Density values of $n_e \approx 1.8 \times 10^{18} \text{ m}^{-3}$ are obtained for this case using 1.8 kW and a fill pressure of 13 mTorr. Electron density was lower than for the other cases described below because of magnetic field strength and geometry differences rather than higher gas pressure.

Case II uses the focus geometry described in Section 5.3.2 with $\omega_{LH-HD}/\omega = 0.55$, as shown in Figure 5.5(c). A power level of 3.1 kW was used with a fill pressure of 8.6 mTorr, and density values of $n_e \approx 1.1 \times 10^{19} \text{ m}^{-3}$ are obtained in this case.

Case III uses the same focus geometry used in Case II, but with $\omega_{LH-HD}/\omega = 1.1$ as shown in Figure 5.5(c). The power and fill pressure are also nearly identical with those of Case II, being 3.2 kW and 8.6 mTorr, respectively. The density value obtained for Case III is $n_e = 1.2 \times 10^{19} \text{ m}^{-3}$, so only the magnetic field strength in the plasma formation region is significantly different from Case II.

In Section 5.4.1, we present measurements of the RF magnetic field for these three cases. In Section 5.4.2, we analyze the signals to show that at least two radial modes can appear in the Mini-RFTF device during high-density helicon operation.

5.4.1 Radial and axial mapping of the RF magnetic field

Figure 5.7 shows the axial profile of B_z/I_{rf} for (a) amplitude and (b) phase shift, respectively, for all three cases. The RF magnetic probe was rotated to be 1 cm off the axis of the device. Phase signals were adjust to 0 degrees at the downstream antenna ring located at $z = 0.43$ m.

From Figure 5.7(a), for Case I (choke), the amplitude monotonically damps along the axis beyond the antenna near-field region (the downstream antenna ring is located at $z = 0.43$ m). In contrast, for Cases II (open circles) and III (closed triangles), beating structures were observed in the wave amplitude and phase. Case II, with a lower magnetic field strength than Case III, shows a much stronger beating effect than Case III. One possible explanation of this beating structure is the excitation of standing waves with wavelengths dominated by the device scale [91].

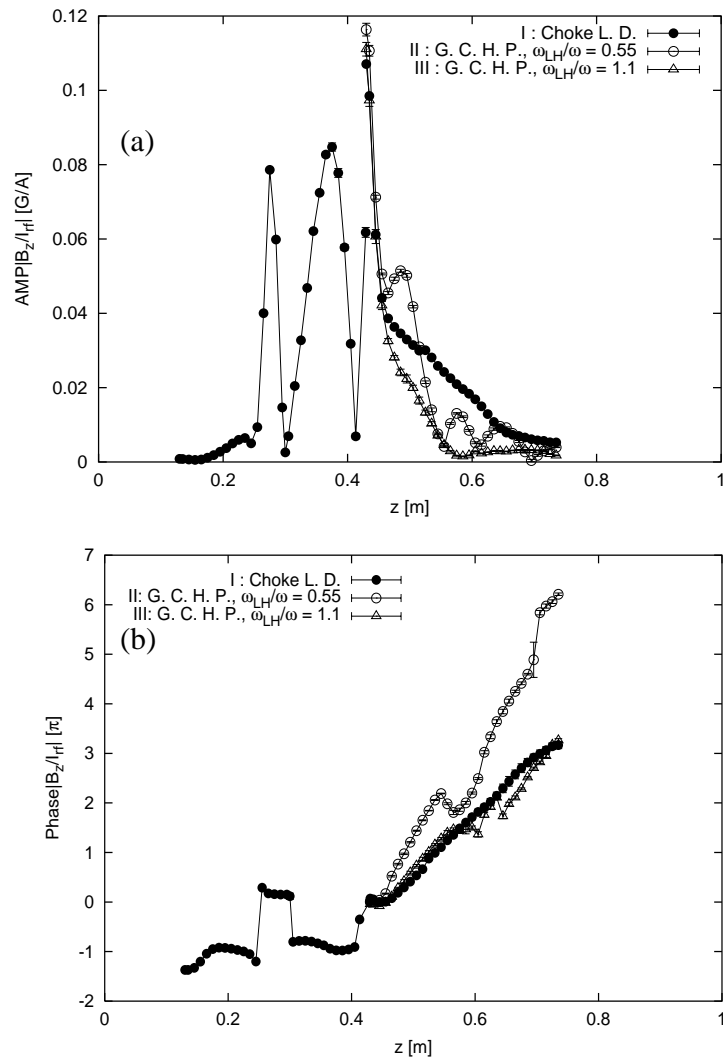


Figure 5.7: The axial profile of B_z/I_{rf} for (a) amplitude and (b) phase shift for the following conditions: I: Low-power (L. P.) Choke (closed circles) 1.8 kW, $n_e = 1.6 \times 10^{18} \text{ m}^{-3}$. II: Good curvature, high power (G. C. H. P.) $\omega_{LH-HD}/\omega = 0.55$ 3.1 kW, $n_e = 1.1 \times 10^{19} \text{ m}^{-3}$. III: G. C. H. P. $\omega_{LH-HD}/\omega = 1.1$ 3.2 kW, $n_e = 1.2 \times 10^{19} \text{ m}^{-3}$. Phase shifts were adjusted at the antenna ring.

However, in Figure 5.7(b), the phase shift profile for both Cases II and III shows a traveling wave structure, and the measured beat profile is not explained by consideration of only a single axial wave number. This result holds true even if the static field strength and density profile non-uniformities are taken into account.

Figure 5.8 shows radial profiles of the oscillating wave fields (a) amplitude and (b) phase shift at the same location for Case I (closed circles) and II (open circles). The RF magnetic probe was located at $z = 0.52$ m and rotated to obtain the radial profile. The plasma radius was not measured at the location where the radial magnetic field was measured. However, the plasma radius was measured at $z = 0.78$ m and flux tube mapping of the magnetic field was used to estimate the radius of plasma on the point of B_z measurements. Both plasma radii are close to that of quartz tube. It should be noted that these are not purely radial scans because the the RF magnetic probe angular location was not fixed. However, that is an acceptable way to estimate radial profile of the magnetic fields. A similar method was addressed by Krämer et al. [92].

As shown in Figure 5.8(b), there were phase jumps on the axis. The $m = +1$ modes are expected to be dominant there because $m = -1$ has been reported to be weakly excited [93]. Figure 5.8(a) shows that the wave field is more focused near the center of the device for Case II than for Case I. The radial wave focusing effect was observed in the near-field region of the antenna for Case II. Thus, the strong beating phenomena indicates that more than two axial wavelengths were excited in the plasma. If it is assumed that two modes, the fundamental radial and second higher radial mode, are excited in the plasma, then a peaked profile for the radial wave fields is expected as discussed in Section 5.4.2.

5.4.2 Radial mode analysis

In this section, we explain the wave profiles measured in Section 5.4.1 by considering the propagation and damping of two traveling waves. Theoretical treatments for a radial mode analysis addressed here are described in Section 2.3.

Figure 5.9 shows a comparison of Equation (2.5) to experimental amplitude in (a) and phase in (b) for selected ratios of the first two eigenmodes, a_2 , for each of the three cases. Solid lines correspond to the fit for Case I (choke), dashed lines to Case II, and dash-dotted lines to the Case III. The phase shift defined by the

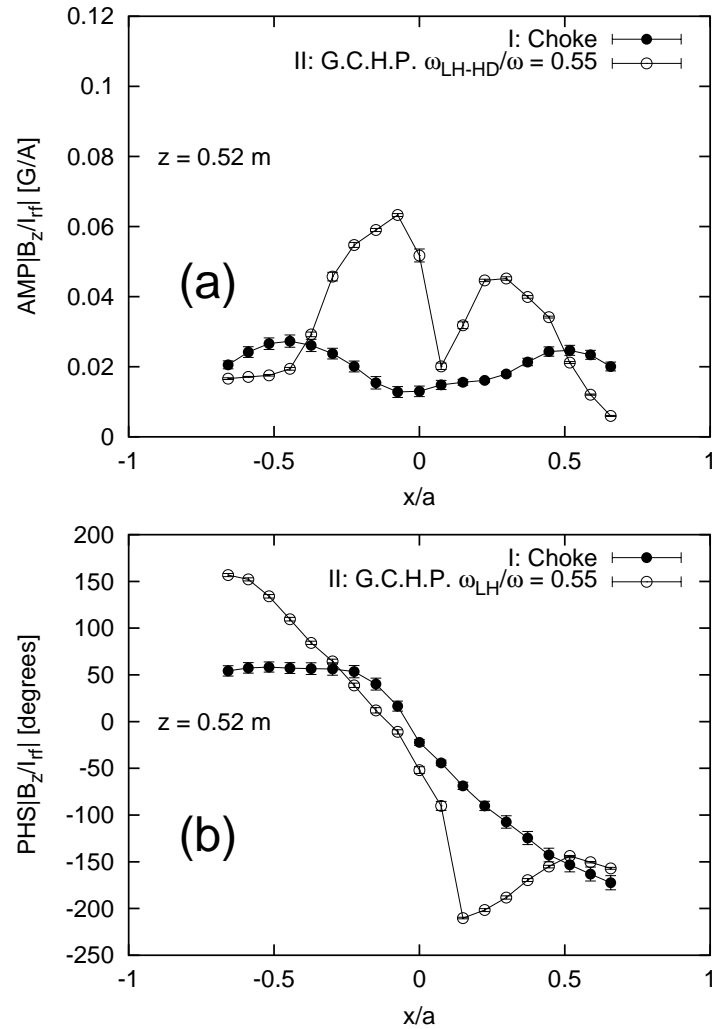


Figure 5.8: Radial (a) amplitude and (b) phase shift of an oscillating wave field measured at $z = 0.52$ m. For Case I (choke) the power level was 1.8 kW. For Case II (good curvature) a power level of 3.2 kW with $\omega_{LH-HD}/\omega = 0.55$ was used. The radial position was normalized by the radius of the quartz tube.

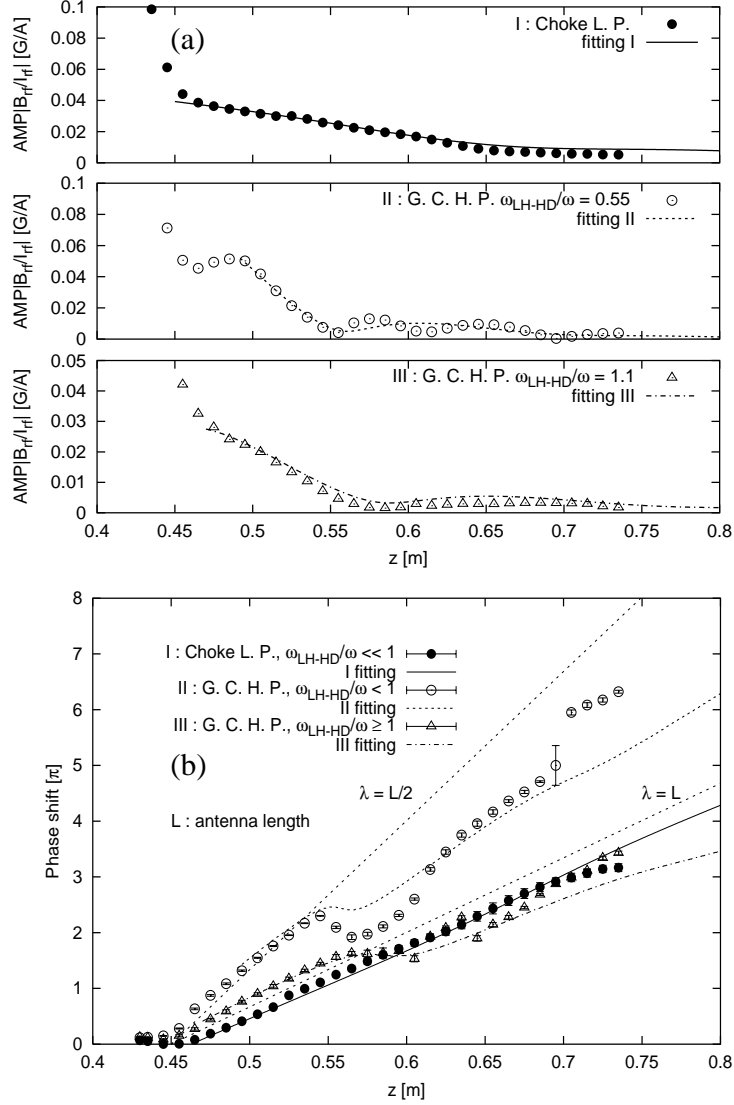


Figure 5.9: Fitting curve of B_{rf}/I_{rf} for (a) amplitude and (b) phase shift. Coefficients are as follows: I: $a_2=0.10$, $k_{z1}^r = 40 \text{ m}^{-1}$ and $d = 0.13$. II: $a_2=0.55$, $k_{z1}^r = 92 \text{ m}^{-1}$ and $d = 0.19$. III: $a_2=0.50$, $k_{z1}^r = 60 \text{ m}^{-1}$ and $d = 0.20$.

antenna length and half of the antenna length are also shown in Figure 5.9(b). Here we assumed that $k_{z2}^r/k_{z1}^r = \alpha_1/\alpha_2 = 0.47$, which was computed from a parabolic density profile ($[1 - (r/a)^2]^4$) helicon dispersion relation, as shown in Figure 2.3. For a collisional plasma, the wave damping ratio is mainly proportional to the plasma density, and assuming the wave damping ratio, d , is the same for both the first and second axial traveling waves: $d = k_{z1}^i/k_{z1}^r = k_{z2}^i/k_{z2}^r$. Other parameters (k_{z1} and a_2) were found in order to satisfy both wave amplitude beating and phase shift as well as d .

As shown in Figure 5.9, the fit based on Equation (2.5) agrees well with the experimental data for Case I, showing that the first radial mode was dominant for this case with lower power operation. For Cases II and III, the second radial mode contribution must be comparable with the first radial mode to obtain good fits using Equation (2.5). For Case III, the measured axial wavelength was consistent with the antenna length rather than twice the antenna length. However, for Case II, the measured axial wavelength was even shorter than the antenna length. Moreover, the measured phase shift indicates the existence of an even shorter wavelength near $z = 0.55$ to 0.65 m. The cause of the phase jump occurring near $z = 0.7$ m is not clear, but if we assumed that a wavelength shorter than $L/2$, was excited near the $z = 0.55$ m region, then the phase jump can be explained with this model. Note also that the damping ratio for Case II and III was larger than that of Case I, which is qualitatively expected because Case II and III have higher density (10^{19} m^{-3}) than Case I (10^{18} m^{-3}).

From Figure 5.8, the measured radial B_z/I_{rf} profile for Case II is focused on the axis and is comparable to the B_z structure obtained by combining the first and second radial modes shown in Figure 2.4. This result indicates the possibility that the first and second radial modes are mixing, which is consistent with the beating structure detected along the axis, as shown in Figure 5.9.

As for a higher radial mode coupling with the first radial eigenmode for $m = 1$, a combination with other azimuthal modes is also a possibility for the strong beating effect [50] shown in Figure 5.9. However, the second radial mode seems to play a more important role in our experiments. As described in Section 2.3, the helicon dispersion relation with a radially nonuniform density profile gives an axial wavelength identification for each azimuthal mode; the wavelength of $m = +1$ is

shorter than $m = 0$ and $m = -1$ [50, 51]. For the B_z radial profile, a mixture of the first radial for $m = -1$ and first radial for $m = +1$ modes has a structure similar to that obtained by mixing the first and second radial for $m = +1$ modes for the same amplitude contribution of each mode. Though $m = 0$ also has a shorter wavelength, from the Fourier transformation, its amplitude is negligible, and a wave structure made from the combination $m = 0$ and $m = +1$ also has a strong asymmetry along the radius that does not agree with the results shown in Figure 2.4. For $m = \pm 3$ modes from the double half turn (DHT) part of the antenna, these have smaller contributions than the $m = \pm 1$.

To interpret the beating structure from Figure 5.7(a), we required a much shorter axial wavelength than is obtained from the first radial mode for $m = -1$. The wavelength of the second radial mode for $m = +1$ is shorter than that of the first radial mode for $m = -1$, strengthening the argument that the second radial mode plays a strong role in our experiment. Furthermore, the $m = +1$ mode is largely responsible for high-density helicon plasmas, and the $m = -1$ mode is reported to be strongly reduced along the z direction [93]. Thus, even though the effects of multiple azimuthal modes may help in fitting the experimental beating structure by introducing many axial wavelengths, the evidence strongly suggests that the second radial mode for $m = +1$ was the dominant mechanism responsible for the beating that was observed. Numerical simulations done with controlled azimuthal modes would answer the question.

Figure 5.10 shows the radial mode number profile estimated from Figure 5.5 (b) for the flat case normalized by the first radial mode α_{1st} . The maximum electron density was computed from the line density measurements shown in Figure 5.5 (b). Here, α_{1st} was computed value for the density profile factor $q = 4$ in Figure 2.3. Axial wavelengths were assumed to be L and $L/2$ as represented by opened and closed circles, respectively to calculate α_0 in Equation (2.3).

From Figure 5.10, for the $\omega_{LH-HD}/\omega \geq 1$ region, the dispersion relation was satisfied by the first radial eigenmode, and, as shown in Figure 5.9, the measured wavelength was also close to the antenna length. For $\omega_{LH-HD}/\omega \simeq 0.5$, the measured phase shift shown in Figure 5.9 indicates an axial wavelength about half the antenna length in addition to a wavelength contributed by the second radial mode that is close to the antenna length.

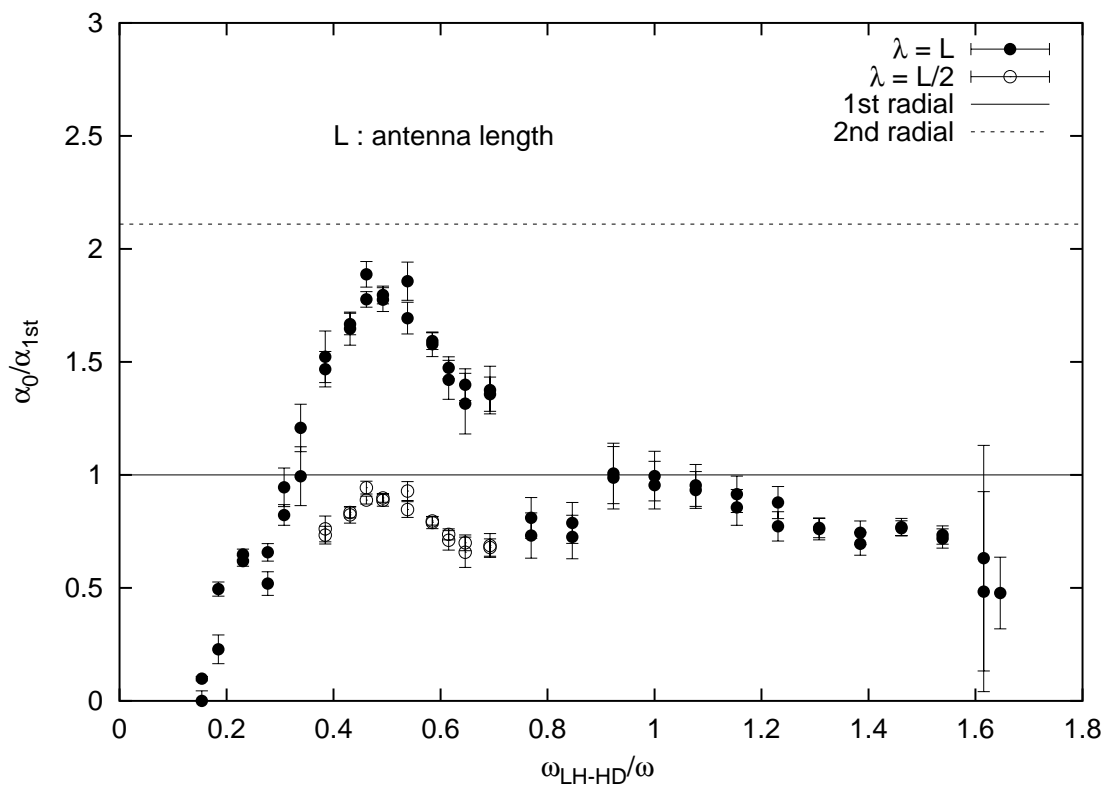


Figure 5.10: Normalized radial mode number profile estimated from the flat configuration. The axial wavelength was assumed to be L (closed circle) and $L/2$ (open circle).

To explain these beating phenomena in detail, as well as the damping mechanism, the axial nonuniformity and global wave phenomena should be considered. Such a calculation is beyond the scope of the work presented here, but some effects can be inferred from the simple estimates. In our system, the static magnetic field is increasing along the axis. This geometrical factor chokes the flux tube and helps to focus the plasma. An axial neutral pressure profile exists in the quartz tube, so the pressure profile might depend on the magnetic field strength as well as the axial density profile. According to the other experiments, the density peak observed for lower magnetic field operation (beating wave structure) is seen to be related to the field strength, but not to input power nor fill pressure. For higher-power operation, the second radial mode amplitude factor, a_2 , becomes comparable to that of the first radial mode. Our helical antenna was designed predominantly to excite wavelengths of $2L$, where L is the antenna length; however, the measured wavelength is shorter and comparable to L . Similar results were obtained by several authors [63, 92].

5.5 Discussion

Stable, high-density hydrogen plasmas have been obtained and studied in the axially nonuniform magnetic field Mini-RFTF device. The nonuniform magnetic field allows the plasma to be sustained over a broad range of parameters. Peak densities of $\simeq 10^{19} \text{ m}^{-3}$ were achieved for frequencies both below and above the high-density limit of the lower hybrid frequency throughout the plasma production region. Systematic measurements of different magnetic geometries and field strengths allowed the best operating regimes to be identified. Operation at a high magnetic field strength required a higher power threshold to be overcome to achieve the helicon mode than was observed for low magnetic field strength operation, but once achieved, high-field-strength operation proved to be higher density than operation near the lower hybrid resonance. Measurements of the axial component of the RF magnetic field show a beating of two axially propagating helicon modes as well as a radial wave focusing effect. Higher-order radial modes, rather than multiple azimuthal mode coupling [50], seem to be important for high-density operation.

High-density hydrogen plasma operation was investigated by changing the magnetic field configuration in the antenna region (Section 5.3.1) and by changing the

nonuniform flux tube mapping (Section 5.3.2). For both experiments, as shown in Figures 5.3(a) and 5.5, it was found that high-density hydrogen operation was sustained for $B_0 < B_{LH-HD}$ and $B_0 \approx B_{LH-HD}$ at modest power levels. The axial nonuniformity in magnetic field geometry, the overall magnetic field strength, and the RF power available are all found to be important parameters in helicon operation. The most efficient operation was for geometries that minimize field line interactions with the surface of the quartz tube (flat). The high axial nonuniformity allowed hydrogen helicon plasmas to be well sustained with very low magnetic fields in the antenna region, as shown in Figure 5.3(a) with relatively lower power (< 2 kW).

If enough power was used (> 3 kW), helicon operation was also possible for $B_0 > B_{LH-HD}$ as shown in Figure 5.5. In fact, the best operation was for magnetic fields above the high-density limit of lower hybrid, but this high-field operation could be achieved only by overcoming a higher power threshold than is required for lower field operation. The observed maximum density appeared in the downstream region ($z > 0.4$ m) and was more than five times higher than that reported by other authors for similar fields, except for a recent report [28, 31, 88], and high-density did not seem to limit the operation in any way. Because of the nonuniform field, the upstream region with $z < 0.3$ m, does have field strength values near B_{LH-HD} , which may help to generate low-density plasma that will eventually support the helicon plasma downstream where $B_0 > B_{LH-HD}$.

As a result of oscillating magnetic field measurements and analysis shown in Figure 5.9, for cases with $B_0 < B_{LH-HD}$, high-density (10^{19} m⁻³) helicon plasma seems to be supported by a combination of both the second and fundamental radial eigenmodes rather than a coupling of multiple azimuthal modes [50]. In that case, the helical antenna excited wavelengths close to the antenna length, L , for the second radial, and close to $L/2$ for the fundamental radial mode. The contribution of the second radial mode may be caused by a wave-focusing effect that sustains plasma near the axis, as shown in Figure 5.8. On the other hand, for the low-density case shown in Figure 5.9 (choke), only the fundamental radial eigenmode with wavelength $\approx L$ was observed.

The nonuniform magnetic field contributes to a wide operation range in Mini-RFTF, especially for lower magnetic fields. Good curvature configurations (both

flat and focus) show more stable plasma operation as ω_{LH-HD}/ω is varied than in the bottle case shown in Figure 5.5. This observation may indicate that the converging nonuniform field allows easier access for the helicon wave than is found in uniform systems. For systems with uniform magnetic field and electrons that are strongly magnetized, slow radial diffusion across field lines can make radial peaking of the density profile difficult. For the nonuniform field configurations with a converging magnetic field downstream, electrons can move across field lines in regions of low magnetic field, and then along field lines toward the axis to peak the radial density profile. Thus, while the detailed coupling to a particular helicon configuration depends on stability, transport, the local power balance, and the wave dispersion, our findings generally suggest that systems with nonuniform magnetic fields may allow easier coupling to higher-order radial eigenmodes than is possible in straight-line systems. Our future research will perform careful measurements with $\omega_{LH-HD}/\omega \approx 0.5, 1$ and 1.5 by changing the power levels to better reveal the mechanisms for coupling to high-order radial modes.

For high magnetic field operation with $\omega_{LH-HD}/\omega = 1.5$, we found that achieving high densities of around 10^{19} m^{-3} was possible if enough power was coupled to the plasma. Several studies on systems with uniform magnetic fields have shown that the plasma density can be limited by instabilities [86, 94] to $< 10^{18} \text{ m}^{-3}$. However, these instabilities were not evident in the high-field nonuniform configurations in Mini-RFTF. Some large amplitude fluctuations were observed, as shown in Figure 5.6. However, these fluctuations appear to be related to the transition from low- to high-density conditions as well as neutral depletion [89]. Our results show that it is possible to obtain hydrogen plasma densities of $\approx 10^{19} \text{ m}^{-3}$ using both high power and high magnetic fields in optimized nonuniformity magnetic field configurations. Additional research into the high-field, high-density hydrogen operation in Mini-RFTF is planned.

Chapter 6

Non-uniform magnetic field contribution to density enhancement of light ion helicon plasma sources

6.1 Introduction

Helicon plasma discharges generated by radio-frequency waves are of great interest due to their high ionization efficiency. Pioneering works in helicon discharges dates to the 1960s [19, 20]. The physics of helicon discharges has been reviewed by Chen and Boswell [22, 23], and applications have been found in many areas, including fusion research [26–28], space plasma simulation [29], and plasma thrusters [12].

The influence of axially non-uniform magnetic field geometries on helicon plasma source performance has been investigated experimentally by several groups [69, 75, 95–97]. Chen first reported that a cusp field geometry results in a density enhancement in comparison to uniform geometry [69, 95], which was attributed to the reflection of helicon waves launched in the upstream direction [70]. Gilland et al. suggested the possibility of improved collisional confinement resulting from absorption of the upstream helicon wave [96]. Guo et al. examined the contribution of the varying magnetic field strength to produce strong density gradients. The nonuniformity in $|B|$ was believed to increase wave absorption and source efficiency due to the wide range of phase velocities produced, leading to increased production of hot electrons.

However, in these experiments reported there, only a limited number of field geometries were examined, and no comprehensive investigation of field geometry effects was conducted. Achievement of high densities ($> 10^{19} \text{ m}^{-3}$), while at the same time minimizing neutral densities, in a non-uniform magnetic field configuration is especially important for fusion and space propulsion applications [12], where charge exchange losses can critically affect performance.

In this chapter, the dependence of plasma density on a wide range of magnetic field profiles, fill gas pressures, and input powers are extensively investigated for operation with both hydrogen and helium. Density enhancement at low $|B|$ has been found to occur only for the case of monotonically increasing field strength in the upstream axial direction (denoted here as the ‘focus’ geometry), and is believed to result from enhanced power deposition in the source region.

A description of the experimental setup and the various external magnetic field profiles employed is presented in Section 6.2. The dependence of plasma density on $|B|$ for fixed axial magnetic field strength profiles is discussed in Section 6.3. Effects of varying the axial $|B|$ profile is discussed in Section 6.4, followed by a discussion and final conclusions in Sections 6.5 and 6.6, respectively.

6.2 Experimental apparatus and geometry of the external magnetic

The experimental apparatus used in all of the experiments reported here is shown in Chapter 3, Figure 3.1. All of the experiments reported here took place at a frequency of 21 MHz. Forward and reflected power are monitored by directional couplers mounted between the power supply and the matching network. Diagnostics include the 70-GHz interferometer that can be scanned axially ($z = 0.1$ to 0.7 m), and the radially movable RF-compensated Langmuir probes. The probe installed at the end of quartz tube ($z = 0.78$ m) is referred to here as the upstream probe, while the probe installed at the center of the viewing port ($z = 1.22$ m) is referred to as the downstream probe. The current-voltage sensor pair mounted between the matching network and the antenna is used in conjunction with the Hewlett-Packard 8753D network analyzer to measure net input power, as well as vacuum and plasma loading. During typical operation, the plasma is pulsed for 40 ms with duty cycle of

2%. The matching is tuned to keep the reflected power less than 5% of the forward power during the high density phase of the pulse.

Figure 6.1 shows the various profiles of $|B|$ on axis (a), and flux-tube mappings (b), (c) and (d) used in these experiments. The figure also shows the locations of the helical antenna, magnetic field coils, and Langmuir probes. Two parameters are used here to define the magnetic field geometry. The first is the ratio of the maximum value of $|B|$ (located at the middle place of MR1), to the value at the middle place of the SOL coil, defined here as M. R. (Magnetic field strength Ratio). The second is the ratio ω_{LH-HD}/ω of the high density limit of the lower hybrid frequency ($= \sqrt{\omega_{ce}\omega_{ci}}$), to the RF frequency, where ω is the frequency of the applied RF, and ω_{ce} and ω_{ci} are the electron cyclotron frequency and the ion cyclotron frequency, respectively. For instance, $\omega_{LH-HD}/\omega = 1.0$ implies that the external axial field strength at the center of the SOL coil is 322 G for hydrogen and 644 G for helium for $f = \omega/2\pi = 21$ MHz.

In Figure 6.1, magnetic field strength profiles on axis and the corresponding magnetic flux tube mappings (surfaces of constant flux perpendicular to the axis) are plotted for several values of M. R. Cases with M. R. < 5 are denoted as “flared”, and the lines of magnetic force intersect the quartz tube at least twice as shown in Figure 6.1 (b) of M. R. = 1.0 case. For the case in which M. R. = 5, there is a flux tube for which the field lines are parallel to the quartz tube inner wall from the antenna location to the downstream end of the tube as shown in the figure (c). Here, M. R. > 5 cases, shown in the figure (d), have the “focus” geometry, which denotes monotonically increasing $|B|$ downstream up to the peak under MR1, and the lines of magnetic force have single intersections with the wall of the quartz tube.

6.3 Dependence of density enhancement on magnetic field strength

In the first set of experiments, the effect of magnetic field strength on the plasma density was investigated for the case in which the magnetic field geometry was kept constant. This was accomplished by operating the device with a fixed value of M. R. = 5.0, so that the magnetic field strength was varied by a nearly constant factor throughout the device. Other parameters that were modified during the

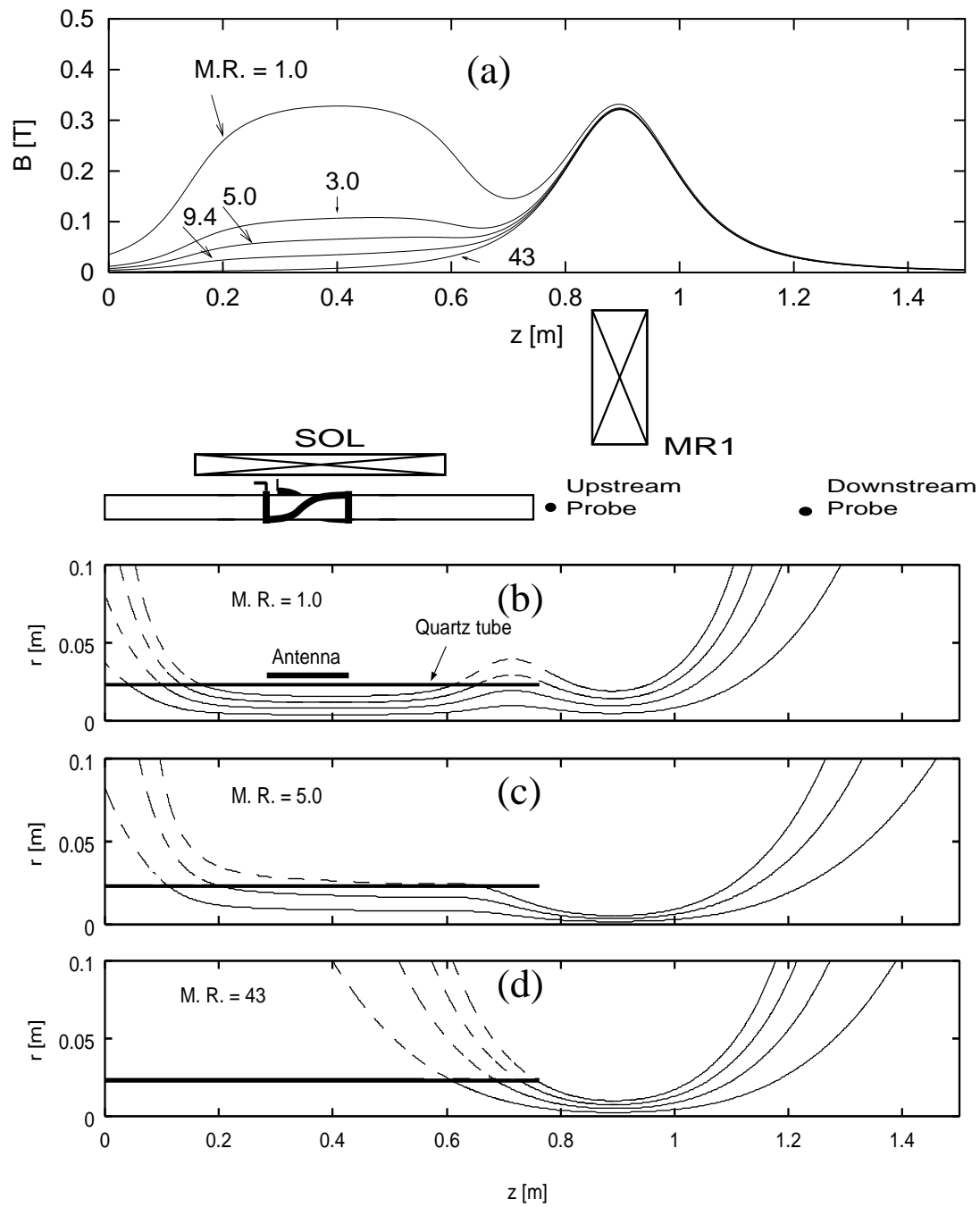


Figure 6.1: Various profiles of $|B|$ on axis (a), and flux-tube mappings (b), (c) and (d), used in these experiments.

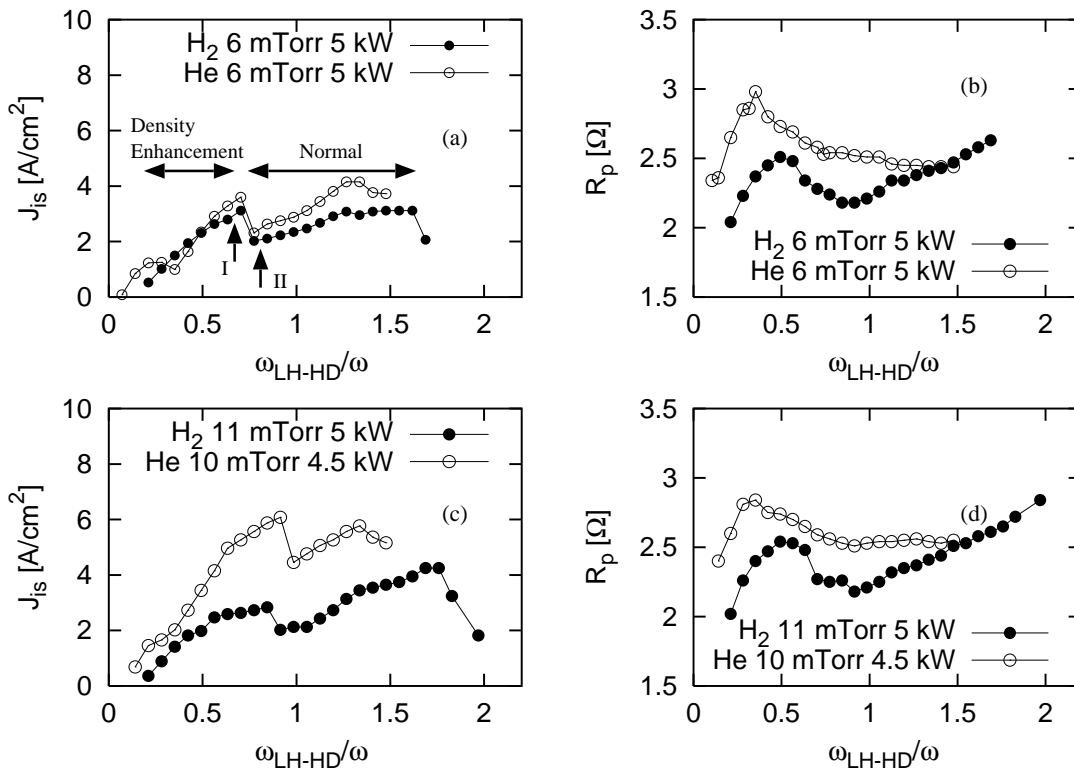


Figure 6.2: Measurements of ion saturation current (J_{is}) and antenna loading (R_p) versus external field strength $|B|$ for normal and high pressures both hydrogen (closed circles) and helium (open circles). Flux tube mapping was fixed as M. R. = 5.0.

course of these experiments were the net injected RF power and the fill gas pressure. Experiments were conducted using both hydrogen and helium.

In Figure 6.2, measurements of ion saturation current (J_{is}) and antenna loading (R_p) versus external field strength $|B|$ are shown for two values of the fill pressure (denoted “normal” and “high” in the figure caption). The data was taken using the upstream Langmuir probe (located at $z = 0.78$ m), which was positioned on-axis. During the magnetic field scan, the matching was adjusted to minimize the reflected power, and the net power was held constant.

As shown in Figures 6.2 (a) and (c), J_{is} initially increases with ω_{LH-HD}/ω ($\propto |B|$) for both hydrogen and helium, at both normal and high fill pressures. Interestingly, this increase with $|B|$ continues up to the same value of ω_{LH-HD}/ω independent of the ion species, beyond which a noticeable drop in J_{is} occurs. However, the value of

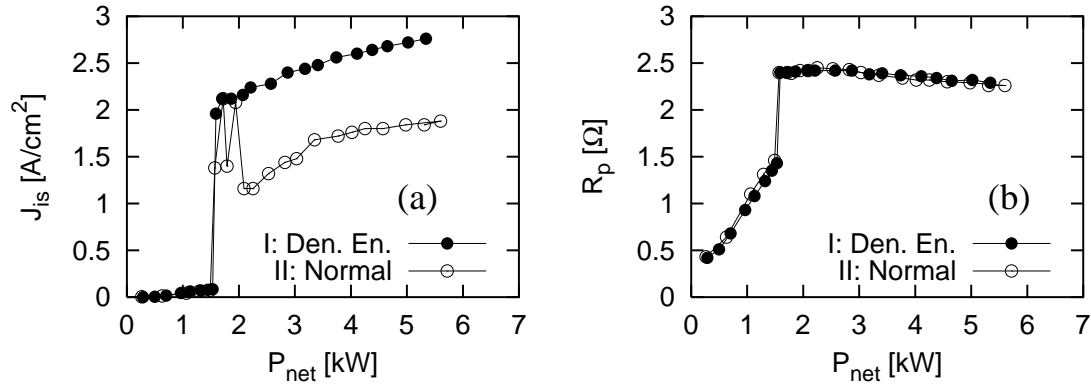


Figure 6.3: Net power dependence of (a) an ion saturation current density and (b) a loading for hydrogen operation at the values of ω_{LH-HD}/ω corresponding to the points labeled I (closed-circles) and II (open circles) in Figure 6.2. Experimental conditions were the same as in Figures 6.2 (a) and (b).

ω_{LH-HD}/ω at which the drop occurs does depend on the fill pressure. For the case of high fill pressure, the increase in J_{is} with $|B|$ persists to a value of $\omega_{LH-HD}/\omega \sim 0.85$, while for the low fill pressure case, the drop occurs at $\omega_{LH-HD}/\omega \sim 0.7$. As shown in the figure, we designate the region before the drop as the “Density Enhanced (Den. En.)” region, and the region of density increase with $|B|$ beyond the drop as the “Normal” region. The antenna loading also initially increases with $|B|$, as shown in Figures 6.2 (b) and (d), but in this case the behavior relative to ω_{LH-HD}/ω , does depend on the ion species, but is nearly independent of the fill pressure, the reverse of the situation observed for the J_{is} dependencies. Also, the sudden drop in J_{is} seems not appear to the values of R_p except for normal case with H_2 . It is not known at the present time why there is a correspondence between plasma density and antenna loading over only limited regions.

Figure 6.3 shows the net power dependence of (a) the ion saturation current and (b) antenna loading for hydrogen operation at the values of ω_{LH-HD}/ω corresponding to the points labeled I and II in Figure 6.2 (a).

The fill pressure (6 mTorr), was the same value as that used to produce Figure 6.2 (a). The closed-circle curve corresponds to the value of ω_{LH-HD}/ω at point I ($=0.70$), which is in the “density enhanced” region, and the open circle curve corresponds to the value at point II ($=0.77$), which is in the “normal” region. For both cases, there is a transition from an “inductive” to “helicon” mode for $P \sim 1.6$ kW. This

is clearly evidenced by a large jump in both J_{is} and R_p . Beyond this point, J_{is} gradually increases with net power for the density enhanced case, but for the higher field (normal) case, there is a somewhat unstable transition which settles into a stable gradual increase at powers above 2 kW, with values substantially lower than those for the lower field (density enhanced) case. The data suggests for both cases that the magnetic field strength has a greater effect on the plasma density than the power level, as long as the power is high enough to produce a helicon mode. An unexpected result is that for the normal case the density tends to jump up to the value seen for the density enhanced case at relatively low power levels, but not higher ones. We do not have an explanation yet for this feature.

Figure 6.4 shows radial profiles of the ion saturation current (a) upstream and (b) downstream for density enhanced ($\omega_{LH-HD}/\omega = 0.63$, closed circles) and normal ($\omega_{LH-HD}/\omega = 0.84$, open circles) hydrogen operation. The net power was 5 kW, and the fill pressure was again 6 mTorr. As shown in the figure, for the normal, higher field case, a peaked radial ion saturation current profile is observed in both the upstream and downstream Langmuir probe locations. In the density enhanced case, the radial profile was again peaked in the upstream region, but was now hollow in the downstream region. The profile in the outer region of the plasma was identical in both cases. For hydrogen operation in particular, the discharge had a bright edge when observed from the viewing port (located downstream) in the density enhanced case. A possible explanation for the observed radial profiles of J_{is} is that most of the power is absorbed in the source region for the density enhanced case, but radial transport results in a hollow downstream profile. For the normal case, some power may propagate near the axis substantially further downstream, creating plasma to replace that lost to radial transport.

Figure 6.5 shows measurements of the relative magnitude and phase of the axial RF magnetic field made during previous experiments [32] for both the density enhanced and normal operation regimes. The measured values are normalized to the magnitude and phase of the antenna current measured at the output of the matching circuit. For the density enhanced case, a strong beating wave structure was detected, which was explained as a superposition of the fundamental and second radial eigenmodes [32]. The former also was found to have an axial wavelength of approximately half the antenna length, and the latter an axial wavelength equal to

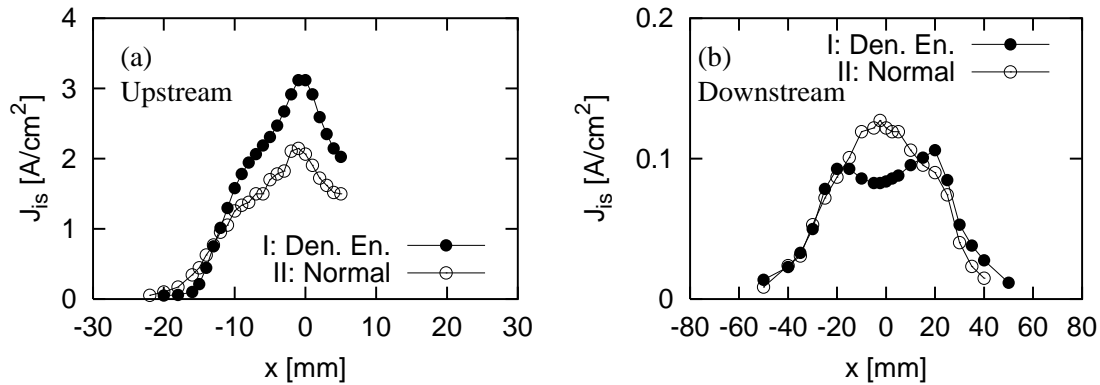


Figure 6.4: Radial profiles of the ion saturation current (a) upstream and (b) downstream for density enhanced ($\omega_{LH-HD}/\omega = 0.63$, closed circles) and normal ($\omega_{LH-HD}/\omega = 0.84$, open circles) hydrogen operation.

the antenna length. In the normal case, only the fundamental mode was observed, with an axial wavelength corresponding to the full antenna length. This is consistent with the notion that in the density enhanced case the power absorption is stronger in the source region, since a higher radial mode would be expected to be more strongly collisionally damped [49]. The normal mode may allow power to be carried further downstream.

6.4 Flux tube mapping dependence of density enhancement

In the previous section, the effects of the magnetic field strength on plasma density for a fixed magnetic geometry were investigated. In this section the dependence of the density on changes in the magnetic geometry are explored.

Figure 6.6 shows graphs of J_{is} versus ω_{LH-HD}/ω similar to those shown in Figures 6.2 (a) and (c), but in this case the fill pressure is held constant, and sweeps are made for values of M. R. between 1 and 43. Again, both graphs were obtained using data from the upstream probe. Figure 6.6 (a) shows results with hydrogen with $P = 5$ kW and fill pressure = 11 mTorr, and 6.6 (b) shows results with helium, $P = 4.5$ kW, and fill pressure = 10 mTorr.

A feature of this data is that the density enhanced mode, with a local minimum

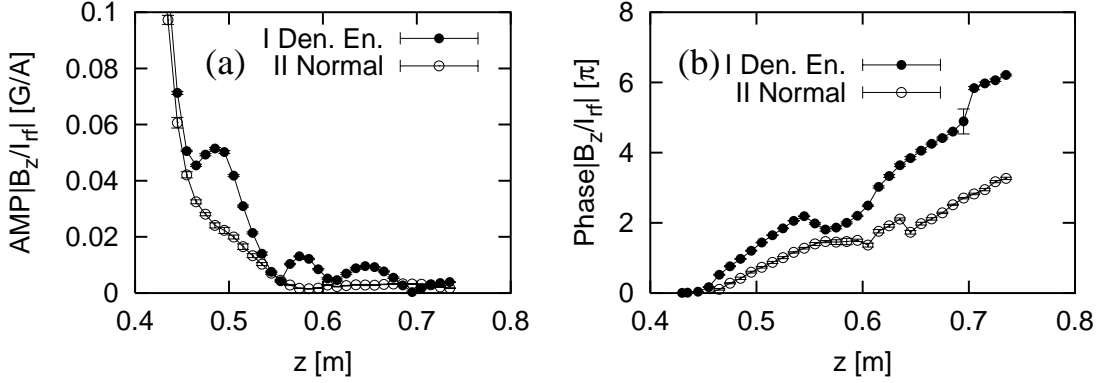


Figure 6.5: Measurements of the relative magnitude and phase of the axial RF magnetic field performed during previous experiments [32] for both the density enhancement (open circles) and normal (closed circles) operations.

in the J_{is} versus ω_{LH-HD}/ω curve, is observed for the focus type geometry with M. R. ≥ 5.0 , but not for cases in which $|B|$ does not monotonically increase between the antenna and the downstream field peak. The magnitude of the ion saturation current observed for low magnetic field strengths depends very strongly on the value of M. R. in the region $\omega_{LH-HD}/\omega < 1$, but much more weakly, at least for M. R. > 1.2 , in the region $\omega_{LH-HD}/\omega < 1$. This can be explained by the fact that high M. R. has a wide range of the magnetic field strength around source region and then plasma generations would occur further downstream region where magnetic field is higher.

As shown in Figure 6.6, a significant difference is observed between hydrogen and helium for high field $\omega_{LH-HD}/\omega > 1.5$ operation. For hydrogen, a sudden drop in J_{is} is observed as $|B|$ is increased, while for helium, J_{is} decreases much more gradually with increasing $|B|$. A possible explanation is the dependence of the power threshold to achieve helicon mode operation on the magnetic field strength. Figure 6.7 is a graph of this dependence for both hydrogen and helium. The flux tube mapping and fill pressure were fixed at M. R. = 5.0 and 6 mTorr, respectively. It can clearly be seen that for $\omega_{LH-HD}/\omega > 1$, the power threshold begins to increase rapidly for hydrogen, while it decreases slowly for helium. Thus, in the case of hydrogen, above $\omega_{LH-HD}/\omega = 1.5$, the power is insufficient to sustain a helicon mode in the plasma. For helium, a possible explanation for the gradual decrease of ion saturation current

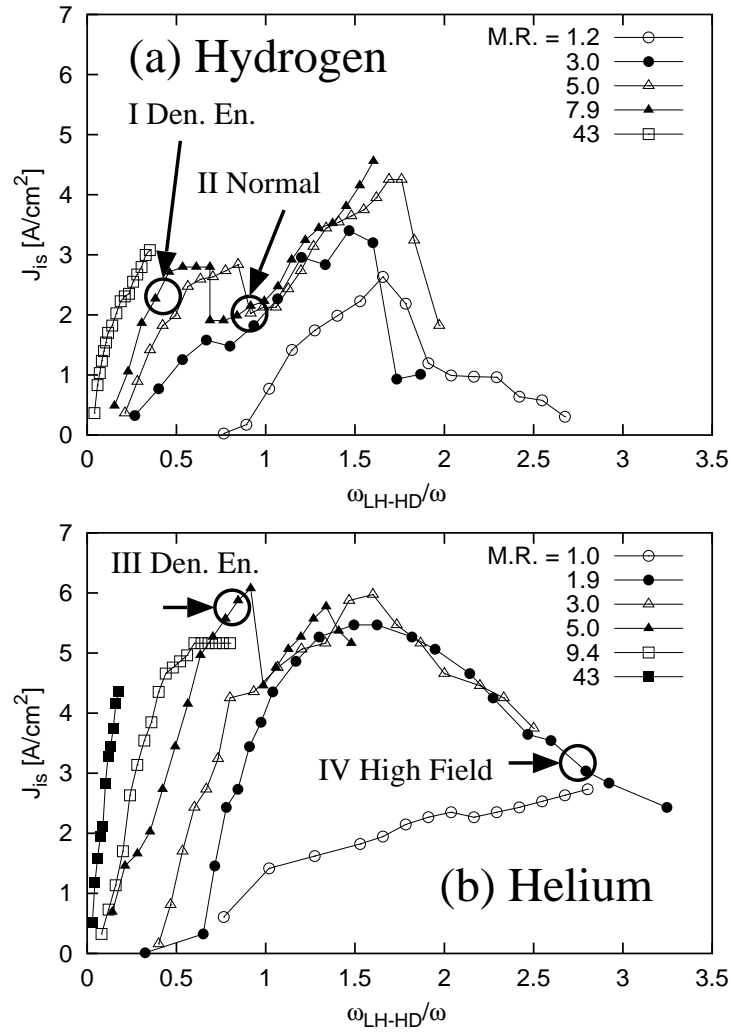


Figure 6.6: Ion saturation currents at upstream probe versus ω_{LH-HD}/ω for values of M. R. between 1 and 43 at both hydrogen (a) and helium (b).

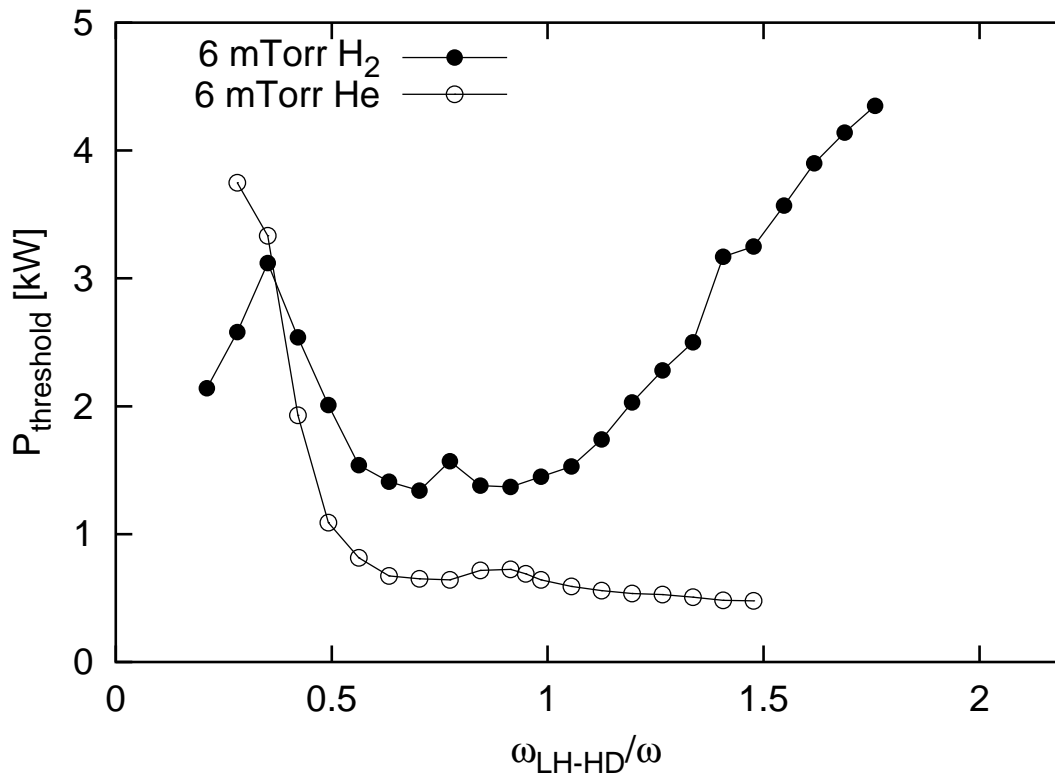


Figure 6.7: Power threshold for density jump versus ω_{LH-HD}/ω both 6 mTorr hydrogen (closed circles) and 6 mTorr helium (open circles).

with increasing $|B|$ is simply that the helicon mode wavelength continues to increase, reducing upstream power absorption.

In support of this possibility, Figure 6.8 shows the radial profile of ion saturation current measured (a) upstream and (b) downstream for two cases, denoted as III: Density Enhancement and IV: High Field. This data was obtained with helium at 4.5 kW net power and 10 mTorr fill pressure. The upstream probe shows higher values of J_{is} near the axis for the density enhanced case (Figure 6.8 a), while the downstream probe shows higher values at all radii for the high field case (Figure 6.8 b). In addition, the plasma was observed visually to be brighter in the downstream viewing region for the high field case.

Figure 6.9 shows graphs of plasma line density measured with a microwave interferometer and J_{is} as a function of M. R. for which the value of ω_{LH-HD}/ω is optimized to give the maximum J_{is} value at every data point. As a result some of

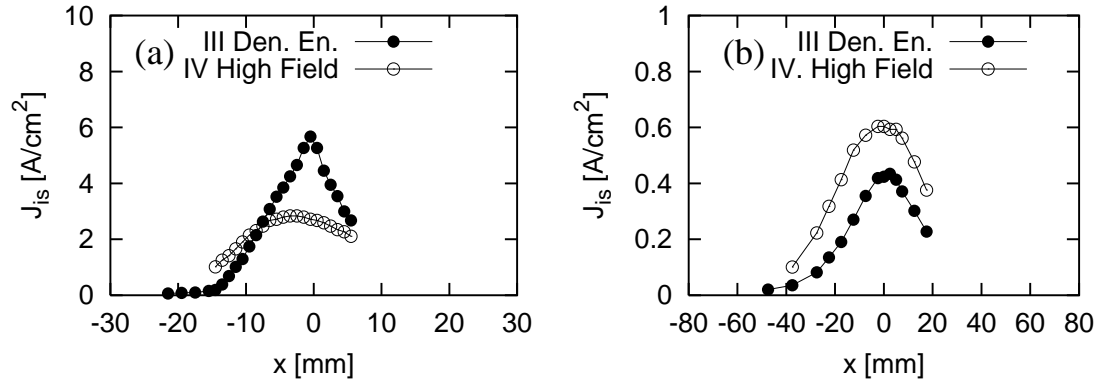


Figure 6.8: Radial profile of ion saturation current for helium measured (a) upstream and (b) downstream for III: Density Enhancement and IV: High Field labeled in Figure 6.6. Net power and fill pressure was 4.5 kW, and 10 mTorr, respectively.

the data was obtained in the density enhance mode and some was obtained in the normal mode. The other parameters chosen were fill pressure = 11 mTorr and $P = 5$ kW in hydrogen (Figure 6.9 a), and fill pressure = 6 mTorr and $P = 4.5$ kW in helium (Figure 6.9 b). The arrows denote the fact that operation at higher M. R. was possible for both gases, but not without either reducing the current in the SOL coil below the optimum value, or increasing the current in the MR1 coil beyond the capability of its power supply. Thus, higher plasma density is likely achievable with increased M. R. and solenoid magnetic field. The data also highlights the positive effect of the M. R. on the plasma density in the source region.

6.5 Discussion

In Section 6.3, it was found that enhancement of the plasma density in the $\omega_{LH-HD}/\omega < 1$ region for non-uniform magnetic field configurations was sensitive to the field strength. A local minimum in the graph of plasma density versus ω_{LH-HD}/ω was found for a specific value of $\omega_{LH-HD}/\omega < 1$, which was not sensitive to the power level or the ion species (at least for the cases of H and He). Higher fill pressure caused the location of the minimum to move to a higher value of ω_{LH-HD}/ω . In Section 6.4, it was also seen that the flux tube geometry (specifically the ratio of the peak magnetic field strength to that in the solenoid) was also important in achieving the maximum possible density in the “density enhanced” regime for which

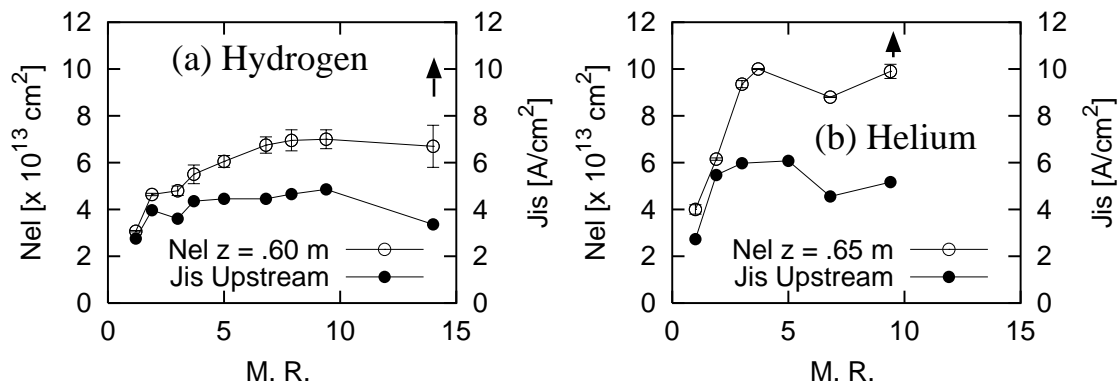


Figure 6.9: Measurements of plasma line density with a microwave interferometer and J_{is} for which the value of ω_{LH-HD}/ω is optimized to give the maximum J_{is} as a function of M. R. both (a) hydrogen and (b) helium.

ω_{LH-HD}/ω was somewhat below 1.

For the case of this regime, a strong beating wave field pattern was detected in the previous experiments that were attributed to the excitation of at least two waves with different axial and radial wavelengths. Chen previously observed beating patterns that were explained as wave reflection from a backplate [70]. However, in the case of the patterns shown here in Figure 6.5, reflection of waves from the front end would be necessary, but because of the large axial attenuation in the device it is unlikely that the beating pattern could be explained by wave reflection. The relative upstream and downstream radial density profiles seen in our experiments (Figures 6.4 and 6.8) suggest that at least in this case the enhanced source density is due not to reflections but to excitation of the higher radial mode as well as incremental damping. For the “normal” operating mode, only long wavelength modes are present, evidence of strong wave beating is not observed, and power propagates and produces plasma further downstream.

From the results described in Section 6.4, it appears that the existence of a “focusing” geometry, in which the field lines intersect the quartz tube only upstream of the antenna is necessary to achieve the low field, density enhanced regime, for which $\omega_{LH-HD}/\omega < 1$.

For operation with M. R. < 5.0 , in which case field lines intersect the quartz tube downstream of the antenna in addition to upstream, density in the source region

was reduced by a factor of 2 or more. Since power is lost in regions where the field lines intersect the inner wall of the tube, eliminating the downstream intersection results in power being lost this way in the backward direction only. The effect of collisional mirror confinement [68, 98] which tends to increase the upstream density while decreasing the downstream flow seems to explain upstream and downstream density profile differences observed on helium operations shown in Figure 6.8.

An incremental of the fill pressure was found contributing to increase the value of $|B|$ for which the density enhanced regime could be achieved for either hydrogen or helium. Collisional damping effects upstream of the antenna region for non-uniform fields, as suggested by Gilland et al. [96], may be partly responsible for such density enhancements. By using a focusing geometry, and increasing the pressure upstream of the antenna so that the intersection of the field lines with the quartz tube on downstream is reduced and collisional confinement of upstream is achieved, further improvements in the density enhanced mode may be achieved. This approach is illustrated in Figure 6.10. The true explanation requires exact modeling of axial non-uniform magnetic field geometry such as using RF simulation code with transport model, however experiments addressed above have revealed that a field geometry had an important role in the density optimization. The increased plasma density produced in the density enhanced mode is especially important for fusion and space propulsion applications where a low neutral density is required in the downstream region.

In Section 6.4, it was observed that the helicon source performance differed for hydrogen and helium at higher magnetic field strengths ($\omega_{LH-HD}/\omega > 1$). This can be explained by the dependence of the power threshold for achieving the jump from inductive to helicon operating mode on magnetic field strength. It indicates that the source species that will be used is an important consideration in the optimization of such sources.

6.6 Conclusions

Operation at plasma densities considerably higher than 10^{19} m^{-3} has been achieved for a light ion helicon source operating with an axially non-uniform magnetic field. Performance of the source has found to depend strongly on the field geometry and

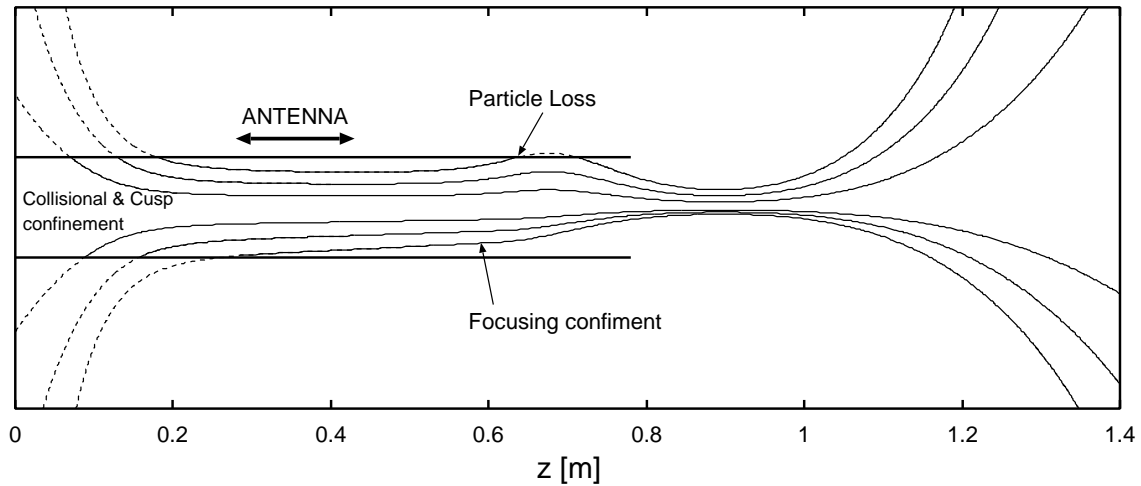


Figure 6.10: Flux tube mapping for (a) flare: no density enhancement configuration and (b) focus: density enhancement configuration.

magnetic field strength normalized to the magnetic field for which $\omega = \omega_{LH-HD}$ in the bulk plasma. Improved performance for low values of ω_{LH-HD}/ω has been observed which is possibly explained by increased power deposition in the source region caused by the presence of higher radial mode at the low values of $|B|$ existing in this case. A focusing magnetic field geometry is required, which may be due to the fact that it reduces power and particles lost to the quartz tube downstream from the antenna. The difference in behavior between hydrogen and helium at high values of $|B|$ can be explained by differences in the dependence of the density jump power threshold on the magnetic field strength.

Chapter 7

Focusing magnetic field contribution for helicon plasma

7.1 Introduction

In terms of high density plasma production, helicon plasma sources have attracted great interests for high ionization efficiency. Though researches have been conducted for many years [22, 23], their interests have been focused on heavy ions such as Ar and relatively uniform magnetic field geometries. For light ion helicon plasmas, it has been reported that magnetic field strength and geometry are key issues for their operation optimizations [68]. A control of plasma flow and sustainment is also important for applications requiring high density and high magnetic field strength for downstream represented as VASIMR project [12]. These understandings are also useful for further developments of plasma source required for plasma propulsion and fusion intended researches such as plasma-materials interaction.

This chapter reveals external magnetic field geometry effects on plasma sustainment in light ion (hydrogen and helium) sources. RF power dependences of plasma sustainment are investigated from the measurements of both axial and radial plasma profiles. Following this section, external magnetic field configurations are introduced in Section 7.2. Experimental results and discussions are presented in Section 7.3. Summary and conclusion are given in Section 7.4

7.2 Experimental Setup

Experimental apparatus for non-uniform magnetic field experiments is shown in Figure 3.1, Chapter 3. Both hydrogen and helium gases are used at around 10 mTorr. Setup of diagnostics includes the 70-GHz interferometer, RF compensated Langmuir probes (both upstream and downstream) and the I-V sensor. Plasma was sustained 40 msec with duty rate 2 %. The matching was tuned to keep the reflected power less than 5 % of the forward power.

Figure 7.1 shows varieties of magnetic field geometry on Mini-RFTF for (a) external axial magnetic field profiles and (b) flux tube mappings. Locations of the helical antenna and coils as well as probes are also shown in Figure 7.1. In Figure 7.1, field strength (a) and flux tube mappings (b) are plotted for three geometries represented as "focus", "flat" and "flare". Here, focus case has focusing field geometry toward downstream and the field line has an intersection with the quartz tube wall. For flare, the flux tube is pinched as shown in Figure 7.1 (b) and two intersections are occurred between the quartz tube and the field line. Flat case keeps uniformity from the antenna installation position to the edge of SOL coil. Field geometries shown in the figure were applied to the experiments described here for both hydrogen and helium. The amplitude of magnetic field strength at MR1 coil location ($z = 0.9$ m) was 0.32 T for helium as shown in Figure 7.1, and 0.25 T for hydrogen operation.

7.3 Experimental Results and Discussion

Figure 7.2 shows a net power dependence of ion saturation currents measured by the upstream probe and loading resistance for focus and flat magnetic field configurations in both hydrogen and helium discharges. Fill pressure was 11 mTorr for hydrogen and 10 mTorr for helium.

For the hydrogen discharge, as shown in Figure 7.2 (a), flat magnetic field configuration on source region requires a density jump to sustain high density plasma. The loading also represents this jump as shown in Figure 7.2 (b). On the other hand, for focus field also shown in Figures 7.2 (a) and (b), behavior is transferred to high density mode without sudden jump of plasma density or loading. Similar results are shown for helium discharges in Figures 7.2 (c) and (d). From the view point of experimental technique, matching for focusing field was smooth and values

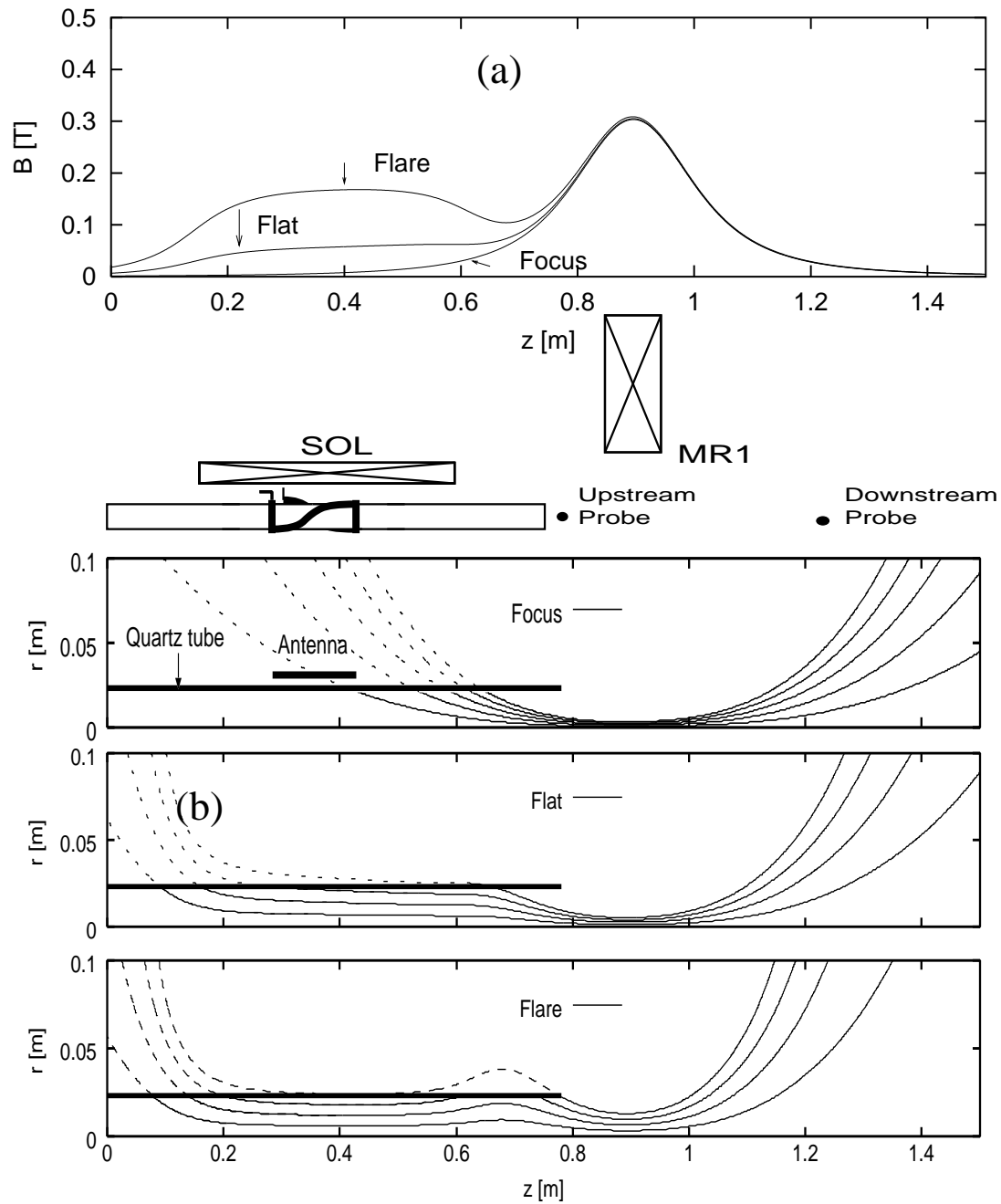


Figure 7.1: Variety of magnetic field geometry on Mini-RFTF (a) external axial magnetic field strength profile and (b) flux tube mapping.

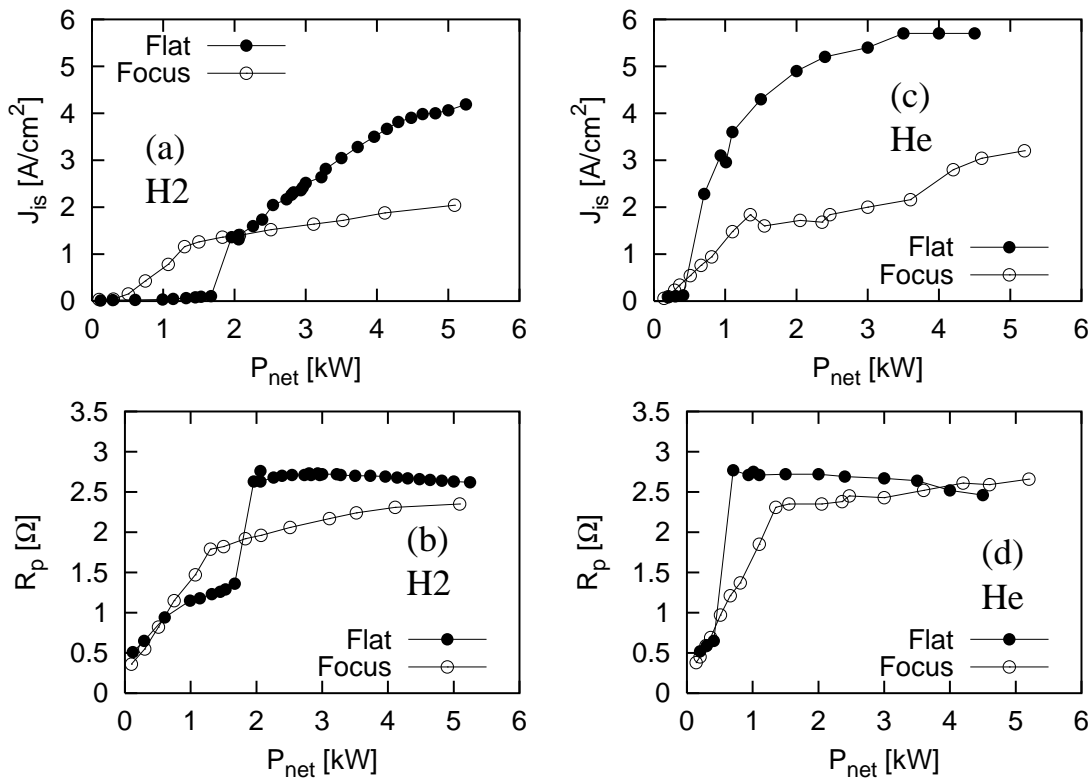


Figure 7.2: Net power dependence of ion saturation currents (a) hydrogen and (b) helium and plasma loading resistance (c) hydrogen and (d) helium for focus and flat field geometries.

of capacitance were continuous for whole range of operation. For the focusing magnetic field, the plasma sustainment with lower power was also available than flat case for both hydrogen and helium.

Compared with flat magnetic field configuration, focusing field has a field lines which more directed to the on-axis and then magnetized electrons move along the lines toward the center. According to the helicon plasma dispersion relation, axial wavenumber k is proportional to n_e/B_0 , where n_e is the electron density and B_0 is the external magnetic field strength. Since focusing field has a broader-scale of external magnetic field strength on source region compared with flat configuration, there is a flexibility to satisfy the dispersion relation which resulted in plasma sustainment.

To understand the effect of field configuration on plasma sustainment, measurements of axial and radial density profiles for three magnetic field as shown in

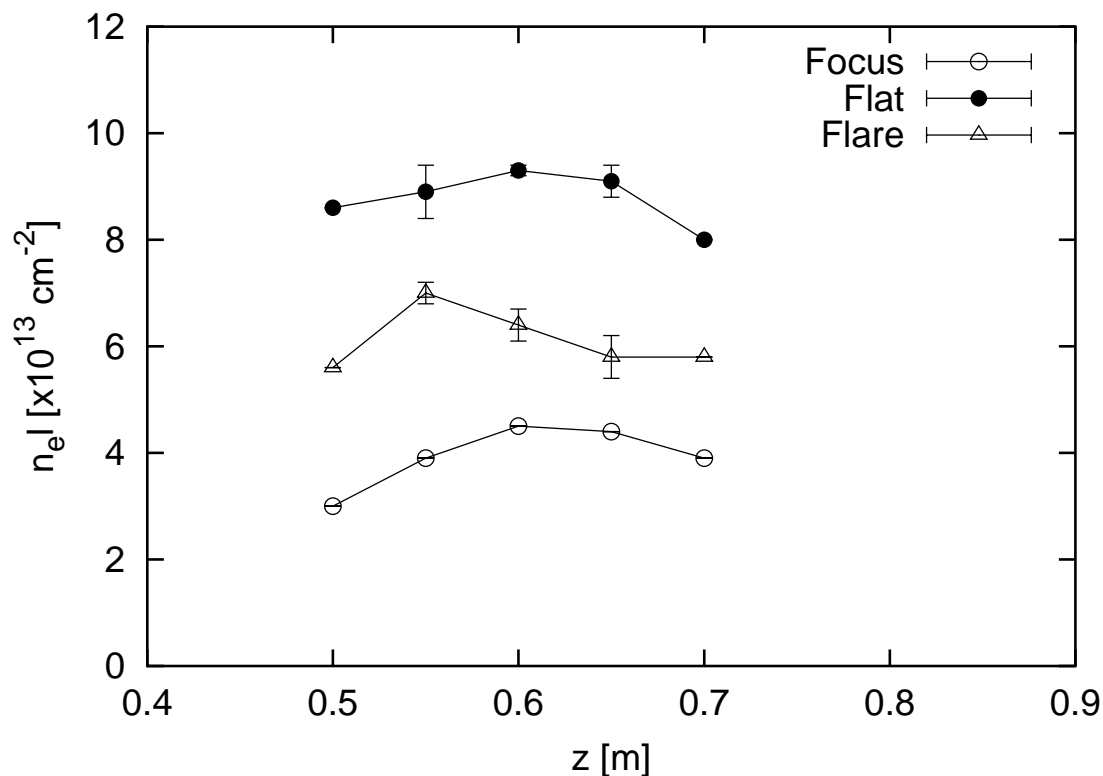


Figure 7.3: Axial profile of line density measurements for focus (open circles), flat (closed circles) and flare (open triangles) field geometries in helium.

Figure 7.1 were conducted for helium. For this operation, fill pressure was 10 mTorr and net power was 4.5 kW.

Axial line-averaged electron density profiles on source region measured by the interferometer are shown in Figure 7.3 for focus (open circles), flat (closed circles) and flare (closed triangles) field configurations. Figure 7.4 represents radial profiles of ion saturation currents measured by (a) upstream and (b) downstream probes for the three field geometries in helium.

For upstream region, as shown in Figures 7.3 and 7.4 (a), flat configuration sustains higher density than those of other cases. On the other hand, for downstream as shown in Figure 7.4 (b), flare geometry has higher density and wider plasma profile than those of other cases. It indicates that plasma production region is shifted toward downstream for flare configuration.

Figure 7.5 shows viewings from the viewing port on downstream ($z = 1.22$ m) for

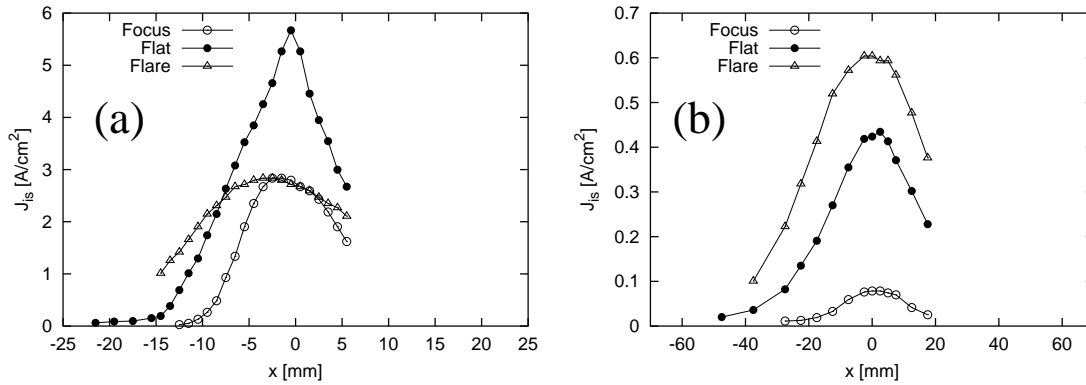


Figure 7.4: Radial ion saturation currents profile of (a) upstream ($z = 0.78$ m) and (b) downstream ($z = 1.22$ m) for focus, flat and flare geometries.

(a) focus and (b) flare configurations. Case (a) represents a narrow stream flow and case (b) shows a bright wide plasma plume flow. It indicates that plasma generation is occurring on downstream for flare configuration. The control of plasma radius on downstream is strongly related with upstream field configurations.

7.4 Summaries and Conclusions

Field geometry dependence in source region has been conducted for Mini-RFTF device. The net power dependence for strong focusing fields had gradual density transition compared with flat field configuration in which clear density transition for helicon mode was observed. Strong focusing field geometry contributes to sustain high density helicon plasma without dedicated matching control. For three field geometries, density profile measurements were also conducted and found that flare geometry contributed to shift the plasma generation region to downstream. For an application toward high density plasma source, magnetic field configuration in source region was strongly related to the downstream plasma sustainment and appropriate methods for further optimization. Such method is useful for plasma propulsion where plasma radius controlling is a key issues related with ion heating and acceleration.

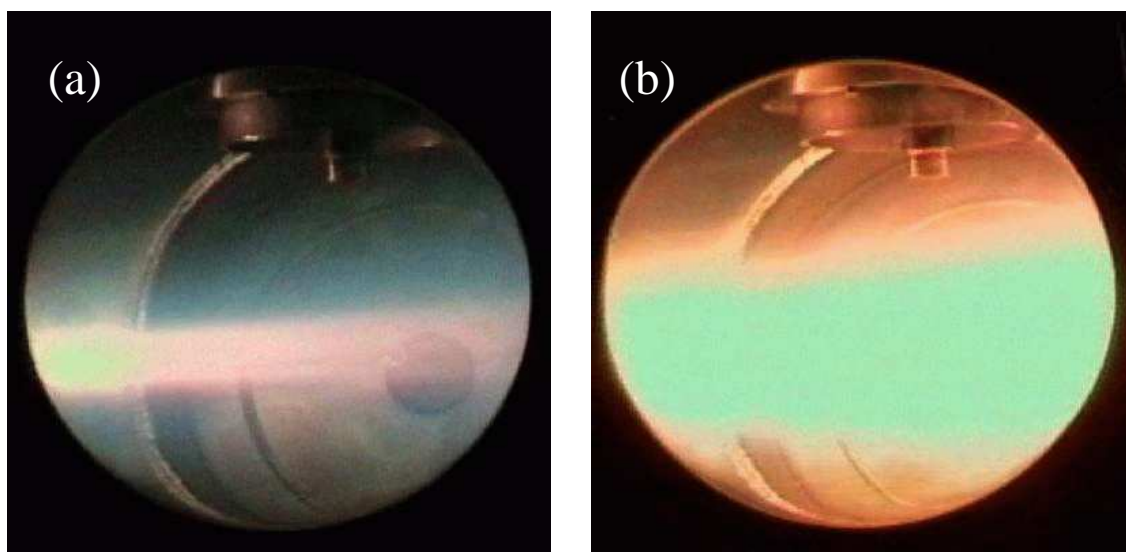


Figure 7.5: Plasma view from the viewing port ($z = 1.22$ m) for (a) focus and (b) flare geometries.

Chapter 8

CONCLUSIONS

This thesis has examined the non-uniformity magnetic field contributions for high-density hydrogen and helium helicon plasma sustainment. High density ($> 10^{19} \text{ m}^{-3}$) hydrogen helicon plasma was successfully sustained, which had been considered difficult until recent. Experimental investigations of non-uniformity magnetic field contributions have been conducted and comparison between computational model including transport model were also examined. Conclusions described in this thesis are as follows:

Comparison of high-density hydrogen helicon plasma between experiments and computations using the RF-modeling numerical code including transport model were described in Chapter 4. As the results, qualitative agreement between the flux-tube-averaged transport model and experiments were obtained as far as plasma generation and power balance are concerned. The electromagnetic wave propagations could be simulated qualitatively by the RF-modeling based on the measured plasma density profile. It was also found that collisional damping of helicon wave was mainly contributing to high-density hydrogen helicon plasma sustainment.

Chapter 5 described high density hydrogen helicon plasmas in a nonuniform magnetic field. Here, high-density ($\sim 10^{19} \text{ m}^{-3}$) hydrogen plasma has been successfully sustained in axially nonuniform static magnetic field configurations for frequencies both above and below the high-density limit of the lower hybrid resonance frequency (LH-HD). Wave field measurements suggested that several modes were coupling to generate these helicon plasmas. The dependence of the plasma density on the static magnetic field strength for fixed geometry could be explained by wavelength that was close to the antenna length and that couple to the axial wavelength of the fun-

damental radial mode for frequencies below the LH-HD frequency and to the axial wavelength of the second radial mode for frequencies above the LH-HD frequency.

Chapter 6 gave a discussion on the density enhancement due to the non-uniform magnetic fields for hydrogen and helium discharges. The ultimate achievable density, well above 10^{19} m^{-3} both hydrogen and helium, has been found to depend strongly on both shape and strength of the axial magnetic field profile. As the magnetic field strength was swept from low to high values, two local maxima in plasma density were observed for cases in which the field strength increased monotonically in the downstream direction away from the helicon antenna. A comparison of the plasma density close to the antenna and further downstream suggested that the first maximum occurred at low field corresponds to efficient power absorption on source region. For the second maximum at high field, the plasma density dropped sharply in the case of hydrogen, but only slowly in the case of helium. The data suggested that this was due to a strong rise in the threshold power required to reach the high-density mode in hydrogen, which was not seen for helium operation.

Chapter 7 described a contribution of source magnetic field configurations for hydrogen and helium helicon plasma. Here, field geometry dependence in source regions was conducted. As the results, the net power dependence for strong focus field had gradual high-density transition compared with flat field configuration in which clear helicon mode transitions were observed. Strong focusing field geometry resulted in sustainment of high-density helicon plasma without dedicated matching control. For three geometries, both axial and radial density profiles were measured and found that flare geometry made plasma generation region further downstream. For applications such as high-density plasma sources, configuration of magnetic field in source region was strongly related to the downstream plasma sustainment.

As described above, high-density ($\sim 10^{19} \text{ m}^{-3}$) hydrogen helicon plasma has been successfully sustained with non-uniform magnetic field geometries. This had been considered difficult because of RF power limitation and low particle confinement times. As the results of light-ion helicon plasma experiments such as hydrogen and helium, magnetic field geometries have a strong influence on source optimizations. Plasma plume controls are possible with field geometry optimizations. For the application to fusion test components and plasma propulsions with ICR heating, control of neutral gas pressure is required as a future work.

References

- [1] Y. Mori, Y. Takao, and H. Nakashima, in *Proceedings of the 26th International Electric Propulsion Conference*, Kitakyushu, 1999, Vol. 2, p. 1329.
- [2] Y. Mori, T. Noutsuka, Y. Takao, and H. Nakashima, in *Proceedings of the 1st Cross Strait Symposium on Materials, Energy and Environmental Sciences*, Fukuoka, 1999, Vol. 1, p. 50.
- [3] H. Sou, Y. Takao, T. Noutsuka, Y. Mori, K. Uemura, and H. Nakashima, *Vacuum* **59**, 73 (2000).
- [4] Y. T. T. Noutsuka, Y. Mori, K. Uemura, H. Sou, and H. Nakashima, in *Proceedings of the 22nd International Symposium Space Technology and Science*, Morioka, 2000, Vol. 1, p. 403.
- [5] Y. Mori, T. Noutsuka, Y. Takao, and H. Nakashima, *Trans. Fusion Technol.* **39**, 195 (2001).
- [6] T. Gouda, Y. Mori, Y. Takao, T. Esaki, S. Iwata, and H. Nakashima, in *Proceedings of the 2nd Cross Strait Symposium on Materials, Energy and Environmental Sciences*, Pusan, 2000, Vol. 1, p. 223.
- [7] Y. Mori, Y. Takao, K. Uemura, T. Gouda, T. Miyamoto, T. Esaki, T. Maeyama, T. Muranaka, and H. Nakashima, in *Proceedings of the International Conference on Plasma Physics 2000*, Québec, 2000, Vol. 3, p. 920.
- [8] T. Gouda, Y. Mori, Y. Takao, S. Iwata, and H. Nakashima, in *Proceedings of the 25th International Conference on Phenomena in Ionized Gases*, Nagoya, 2001, Vol. 1, p. 307.

- [9] A. Ando, R. Kumagai, S. Fujimura, T. Yagi, K. Hattori, and M. Inutake, in *Proceedings of the International Conference on Plasma Physics 2002*, Sydney, 2002, Vol. 4, p. 131.
- [10] A. Ando, S. Fujimura, T. Yagi, Y. Hosokawa, K. Hattori, and M. Inutake, in *Proceedings of the 26th International Conference on Phenomena in Ionized Gases*, Greifswald, 2003, Vol. 699, p. 497.
- [11] M. Inutake, R. Kumagai, S. Fujimura, T. Yagi, and K. Hattori, *Trans. Fusion Sci. Technol.* **43**, 118 (2003).
- [12] F. R. Chang-Díaz, *Sci. Am.* **283**, 72 (2000).
- [13] F. R. Chang-Díaz, *Trans. Fusion Technol.* **35**, 87 (1999).
- [14] F. R. Chang-Díaz, *Trans. Fusion Sci. Technol.* **43**, 3 (2003).
- [15] J. P. Squire, F. R. Chang-Díaz, T. W. Glover, V. T. Jacobson, D. G. Chavers, R. D. Bengtson, E. A. Bering, R. W. Bosell, R. H. Goulding, and M. Light, *Trans. Fusion Sci. Technol.* **43**, 111 (2003).
- [16] A. V. Arefiev and B. N. Breizman, *Phys. Plasmas* **11**, 2942 (2004).
- [17] T. H. Stix and R. W. Palladino, *Phys. Fluids* **1**, 446 (1958).
- [18] Y. Shimomura, R. Ayamar, V. Chuyanov, M. Huguet, and R. Parker, *Nucl. Fusion* **39**, 1295 (1999).
- [19] R. M. Gallet, J. M. Richardson, B. Wieder, and G. D. Ward, *Phys. Rev. Lett.* **4**, 347 (1960).
- [20] J. A. Lehane and P. C. Thonemann, *Proc. Phys. Soc.* **85**, 301 (1965).
- [21] R. W. Boswell, *Plasma Phys. Control. Fusion* **26**, 1147 (1984).
- [22] R. W. Boswell and F. F. Chen, *IEEE Trans. Plasma Sci.* **25**, 1229 (1997).
- [23] F. F. Chen and R. W. Boswell, *IEEE Trans. Plasma Sci.* **25**, 1245 (1997).
- [24] R. W. Boswell and D. Henry, *Appl. Phys. Lett.* **47**, 1095 (1985).

- [25] G. R. Tynan et al., *J. Vac. Sci. Technol. A* **15**, 2885 (1997).
- [26] P. K. Loewenhardt, B. D. Blackwell, R. W. Boswell, G. D. Conway, and S. M. Hamberger, *Phys. Rev. Lett.* **67**, 2792 (1991).
- [27] H. Takeno, Y. Yasaka, O. Sakai, and R. Itatani, *Nucler Fusion* **35**, 75 (1995).
- [28] Y. Sakawa, M. Ohshima, Y. Ohta, and T. Shoji, *Phys. Plasmas* **10**, 3447 (2003).
- [29] J. L. Kline, E. E. Scime, P. A. Keiter, M. M. Balkey, and R. F. Boivin, *Phys. Plasmas* **6**, 4767 (1999).
- [30] X. Sun, C. Biloiu, R. Harding, and E. E. Scime, *Plasma Sources Sci. Technol.* **13**, 359 (2004).
- [31] M. Aramaki, K. Kato, M. Goto, S. Muto, S. Morita, and K. Sasaki, *Jpn. J. Appl. Phys.* **43**, 1164 (2004).
- [32] Y. Mori, H. Nakashima, F. W. Baity, R. H. Goulding, M. D. Carter, and D. O. Sparks, *Plasma Sources Sci. Technol.* **13**, 424 (2004).
- [33] R. H. Goulding, D. Pavarin, F. Angrilli, G. C. Barber, M. D. Carter, R. Maggiora, and D. O. Sparks, in *Proceedings of the International Conference on Electromagnetics in Advanced Applications*, Torino, 1999, p. 107.
- [34] F. W. Baity, private communication.
- [35] P. Aigrain, in *Proceedings of the International Conference on Semiconductor Physics*, Prague, 1960, p. 224.
- [36] C. R. Legéndy, *Physical Review* **135**, A1713 (1964).
- [37] J. P. Klosenberg, B. McNamara, and P. C. Thonemann, *J. Fluid Mech.* **21**, 545 (1965).
- [38] H. A. Blevin, P. J. Christiansen, and B. Davies, *Phys. Lett.* **28 A**, 230 (1968).
- [39] B. Davies, *J. Plasma Phys.* **4**, 43 (1970).
- [40] R. W. Boswell, *J. Plasma Phys.* **31**, 197 (1984).

- [41] R. L. Ferrari and J. P. Klozenberg, *J. Plasma Phys.* **2**, 283 (1968).
- [42] B. Davies and P. J. Christiansen, *Plasma Phys.* **11**, 987 (1969).
- [43] K. P. Shamrai and V. B. Taranov, *Phys. Lett.* **204A**, 139 (1995).
- [44] K. P. Shamrai and V. B. Taranov, *Plasma Sources Sci. Technol.* **5**, 474 (1996).
- [45] T. H. Stix, *Waves in Plasmas*, American Institute of Physics, New York, 1992.
- [46] F. F. Chen, *Plasma Phys. Control. Fusion* **33**, 339 (1991).
- [47] F. F. Chen, M. J. Hsieh, and M. Light, *Plasma Sources Sci. Technol.* **3**, 49 (1994).
- [48] I. D. Sudit and F. F. Chen, *Plasma Sources Sci. Technol.* **3**, 602 (1994).
- [49] Y. Sakawa, N. Koshikawa, and T. Shoji, *Plasma Sources Sci. Technol.* **6**, 96 (1997).
- [50] R. T. S. Chen, R. A. Breun, S. Gross, N. Hershkowitz, M.-K. J. Hsieh, and J. Jacobs, *Plasma Sources Sci. Technol.* **4**, 337 (1995).
- [51] M. Krämer, *Plasma Sources Sci. Technol.* **6**, 1052 (1999).
- [52] W. L. Gardner, D. J. Hoffman, H. C. McCurdy, T. J. McManamy, J. A. Moeller, and P. M. Ryan, in *Proceedings of the 11th Symposium on Fusion Engineering*, Austin Texas, 1985, p. 1328.
- [53] J. B. O. Caughman, II, D. N. Ruzic, D. J. Hoffman, R. A. Langley, M. B. Lewis, and P. M. Ryan, in *Proceedings of the IEEE 13th Symposium on Fusion Engineering*, Knoxville, 1989, Vol. 2, p. 921.
- [54] D. W. Swain, R. H. Goulding, and P. M. Ryan, *Fusion Sci. Technol.* **41**, 69 (2002).
- [55] M. A. Lieberman and A. J. Lichtenberg, *Principles of Plasma Discharges and Materials Processing*, John Wiley & Sons, Inc., New York, 1994.

- [56] I. H. Hutchinson, *Principles of Plasma Diagnostics*, Cambridge, New York, first edition, 1987.
- [57] N. Benjamin, *Rev. Sci. Instrum.* **53**, 1541 (1982).
- [58] P. A. Chatterton, J. A. Rees, W. L. Wu, and K. Al-Assidi, *Vacuum* **42**, 489 (1991).
- [59] T. P. Schneider, W. W. Dostalík, A. D. Springfield, and R. Kraft, *Plasma Sources Sci. Technol.* **8**, 397 (1999).
- [60] I. D. Suid and F. F. Chen, *Plasma Sources Sci. Technol.* **3**, 162 (1994).
- [61] P. Beiersdorfer and E. J. Clothiaux, *Am. J. Phys.* **51**, 1031 (1983).
- [62] J. G. Yang, J. H. Choi, B. C. Kim, N. S. Yoon, and S. M. Hwang, *Rev. Sci. Instrum.* **70**, 3774 (1999).
- [63] M. Light, I. D. Suid, F. F. Chen, and D. Armush, *Phys. Plasmas* **2**, 4094 (1995).
- [64] H. Nogami, Y. Ogahara, K. Mashimo, Y. Nakagawa, and T. Tsukada, *Plasma Sources Sci. Technol.* **5**, 181 (1996).
- [65] A. Fukuyama and Y. Ichida, in *Proceedings of the 1996 International Conference on Plasma Physics*, Nagoya, 1996, Vol. 2, p. 1342.
- [66] Y. Mouzouris and E. Scharer, *Phys. Plasmas* **5**, 4253 (1998).
- [67] D. Arnush, *Phys. Plasmas* **7**, 3042 (2000).
- [68] M. D. Carter, F. W. Baity Jr., G. C. Barber, R. H. Couling, Y. Mori, D. O. Sparks, K. F. White, E. F. Jaeger, F. R. Chang-Díaz, and J. P. Squire, *Phys. Plasmas* **9**, 5097 (2002).
- [69] F. F. Chen, *J. Vac. Sci. Technol. A* **10**, 1389 (1992).
- [70] F. F. Chen, *Phys. Plasmas* **10**, 2586 (2003).
- [71] Y. Yasaka and Y. Hara, *Jpn. J. Appl. Phys.* **33**, 5950 (1994).

- [72] J. D. Huba, *NRL Plasma Formulary*, Beam Physics Branch and Plasma Physics Division Naval Research Laboratory, Washington, DC, 2002 revised.
- [73] M. D. Carter, F. W. Baity Jr., G. C. Barber, R. H. Couding, Y. Mori, D. O. Sparks, K. F. White, E. F. Jaeger, F. R. Chang-Díaz, and J. P. Squire, *Trans. Fusion Sci. Technol.* **43**, 125 (2003).
- [74] Y. Setsuhara, Y. Sakawa, T. Shoji, M. Kumagai, and S. Miyake, *Surf. Coat. Technol.* **142-144**, 874 (2001).
- [75] X. M. Guo, J. Scharer, Y. Mouzouris, and L. Louis, *Phys. Plasmas* **6**, 3400 (1999).
- [76] S. Rosenberg and W. Gekelman, *Geophys. Res. Letters* **25**, 865 (1998).
- [77] J. L. Pinçon, P. M. Kintner, P. W. Schuck, and C. E. Seyler, *J. Geophys. Res.* **102**, 17283 (1997).
- [78] C. Gormezano, *Plasma Phys. Control. Fusion* **28**, 1365 (1986).
- [79] P. Zhu and R. W. Boswell, *Phys. Rev. Lett.* **63**, 2805 (1989).
- [80] S. Yun, S. Cho, G. Tynan, and H. Chang, *Phys. Plasmas* **8**, 358 (2001).
- [81] S. Cho, *Phys. Plasmas* **7**, 417 (2000).
- [82] M. M. Balkey, R. Boivin, J. L. Kline, and E. E. Scime, *Plasma Sources Sci. Technol.* **10**, 284 (2001).
- [83] J. L. Kline, E. E. Scime, R. F. Boivin, A. M. Keesee, and X. Sun, *Phys. Rev. Lett.* **88**, 195002 (2002).
- [84] Y. Sakawa, T. Shoji, T. Takino, Y. Kuroki, and K. Shimura, in *Proceedings of the 1996 International Conference on Plasma Physics*, Nagoya, 1996, Vol. 2, p. 1334.
- [85] Y. Sakawa, T. Takino, and T. Shoji, *Phys. Plasmas* **6**, 4759 (1999).
- [86] M. Light, F. F. Chen, and P. L. Colestock, *Phys. Plasmas* **8**, 4675 (2001).

- [87] A. Bouchoule and P. Rierson, *J. Vac. Sci. Technol. A* **9**, 317 (1991).
- [88] Y. Sakawa, M. Ohshima, Y. Ohta, and T. Shoji, *Phys. Plasmas* **11**, 311 (2004).
- [89] A. W. Degeling, T. E. Sheridan, and R. W. Boswell, *Phys. Plasmas* **6**, 3664 (1999).
- [90] I. D. Sudit and F. F. Chen, *Plasma Sources Sci. Technol.* **5**, 43 (1996).
- [91] K.-K. Chi, T. E. Sheridan, and R. W. Boswell, *Plasma Sources Sci. Technol.* **8**, 421 (1999).
- [92] M. Krämer, B. Lorenz, and B. Clarenbach, *Plasma Sources Sci. Technol.* **11**, A120 (2002).
- [93] K. Suzuki, K. Nakamura, and H. Sugai, *Jpn. J. Appl. Phys.* **35**, 4044 (1996).
- [94] M. Light, F. F. Chen, and P. L. Colestock, *Plasma Sources Sci. Technol.* **11**, 273 (2002).
- [95] G. Chevalier and F. F. Chen, *J. Vac. Sci. Technol. A* **11**, 1165 (1993).
- [96] J. Gilland, R. Breun, and N. Hershkowitz, *Plasma Sources Sci. Technol.* **7**, 416 (1998).
- [97] O. V. Braginskii, N. N. Vasil'eva, and A. S. Kovalev, *Plasma Phys. Rep.* **27**, 699 (2001).
- [98] J. R. Ferron et al., *Phys. Fluids* **30**, 2855 (1987).

Acknowledgements

First, I would like to thank Professor Hideki Nakashima, Kyushu university, for his tolerant guidance and then giving me a freedom to learn at my own pace which must be an indispensable skill to become a researcher. I am deeply indebted to Professor Yoshinobu Kawai, Kyushu university, and Professor Atsushi Mase, Kyushu university for intellectual supports in preparing this thesis.

I am also grateful to associate Professor Yoshiyuki Takao, Oita national college of technology, associate Professor Yukinobu Watanabe, Kyushu university, Ijiri Hidenobu, Kyushu university and members of Nakashima laboratory.

The most work described here has been conducted at Oak Ridge National Laboratory Fusion Energy Division (FED). I would like to thank Dr. David Rasmussen, the head of the technology group in FED, for his donating support, the helicon plasma project team in FED, Dr. Wallace Baity, Dr. Richard Goulding and Dr. Mark Carter, for their instructive discussions and works including lectures not only for physics or experimental technic, but also writing and speaking skill of English.

Many people contributed to the construction and running the Mini-RFTF. I would wish to thank Andy Fadnek and his crew for their mechanical engineering work. I gratefully thanks to Dennis Sparks for his machine operation and continuation of electrical engineering work. No experiment has been conducted without his help. I have learned many RF technology through the experiments from him.

My motivation for this thesis originates from Dr. Franklin Chang Díaz, astronaut in NASA and the head of the advanced space propulsion laboratory, he spared me a time during the international conference on plasma physics held in Québec 2000, this encounter paved me a way for work on VASIMR project: experiments on Mini-RFTF.

Finally, I want to thank my families in two countries, Mrs. Young and her family

for their donation of house and delicious meal during my stay in the United State,
my mother and sisters in my sweet home.